Department of Physics and Astronomy

Heidelberg University

Master thesis

in Physics

submitted by

Nadine Alice Grünwald

born in Lindenfels

2022

Studies of jets in heavy-ion collisions at ALICE with a novel mixed-event approach

This Master thesis has been carried out by Nadine Alice Grünwald

at the

Physikalisches Institut Heidelberg

under the supervision of

Prof. Dr. Johanna Stachel

Abstract:

Within heavy-ion collisions QCD matter is studied at very high temperatures and densities, where quarks and gluons are deconfined and new physics phenomena emerge. At the LHC (Large Hadron Collider) measurements of heavy-ion collisions, where the Quark-Gluon Plasma (QGP) is produced, are performed with the ALICE (A Large Ion Collider Experiment) experiment.

Unique probes of the nature of the QGP in the experiment are the measurements of jets. The energy and structure of the jets, which are high p_{T} objects, is modified due to their interaction with the QGP. A major difficulty in heavy-ion jet measurements is the huge amount of background particles which often limited the jet measurements to high p_{T}. In order to perform low p_{T} jet measurements, where the jets interact strongly with the QGP, a novel mixed-event technique is exploited.

Mixed events are used in this thesis as a new approach to describe the uncorrelated background in heavy-ion jet measurements at ALICE. The 2018 Pb+Pb data set measured at $\sqrt{s_{\mathrm{NN}}} = 5.02$ TeV with the ALICE detector at a centrality of 0-10 % is used. A charged jet reconstruction is carried out with the anti-k_{T} algorithm with jet radii between 0.2 and 0.4. The description of the uncorrelated background by mixed events enables for the first time inclusive jet measurements down to low p_{T} at such high energies. In particular no cuts on the reconstructed jet energies are necessary.

The production of the mixed events is reported in this thesis and several systematic studies, as the dependence of the mixed events on the elliptic flow, are presented. They are done in order to obtain a precise and stable description of the uncorrelated background by the mixed events. The uncorrelated background in inclusive, quasi-inclusive and h-jet distributions is described with the mixed events. For the quasi-inclusive jet distributions a cut on the leading tracks of the jets of 2-5 GeV/c is applied. A correction for background and detector effects is carried out by an unfolding procedure of the correlated quasi-inclusive jet distribution leading to a particle-level jet spectrum.

Kurzfassung:

In Schwerionenkollisionen wird die QCD-Materie bei sehr hohen Temperaturen und Dichten untersucht, bei denen Quarks und Gluonen entkoppeln und neue physikalische Phänomene auftauchen. Am LHC (Large Hadron Collider) werden Messungen von Schwerionenkollisionen, bei denen das Quark-Gluon Plasma (QGP) erzeugt wird, mit dem ALICE Experiment (A Large Ion Collider Experiment) durchgeführt.

Eine einzigartige Möglichkeit um die Eigenschaften des QGP im Experiment zu untersuchen, ist durch die Messungen von Jets gegeben. Die Energie und Struktur der Jets, bei denen es sich um Objekte mit hohem transversalen Impuls handelt, wird aufgrund ihrer Wechselwirkung mit dem QGP verändert. Eine große Schwierigkeit bei der Messung von Jets in Schwerionenkollisionen ist die große Menge an Hintergrundteilchen, welche die Jet Messungen oft auf hohe p_{T} beschränken. Um auch die Jets mit niedrigem p_{T}, deren Wechselwirkung mit dem QGP groß war, messen zu können, wird eine neuartige Mixed-Event Technik ausgenutzt.

Mixed Events werden in dieser Masterarbeit als ein neuer Ansatz genutzt, um den unkorrelierten Untergrund in Jet Messungen in Schwerionenkollisionen zu bestimmen. Der 2018 in Pb+Pb Kollisionen bei $\sqrt{s_{\mathrm{NN}}} = 5.02$ TeV und mit einer Zentralität von 0-10 % mit ALICE aufgenommene Datensatz wird analysiert. Die Rekonstruktion geladener Jets wird mit dem anti-k_{T} Algorithmus durchgeführt, wobei Jet-Radien von 0.2 bis 0.4 verwendet werden. Die Beschreibung des Untergrunds durch Mixed Events ermöglicht zum ersten Mal eine Jet Messung auch bei sehr niedrigen p_{T}. Zum ersten Mal ist es möglich, bei diesen hohen Energien, inklusive jet Messungen bis zu niedrigstem p_{T} durchzuführen, ohne ausschließlich Jets mit hohen Energien auszuwählen.

Die Produktion der Mixed Events sowie deren Eigenschaften, wie die Abhängigkeit vom elliptischen Fluss, werden systematisch untersucht, um eine optimale Beschreibung des unkorrelierten Untergrundes zu erhalten.

Der unkorrelierte Untergrund wird in inklusiven, quasi-inklusiven und Hadron-Jet Verteilungen analysiert. Für die quasi-inklusiven Jet Verteilungen wird ein Teilchen im Jet mit einem transversalen Impuls von 2-5 GeV/c vorausgesetzt. Die Korrektur von Untergrund und Detektor Effekten wird durch Unfolding für die korrelierte quasi-inklusive Jet Verteilung durchgeführt.

Contents

1. Introduction 1
1.1. QCD in the Standard Model 1
1.2. Quark-Gluon Plasma 4
1.3. Heavy-ion collisions 6
1.3.1. Flow 7
1.3.2. Kinematic variables 9

2. Jets in heavy-ion collisions 10
2.1. Jet production 10
2.1.1. Factorization 11
2.2. Jet quenching 12
2.2.1. Theoretical considerations 12
2.2.2. Experimental evidence for jet quenching 14
2.3. Experimental measurements of jets 16
2.3.1. Jet reconstruction with FastJet 16
2.3.2. Heavy-ion jet analysis 18
2.4. Overview 20

3. The ALICE Experiment at LHC 21
3.1. ALICE detector system 22
3.1.1. ITS 23
3.1.2. TPC 23
3.1.3. TRD 23
3.1.4. TOF 24
3.1.5. EMCal 24
3.1.6. V0 25
3.2. Upgrades of the ALICE detector for Run 3 26
3.3. Tracking 26

4. Data set and track selection 28
4.1. Data preparation 28
4.2. Track selection 30
4.3. Pileup rejection 35

5. Analysis strategy 39
5.1. Jet reconstruction setup 39
5.2. Event Plane reconstruction 43
5.3. Event mixing 46
5.3.1. Event categorization 48
5.3.2. Multiplicity and track distribution of the mixed events 51

5.3.3. Same and mixed event jet distribution 53

6. Systematic studies of the mixed events 55
6.1. Splitting of high momentum tracks in the mixed event 55
6.2. Normalization 59
6.3. Area and ρ distributions of same and mixed events 61
6.3.1. Variations of removed jets in the ρ calculation 64
6.4. Systematic study of different event categories 67
6.4.1. Event plane dependence of the mixed event 67
6.4.2. Multiplicity dependence 73
6.4.3. Dependence of the mixing on the z-vertex 77
6.5. Run dependent observation 79
6.6. Event-by-event p_{T} fluctuations 82

7. Raw jet distributions 88
7.1. Inclusive jets 88
7.2. Quasi-inclusive jet distribution 90
7.2.1. Variations of the jet radius 94
7.3. Hadron-jet distribution 97

8. Corrections 100
8.1. Particle-level jet generation with PYTHIA 100
8.2. Instrumental effects 102
8.3. Response matrix 104
8.4. Unfolding 108
8.5. Systematic uncertainties 113

9. Summary and Outlook 114

A. Appendix 117
A.1. Event plane 117
A.2. Mixed event studies 119
A.3. Raw jet distributions 122

Bibliography 123

1. Introduction

In the first section the Standard Model of particle physics is introduced. The focus is on Quantum Chromodynamics (QCD), the field theory of the strong force, which describes the interactions between quarks and gluons [1]. The Quark-Gluon Plasma (QGP) is introduced as a state of QCD matter, and studies of the emergent properties of this many-body system of quarks and gluons using heavy-ion collisions are discussed [2]. Section 2 discusses the concept of QCD jets and their application as a unique and inclusive probe of the behavior of the QGP.

1.1. QCD in the Standard Model

The Standard Model of particle physics describes almost all of the properties of the known fundamental particles and their interactions between them [1]. The known fundamental particles are assigned to three generations of leptons and quarks, the fermions, which form the building blocks of matter, together with the force-carrying bosons. As the last missing part of the Standard Model the Higgs boson was discovered in 2012 at the LHC [3]. The interaction between the particles and the Higgs field was predicted in 1964 as the mechanism which gives the particles their masses.

The electromagnetic force describes the interaction between particles with electric charges [1]. The interaction is exchanged by photons which are massless neutral particles. The weak force is responsible for nuclear decays, including the β-decay of a neutron into a proton via the emission of an electron and neutrino [1]. This decay is mediated by the massive charged W boson. In addition, there are neutral weak interactions mediated by the neutral Z boson.

Quantum Chromodynamics (QCD) is the field theory of the strong interaction. It describes the interaction between colored objects, the quarks and gluons [1]. The color charge is the QCD analogue of electrical charge in Quantum Electrodynamics (QED). There are three colors described as red, green and blue and the corresponding anti-colors. The gluons are the force-carrying particles of the strong interaction. In comparison to the electromagnetic force, with the neutral photon as exchanged particle, the gluons themselves carry color charge. There are six “flavors” of quarks, three up-type quarks (up, charm, top) with a charge of 2/3 and three down-type (down, strange, bottom) quarks with a charge of $-1/3$ of the electron charge.

The distinguishing characteristic of QCD is the running of the coupling constant α_s [1]. The strength of the coupling constant α_s of the strong interaction depends on the momentum transfer Q^2 of the interaction and is not constant [4]. Measurements of the coupling constant as function of momentum transfer are shown in figure 1.1. In addition the comparison to QCD calculations is shown, which are in excellent agreement with the measurements. The strength of the coupling in QCD is decreasing with increasing momentum transfer, in contrast to QED.

In the high energy range where the coupling constant is small, the interaction between quarks and gluons is weak and they can be treated as asymptotically free particles. This is the case for the initial hard scattering of quarks and gluons in hadron collisions. Perturbation theory can be applied for the calculation of those high energy processes [1]. In contrast, for small momentum transfer the coupling constant becomes very large. As a consequence, low-energy quarks and gluons cannot propagate freely but are bound ("confined") into colorless bound states, the baryons and mesons. The baryons with three quarks and mesons with a quark and anti-quark can propagate freely and can be observed in experiments [1]. The fact that gluons carry color charge allows for gluon-gluon self interactions which are the reason for the color confinement [1].

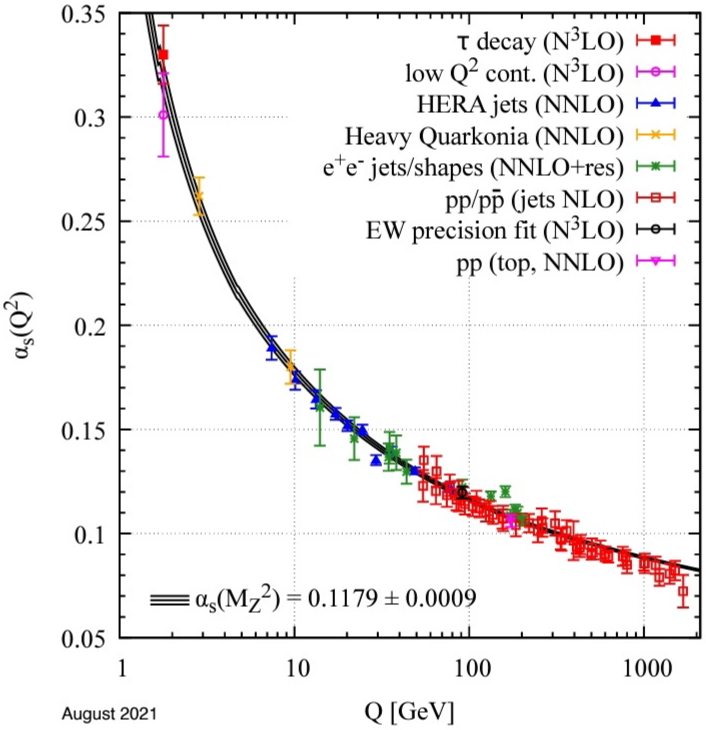

Figure 1.1.: Measurement of the coupling constant α_s. Figure taken from [4].

In the following a 2 → 2 process with large momentum transfer is discussed. High momentum processes as $q\bar{q} \to q\bar{q}$ occur in hadron collisions. The initial production of the two partons takes place via a high-Q^2 interaction, which is calculable in perturbative QCD (pQCD) [5]. As a result of the color confinement jets of hadrons are observed in the detector instead of the two initially produced partons. The jet production is explained in more detail in section 2.

In addition particle production from soft interaction is possible. In figure 1.2 the interaction between a quark and anti-quark pair (i) is depicted in a specific picture [1]. A quark and anti-quark are separated (ii) and the energy density between them increases with increasing distance. Finally the production of a new $q\bar{q}$ pair is energetically preferred (iii). This process is repeated (iv) until the energy is low

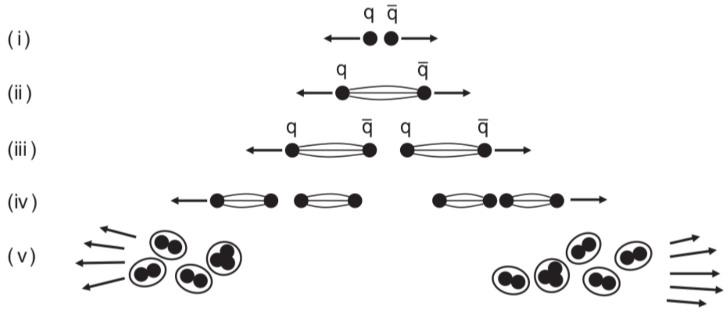

Figure 1.2.: Schematic representation of the hadronization process. Figure taken from [1].

enough and the quarks and anti-quarks combine into hadrons (v). As described in step (ii) it is expected that the exchange of virtual gluons between two quarks leads to constant energy density between them at large distances [1]. As consequence the energy between two quarks increases linearly with the distance and they can never be fully separated. Figure 1.3 shows the non-relativistic QCD color potential where the linear rise is visible at separations between the quarks above 0.25 fm with $\kappa = 1$ GeV/fm. At smaller distances the potential is proportional to $1/r$, where r is the distance between the quarks.

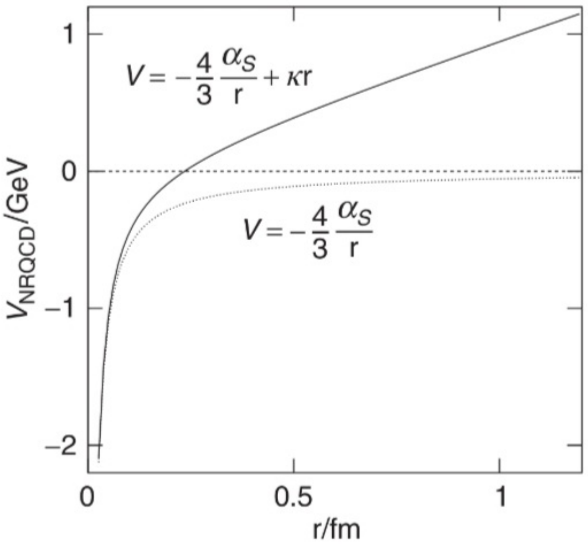

Figure 1.3.: Non-relativistic QCD potential between a $q\bar{q}$ pair. The short range potential between the $q\bar{q}$ pair is shown in the lower curve (dashed line) while the linear long range term was added in the upper curve (solid line) which dominates at r above 0.25 fm. Figure taken from [1].

In the next section the Quark-Gluon Plasma is introduced as a thermalized system of many quarks and gluons. In this many-body system new physics phenomena emerge. The exploration of these emergent features of QCD is the aim of heavy-ion physics.

1.2. Quark-Gluon Plasma

With the Standard Model of particle physics single particles and their interactions can be described. However, it turns out that the behavior of systems of many particles at macroscopic scales can not be predicted from their elementary interactions [6]. In particular with QCD the behavior of single quarks and gluons and the interactions between them are described. However, new physics phenomena appear if many of these quanta are put together. One example are phase transitions where emergent features of many-body systems appear.

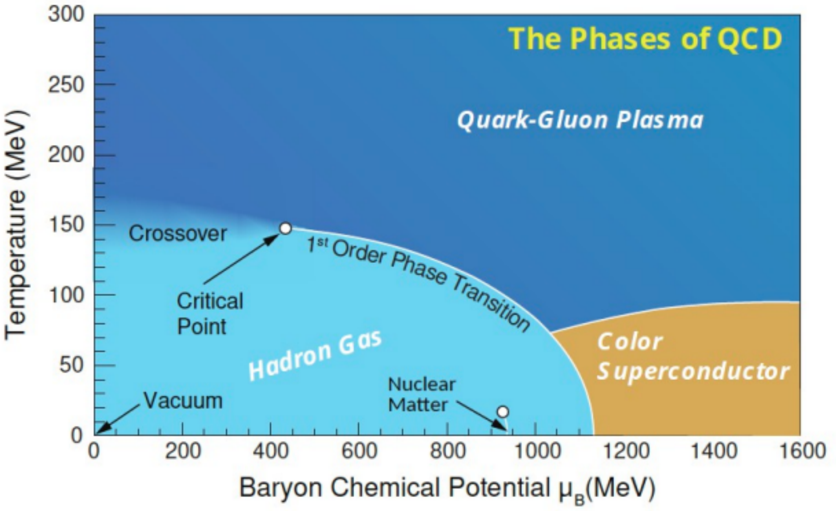

Figure 1.4.: Schematic representation of the QCD phase diagram. Figure taken from [7].

Figure 1.4 shows a sketch of the phase diagram of QCD matter based on parametric arguments [7]. The temperature is shown on the y-axis and the baryon chemical potential on the x-axis which quantifies the net-baryon content. At $\mu_\mathrm{B} \approx 0$ the baryon to anti-baryon ratio is one [5]. At low temperatures and densities the QCD matter is in the phase of a hadron gas. By increasing the temperature at vanishing chemical potential, a cross-over transition to the QGP at temperatures around 155 MeV [8] is shown. At non-vanishing chemical potential a finite order phase transition is predicted [2]. The cross-over from the QGP to the hadron gas at low chemical potential is expected as transition which happened in the early universe. The universe was in the state of decoupled quarks and gluons a few microseconds after the big bang [9]. In heavy-ion collisions this transition, as it happened in the early universe, can be reproduced in the laboratory [5]. In the following a lattice QCD calculation of the QGP at vanishing chemical potential is discussed.

A system of many non-interacting particles can be described by relativistic thermodynamics [2]. In order to describe a specific state of the system the relations between the state variables, the equations of states, have to be derived. In relativistic thermodynamics an ideal gas of identical point-like particles can be described with the Boltzmann statistics [2]. The energy density is described by the Stefan-Boltzmann law with the characteristic T^4 dependence.

In the case of quarks and gluons the Bose and Fermi-Dirac statistics are exploited [10]. From this an equation of the energy density of the system in dependence of the temperature can be derived as shown in equation 1.1 for the bosons.

$$\epsilon = \frac{\pi^2}{30} g_{\mathrm{DOF}} T^4 \tag{1.1}$$

The energy density depends on the temperature of the system and the degrees of freedom described by g_{DOF}. For the fermions the same T^4 dependence but with an additional factor is obtained. The degrees of freedom describe the different spin and color states and in the case of quarks the different flavor states.

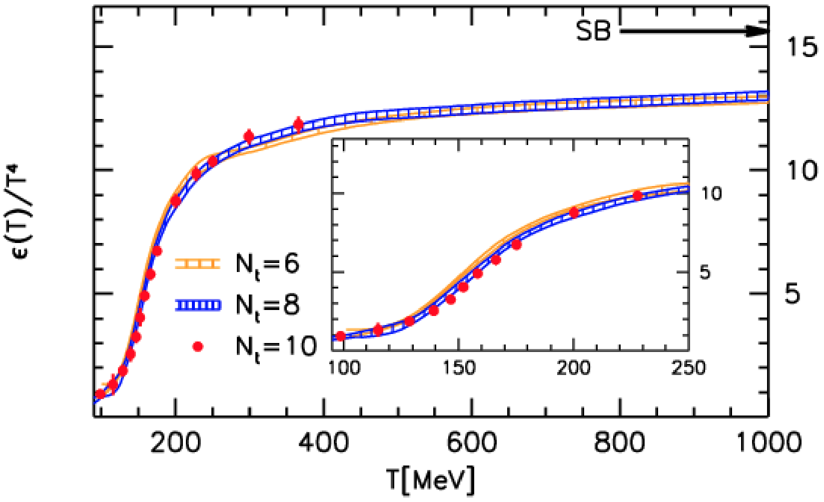

Figure 1.5.: Dependence of the energy density ϵ normalized by T^4 on the temperature calculated by lattice QCD. Figure taken from [11].

The running of the coupling constant α_{s}, shown in figure 1.1, implies that a QGP with temperature T below several GeV will be dominated by interactions in which the coupling is large. Therefore pQCD tools cannot be applied in this regime for the calculation of the QCD equation of state. They must be carried out using lattice QCD where space and time are discretized and the non-linear nature of the gluon self-interaction is fully accounted for [2, 8]. Figure 1.5 shows a lattice QCD calculation of a QGP with $n_{\mathrm{f}} = 2 + 1$ quark flavors, two light (u, d) quarks and one intermediate-mass (s) quark, at chemical potential $\mu_{\mathrm{B}} = 0$. The figure shows the energy density normalized by T^4 as a function of temperature of the system [11]. The different curves correspond to different choices of temporal discretization. At temperatures around 150 MeV a smooth cross-over is observed, as indicated in the sketch of figure 1.4, from a hadron gas to a new phase with more colored degrees of freedom. A large increase in the energy density is observed with a small change of the temperature, indicating a rapid transition in the nature of the degrees of freedom in the plasma. Above the transition region the rate of increase in ϵ/T^4 becomes smaller, and slow convergence is observed. While eventual convergence to the non-interacting Stefan-Boltzmann limit (indicated by the arrow) is indicated, it clearly will not be achieved until very high temperature, far beyond the range shown in the figure. At temperatures up to 1 GeV, a striking difference of about 15% is observed between the lattice calculations and the Stefan-Boltzmann limit. This indicates that the predominant degrees of freedom of the QGP in this temperature range are not freely-propagating quarks and gluons, but rather more complex bound states.

In heavy-ion collisions this system of many quarks and gluons, the QGP, can be produced. Studying this many-body QCD system, which can exhibit novel emergent behavior is the focus of heavy-ion physics. In heavy-ion collisions at the LHC (Large Hadron Collider) at CERN [12] or with RHIC (Relativistic Heavy Ion Collider) at the Brookhaven National Laboratory (BNL) [13] the QGP can be produced in the laboratory. Because the QGP itself is not directly measurable one has to find alternative ways of exploring its collective behavior, the temperature, density or viscosity and other properties. Observables as the radial and elliptic flow, photons and dileptons, as well as quarkonia can be used to get information about the QGP [2]. One possibility to study the behavior of the QGP is the measurement of jets in heavy-ion collisions as described in section 2. In the next section the formation of the QGP in the experiment is introduced.

1.3. Heavy-ion collisions

In heavy-ion collisions densities and temperatures high enough to generate deconfined strongly interacting matter are reached [14]. At the LHC at CERN lead nuclei are collided with energies up to $\sqrt{s_{\mathrm{NN}}} = 5.02$ TeV. Initial temperatures of more than 600 MeV and densities of about 14 GeV/fm^3 are reached at the LHC [10], which clearly exceeds the critical energy density of 0.6 to 1 GeV/fm^3 predicted by lattice QCD calculations [5]. The critical energy density is about four times larger than the density of normal nuclear matter which is 0.15 GeV/fm^3 [5].

Figure 1.6 shows a schematic representation of the space-time evolution from the collision to the production of hadrons in a heavy-ion collision [15]. At t = z = 0 the two nuclei collide and initial interactions of the partons and hard scatterings take place. After a formation time of 1-2 fm/c the thermalization of the QGP is achieved [2]. This thermalized system expands and cools. The hadronization begins after about 10 fm/c, when the critical temperature of $T_{\mathrm{c}} \approx 150$ - 160 MeV is reached, and quarks and gluons combine into hadrons. Inelastic collisions are possible until the temperature falls below the chemical freeze-out temperature $T_{\mathrm{ch}} \approx T_{\mathrm{c}}$. After that only elastic scattering takes place among the hadrons, which change their momenta but not their identity. Their momentum is only fixed when the so called kinetic freeze-out temperature $T_{\mathrm{fo}} \approx 100$ MeV is reached. The particles stream to the detectors, where their momenta are measured and they are identified, which is described in more detail in section 3.

The collision of two nuclei is called one event. The properties of the resulting fireball depend on the initial geometry of the collision [5]. The offset between the two colliding nuclei is called the impact parameter. The impact parameter can not be observed directly but can be inferred from global observables of the collision, for instance from the resulting multiplicity of the event or the transverse energy [5]. In

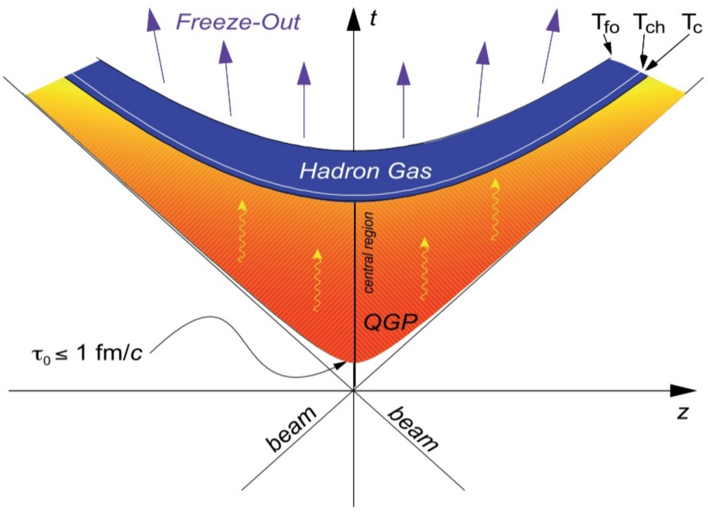

Figure 1.6.: Space-time evolution of a heavy-ion collision. Figure taken from [15].

addition the number of spectactor nucleons can be used to obtain information about the geometry of the collision [2]. These event properties are correlated in heavy-ion collisions and are generically called the centrality of the event. A centrality of 0-5% corresponds to the most central head-on events, where the impact parameter between the two nuclei is close to zero. In central collisions thousands of particles are produced within one event.

The geometry of the collision of the two nuclei can be described with the Glauber model [16]. The number of nucleons which participate in at least one inelastic collision N_{part} and the number of binary inelastic collisions N_{coll} in dependence of the impact parameter are calculated with this model.

1.3.1. Flow

Flow is discussed in this section as an emergent property of the QGP, which describes the collective behavior and expansion of the medium [17]. The azimuthally symmetric component of the collective flow is called radial flow. In non-central collisions the system does not expand isotropically. The expansion is influenced by the elliptic flow, another flow component, described in the following in more detail.

In figure 1.7 two colliding nuclei are depicted in a non-central collision along the z-axis. Their almond shaped overlap region is shown in the middle. The spatial anisotropy leads to azimuthal differences in the pressure gradient which results in a momentum anisotropy, depicted in the lower part of the figure. More particles are emitted in the reaction plane than out of the plane. This anisotropic behavior is quantified as the elliptic flow v_2 which is the second fourier coefficient in the fourier decomposition of the azimuthal particle distribution in equation 1.2 [18].

$$\frac{dN}{d\phi} \propto 1 + 2\sum\nolimits_{n=1}^{\infty} v_n(p_{\text{T}}) \cos(n\phi) \tag{1.2}$$

The angle ϕ is the angle relative to the reaction plane, which is defined by the impact parameter vector of the colliding nuclei and the beam axis [19]. In the estimation of the reaction plane only a finite number of particles can be used [20]. This estimated reaction plane with a finite resolution is called event plane.

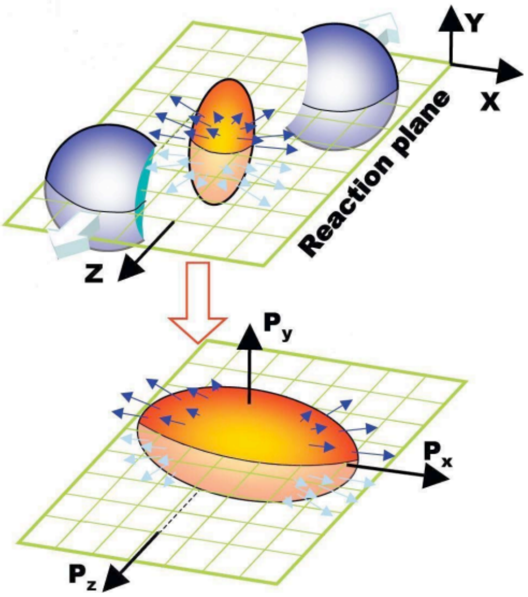

Figure 1.7.: Non-central collision of two colliding nuclei (upper) with the resulting momentum anisotropy in the transverse x-y plane (lower). Spatial (upper) and momentum (lower) coordinates are shown. Figure taken from [21].

By connecting experimental measurements of flow with models, information about the collective behavior of the QGP can be obtained. Such comparisons show that the dynamics of the QGP are well described by hydrodynamic models, which require a local thermodynamic equilibrium [22]. This requires that the free path length is small compared to the considered cell in the system, which is direct evidence that the constituents of the system are strongly-interacting [22]. The best description of the collective behavior and transport properties of the medium is obtained with viscous hydrodynamics [22]. By comparison with the measurement of the elliptic flow a small shear viscosity to entropy density ratio η/s was estimated, which is consistent with η/s for a strongly-coupled system [23, 17].

Spectra and elliptic flow data can be also described by the blast wave model [24]. A fully thermalized system and the freeze-out of all hadrons at the same time is assumed. In [25] a blast wave model with four free parameters was presented, which is used to simultaneously fit spectra and elliptic flow data. The spatial anisotropy is included in this blast wave model with an elliptical freeze out surface. In figure 1.8 the elliptic flow data measured at $\sqrt{s_{\mathrm{NN}}} = 2.76$ TeV with ALICE [26, 27, 28, 29] are depicted. The solid lines are the results from a fit with the blast wave model presented in [25]. The dashed lines are fit predictions. A very good description of the v_2 data at low p_{T} is obtained with the model. At higher transverse momenta the elliptic flow reduces due to the arising jet contribution. Jets as high p_{T} objects are introduced in more detail in the next section 2 where particles from the bulk play an important role in the background.

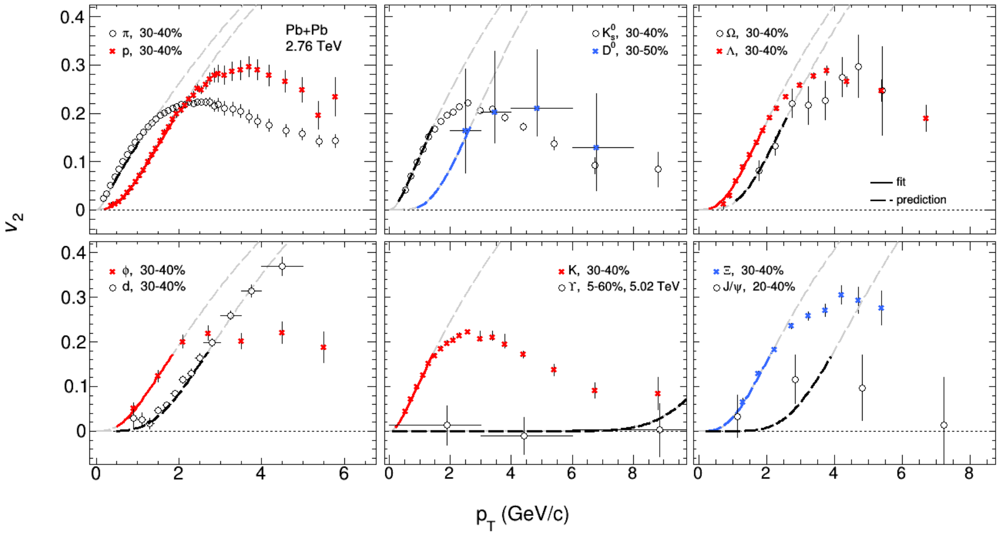

Figure 1.8.: Measurement of the elliptic flow at $\sqrt{s_{\rm NN}} = 2.76$ TeV and simultaneous blast wave fit results (solid lines) and predictions (dashed lines) of fits to v_2 and $dN/dp_{\rm T}$. Figure taken from [30].

1.3.2. Kinematic variables

The measured hadrons in heavy-ion and hadron collisions are usually characterized by the following variables [1]. The particles are described by their transverse momentum $p_{\rm T}$ and their mass m. The transverse momentum is given by equation 1.3, where the beam direction is defined by the z-axis.

$$p_{\rm T} = \sqrt{p_{\rm x}^2 + p_{\rm y}^2} \tag{1.3}$$

The position in the detector is described by the azimuthal angle ϕ and the pseudo rapidity η defined in equation 1.4. The angle θ is the angle relative to the beam direction. The pseudo rapidity can be treated as approximation of the rapidity $y = \frac{1}{2}\ln(E + p_{\rm z}/E - p_{\rm z})$ at high energies where $p \gg m$. The rapidity is a useful variable due to the boost invariance of rapidity differences along the beam direction [1].

$$\eta = -\ln\tan(\theta/2) \tag{1.4}$$

2. Jets in heavy-ion collisions

This section discusses the jet production in hadronic collisions. The description of jets in heavy-ion collisions follows, where jets are introduced as unique probes of the microscopic structure of the QGP. In addition experimental approaches for the heavy-ion jet measurement are discussed. This thesis focuses on the primary challenge of such measurements, the large uncorrelated background.

2.1. Jet production

In hadron collisions jets are produced in the initial hard scattering of partons, the quarks and gluons, from the projectiles [2]. The resulting objects are highly virtual [31], which means they are off-shell and temporarily violate the Einstein energy–momentum relation [1]. They lose their virtuality through radiation in a gluon shower ("fragmentation") until the gluons become very soft [31]. The gluon shower terminates and their combination into hadrons starts. This process is known as hadronization.

In figure 2.1 a sketch of the different phases of jet production in a proton-proton collision is depicted. The production of the energetic parton in the p+p collision is shown on the left side. Next to the collision the fragmentation process of the parton due to the successive radiation of gluons is depicted. The hadronization follows as last stage before the hadrons are detected.

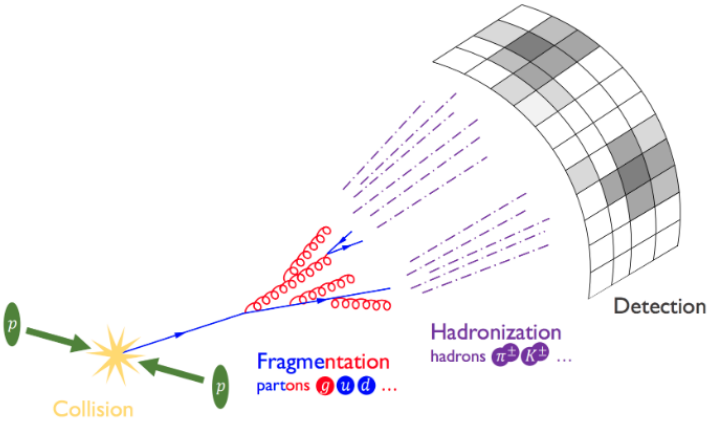

Figure 2.1.: Schematic representation of jet production in a p+p collision. Figure taken from [32].

2.1.1. Factorization

The description of jets as distinct objects in the final state of the hard scattering of two partons is based on the factorization theorem [33]. The initial state, the hard scattering of the partons, and the final state are independent without quantum mechanical interference. Thus the calculation of the production rate of a certain process can be carried out by multiplying the probabilities and not the amplitudes [31].

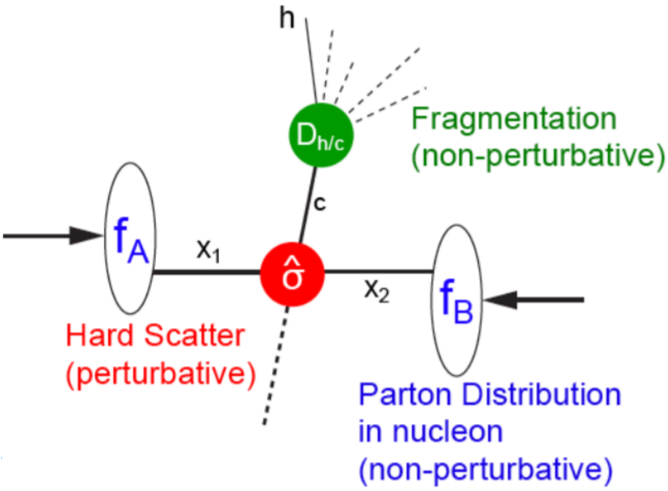

Figure 2.2.: Schematic representation of the factorization theorem. Figure taken from [10].

The factorized expression of the differential cross-section for inclusive hadron production, $AB \to hX$, is shown in equation 2.1 [5]. In this example two partons a and b with momentum fraction x_1 and x_2 from the incoming nuclei A and B with momentum P and $-P$ scatter and produce an outgoing parton c. The hadron h carries momentum fraction z of the full jet momentum.

$$d\sigma^{\text{hard}}_{\text{AB}\to\text{h}} = f_{\text{a/A}}(x_1, Q^2) \otimes f_{\text{b/B}}(x_2, Q^2) \otimes d\sigma^{\text{hard}}_{\text{ab}\to\text{c}}(x_1, x_2, Q^2) \otimes D_{\text{c}\to\text{h}}(z, Q^2) \tag{2.1}$$

The three individual factorized components of the cross-section are schematically represented in figure 2.2: The parton distribution functions (PDF) $f_{\text{a/A}}(x_1, Q^2)$ and $f_{\text{b/B}}(x_2, Q^2)$, the cross-section $d\sigma^{\text{hard}}_{\text{ab}\to\text{c}}(x_1, x_2, Q^2)$ of the two scattered partons a and b and the fragmentation function (FF) $D_{\text{c}\to\text{h}}(z, Q^2)$.

All components depend on the momentum transfer Q^2 of the process. As discussed in section 1.1 the coupling strength depends on the energy scale and determines if a process is calculable in pQCD or not. The cross-section of a hard (high Q^2) parton-parton collision is calculable in pQCD as a convergent series in α_s, since $\alpha_s(Q^2 \to \infty) \to 0$ in high energy processes [5]. The PDF $f_{\text{a/A}}(x_1, Q^2)$ ($f_{\text{b/B}}(x_2, Q^2)$) gives the probability that a parton a (b) with momentum fraction x_1 (x_2) of the incoming nucleon participates in the collision while the FF $D_{\text{c}\to\text{h}}(z, Q^2)$ represents the probability that a hadron h with momentum fraction z of the momentum from the produced parton c is created. The PDF and FF are sensitive to low Q^2 physics which is non-perturbative, whereas the hard cross-section has high Q^2 and can therefore be calculated perturbatively [5].

While the absolute magnitude of the PDF and FF must therefore be extracted from data, their evolution obeys the linear DGLAP (Dokshitzer–Gribov–Lipatov–Altarelli–Parisi) equations [31]. Due to their dependence on the energy scale they have to be measured at one certain scale, and are universal functions independent of the scattering process [34, 35]. The PDF can be measured for example in deep inelastic scatterings while the FF is measured in e^+-e^- collisions [5].

2.2. Jet quenching

In heavy-ion collisions the QGP, a thermalized system of quarks and gluons, is produced. In addition, jets are produced in the initial hard scatterings of partons. The produced high energetic partons interact with the medium while the jet shower evolves [31]. In figure 2.3 a sketch of the jet production in p+p (left) and A+A (right) collisions is shown. On the right side the modification of the jet by gluon radiation in the medium is depicted. Due to the interaction with the medium, the jet shower is modified, as discussed in the next section. Modifications in the jet energy, the jet structure as well as the deflection of the jets are possible results of the interaction with the medium. These effects are called jet quenching [31]. By measuring the jet quenching, information about the structure and the dynamics of the QGP could be derived.

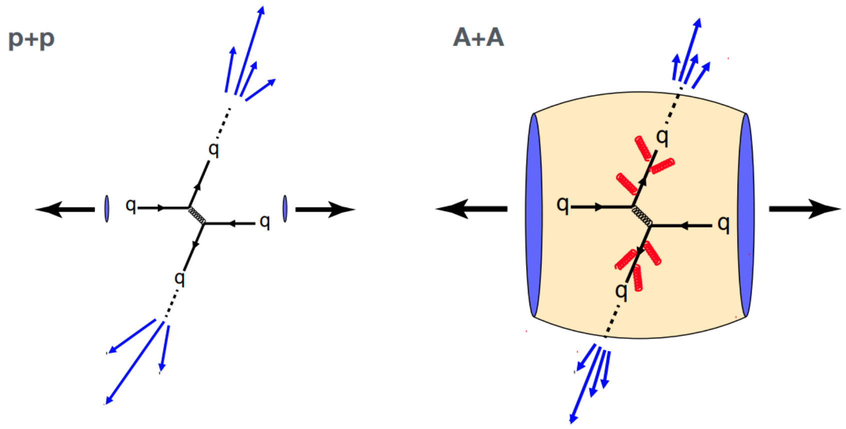

Figure 2.3.: Schematic representation of jet production in p+p (left) and A+A (right) collisions, where the gluon radiation is indicated. Figure taken from [10].

2.2.1. Theoretical considerations

In this section the different mechanisms for jet quenching are described. In the case of a heavy-ion collision the scattered energetic partons undergo several interactions in the medium before they hadronize. There are two main interaction processes of jets in the QGP, the collisional and radiative energy loss [31]. Similar to the energy loss of a charged particle in ordinary nuclear matter, the dominant mechanism of the energy loss of a parton in the QGP depends on the energy scale. Low momentum particles mainly lose their energy in elastic collisions with the constituents of the medium. As shown in the left sketch of figure 2.4 the four-vector ΔE is exchanged by a gluon. Collisional energy loss was already described in 1982 by Bjorken [36]. The dominating mechanism for high momentum particles is the radiative energy loss, represented in the right sketch of figure 2.4. In this case the fast parton radiates a gluon with energy ΔE as result of inelastic scattering.

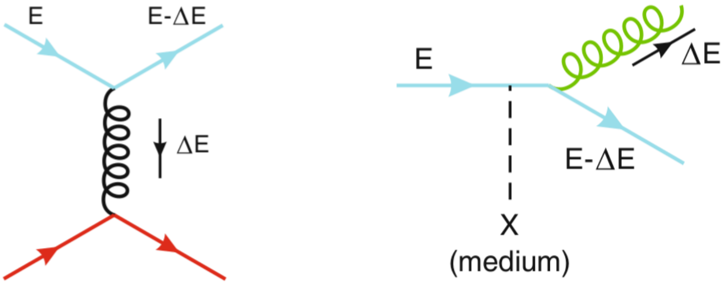

Figure 2.4.: Collisional (left) and radiative (right) energy loss of a parton in the QGP. Figure taken from [5].

In addition to the properties of the particle which experiences the energy loss in the medium, the amount of ΔE depends on the nature of the medium as its temperature T, the coupling strength α and the dimension L [5]. Other important variables are the mean free path λ of the particle in the medium and the number of scattering centers $N = L/\lambda$. These parameters are used in models like the BDMPS (Baier, Dokshitzer, Müller, Peigné, and Schiffer) model [5], which is one example of a theory formulation where multiple soft scatterings are assumed.

The variable $\hat{q}$, described by equation 2.2, is the transport coefficient of the medium, which encounters for the medium modified radiation.

$$\hat{q} = \frac{\mu^2}{\lambda} \tag{2.2}$$

If a quark or gluon scatters with a particle from the medium, the medium transfers a momentum μ to the scattered particle.This momentum transfer μ is the inverse of the screening length, the Debye mass [5] $\mu \propto \sqrt{\alpha_s}T$.

The time for the emission of a gluon is given by the coherence time or length z_c, which is approximately the energy of the gluon divided by its transverse momentum squared [2]:

$$z_c \simeq \frac{\omega}{k_{\mathrm{T}}^2} \tag{2.3}$$

If the scattered particle passes n_c scattering centers during the emission of a gluon, the obtained transverse momentum of the gluon is given by $k_{\mathrm{T}}^2 \simeq n_c\mu^2$, where $n_c = z_c/\lambda$ can be expressed as the coherence length divided by the mean free path. This results in an expression of the coherence length given in equation 2.4, where μ^2/λ is expressed as the transport coefficient $\hat{q}$ [2].

$$z_c \simeq \sqrt{\frac{\lambda}{\mu^2}\omega} = \sqrt{\frac{\omega}{\hat{q}}} \tag{2.4}$$

One distinguishes incoherent scattering, where $\lambda > z_c$, and coherent scattering with $\lambda < z_c$. In the case of coherent scattering destructive interference leads to a reduction of ΔE as described by the Landau-Pomeranchuk-Migdal (LPM) effect [2]. The LPM effect is a general quantum effect that occurs if scattering centers are dense, such that the mean distance between them is less that the time it takes for the radiation.

The soft and hard radiation of a gluon depends on the characteristic gluonstrahlung $\omega_c = 1/2\hat{q}L^2$ [5]. The energy loss for the two cases are described by equation 2.5 and 2.6 where C_R are the color factors. They describe the coupling strengths between the different QCD vertices. For a quark which radiates a gluon $q \to gq$ the coupling strength is proportional to $\alpha_s C_\mathrm{F}$, where $C_\mathrm{F} = (N_\mathrm{c}^2 - 1)/(2N_\mathrm{c)} = 4/3$ with $N_\mathrm{c} = 3$ are the three colors. For the gluon vertex $g \to gg$ it is $\alpha_s C_\mathrm{A}$ with $C_\mathrm{A} = N_\mathrm{c} = 3$. This results in a larger multiplicity for gluon jets than for quark jets because the average number of radiated gluons is $C_\mathrm{A}/C_\mathrm{F} = 9/4$ times larger for gluons than for quarks [5]. At the same time the p_T of the constituents is lower in the gluon jets. The energy loss for charm and bottom quarks is expected to be smaller than for the lighter up, down and strange quarks. The reason is the suppression of gluon emission by a heavy quark within angles smaller than $\theta = M/E$, with respect to the flight direction, where M is the mass of the quark and E its energy. This effect is known as the dead cone effect [5].

$$\Delta E_\mathrm{rad} \approx \alpha_s C_\mathrm{R} \hat{q} L^2 \qquad (\omega < \omega_c) \tag{2.5}$$

$$\Delta E_\mathrm{rad} \approx \alpha_s C_\mathrm{R} \hat{q} L^2 \ln\left(E/(\hat{q}L^2)\right) \qquad (\omega > \omega_c) \tag{2.6}$$

In experiments several aspects which modify the description of energy loss as described in this section have to be taken into account. For example the considered medium is expanding and its properties as the Debye mass and transport coefficient are dependent on the position. There are several models which try to deal with those difficulties as presented in [31, 37].

2.2.2. Experimental evidence for jet quenching

The first measurement of jet quenching was the hadron yield suppression at high p_T [38] and the azimuthal distribution of jet production [39, 40, 41]. The measured nuclear modification factor R_AA as given in equation 2.7 provided evidence for jet quenching.

$$R_\mathrm{AA} = \frac{(dN/dp_\mathrm{T})_{AA}}{N_\mathrm{coll}(dN/dp_\mathrm{T})_{pp}} \tag{2.7}$$

It is defined as the ratio between the yields of a certain particle species in the medium (A+A) and in the vacuum (p+p) and measures the modification of the inclusive hadron yield. Scaled by the number of collisions N_{coll} the ratio R_{AA} is expected to be unity in case of no modification in the medium. In measurements a clear deviation from this was observed with a suppression of the R_{AA} by a factor 5 for the π yield [38, 42] as shown in figure 2.5. As reference the photon spectra were used, where $R_{\text{AA}} \approx 1$ for $p_{\text{T}} > 3$ GeV was found.

The measured suppression of the inclusive hadron yield is a result of a shift in the p_{T} distributions to lower values in the case of heavy-ion collisions. With the measurement of the inclusive hadron suppression evidence for jet quenching was found. However, only single particles are considered and different aspects of jet quenching are neglected. In order to study jet quenching effects as the modification of the jet structure or modifications in the jet energy, where a fraction of the energy is transported away from the leading particle, the jet reconstruction is necessary. This is discussed in the next section.

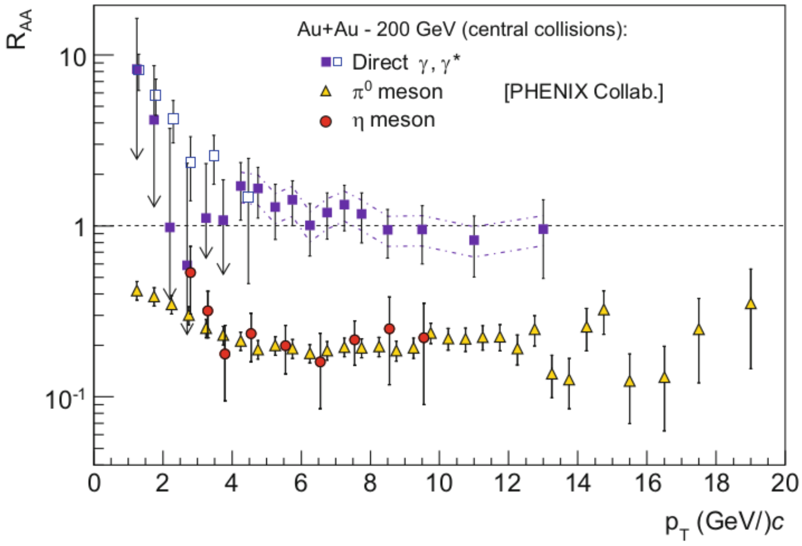

Figure 2.5.: Measurement of R_{AA} at $\sqrt{s_{\text{NN}}} = 200$ GeV for π^0, η and direct photons for comparison. Figure taken from [2].

Measurements of jet-hadron or di-hadron correlations are done by selecting a high p_{T} trigger hadron or jet and measuring the associated particles at $\Delta\phi = \phi - \phi_{\text{trigger}}$ and $\Delta\eta = \eta - \eta_{\text{trigger}}$ [39, 43]. In p+p collisions two back-to-back jets in the azimuthal direction at ϕ (near-side) and $\phi + 180$ deg. (away-side) are observed. In comparison to that, the away side jet is suppressed in the case of Pb+Pb collisions, due to the energy loss in the QGP. The jet p_{T} is shifted to lower energies and in addition the jet is deflected by an angle $\Delta\phi$ in the azimuthal direction as consequence of the scattering. In addition to the jet correlations particle correlations can be a result of the hydrodynamic flow [39]. Low p_{T} particles participate in the collective behavior of the medium. Particle correlations are induced by the elliptic flow due to anisotropies in the collision, as described in the previous section.

2.3. Experimental measurements of jets

In this section the measurement of jets with jet reconstruction algorithms are presented as well as the handling of uncorrelated background in heavy-ion jet measurements. There are several different steps in the measurement of jets. They are determined by the selected jet reconstruction algorithm, the background estimation and the applied corrections [5].

The biggest issue of jet analysis in heavy-ion collisions, which distinguishes them from p+p jet measurements, is the huge amount of background particles. The general major difficulty is the high precision reconstruction of low energy jets.

In this section the FastJet package [44] as a tool which provides several jet reconstruction algorithms is introduced, as well as two different approaches of jet measurements carried out by ALICE and STAR (Solenoidal Tracker at RHIC). In particular a new approach for the estimation of the uncorrelated background, presented by STAR [45], is described in section 2.3.2.

2.3.1. Jet reconstruction with FastJet

In order to study jets and jet quenching effects, the jet reconstruction is performed to recover the partonic kinematics. As shown in figure 2.1 the resulting hadrons from the fragmentation and hadronization process of the partons are measured in the detectors. Jet algorithms were developed to assign the measured hadrons to jets. In jet algorithms a setup for the clustering of jets is defined, which makes the results reproducible [44]. In general the jet algorithms are required to be infrared and collinear safe. This is necessary to ensure that the resulting jet, with its energy and strucutre, is independent of the details of the hadronization. An algorithm is infrared safe if an additional soft particle between two jets does not lead to the reconstruction of one large jet [46]. A collinear safe algorithm is not sensitive to the splitting of a 4-vector into smaller components. Thus the jet reconstruction and the energy stays the same, even if a particle is split into two collinear objects which together have the same energy as before.

The FastJet software package [44] provides several tools and jet finding algorithms. Jet finding algorithms can be categorized into cone and sequential recombination algorithms. In the first case all particle momenta within a cone of radius R around a seed particle i, for example the particle with the largest momentum, are summed [5]. The resulting vector defines the new seed and the procedure is repeated until the direction of the combined vector is fixed. For sequential recombination algorithms a distance measure and a cut off are defined [44]. The particles with the smallest distances according to the distance measure are combined as long as the criterion for the abortion of the process is reached.

The k_{T} algorithm is a common example for a sequential recombination algorithm. The distance measure d_{ji} between particles i and j is defined in equation 2.8 with the transverse momentum p_{Ti} of particle i.

$$d_{\mathrm{ij}} = d_{\mathrm{ji}} = min(p_{\mathrm{Ti}}^2, p_{\mathrm{Tj}}^2)\frac{\Delta R_{\mathrm{ij}}^2}{R^2} \tag{2.8}$$

The distance is calculated as the minimum of the squared transverse momenta of particle i and j times $\Delta R_{\mathrm{ij}}^2 = (y_\mathrm{i} - y_\mathrm{j})^2 + (\phi_\mathrm{i} - \phi_\mathrm{j})^2$ which is the sum of the squared differences between the rapidities y_i and y_j and the azimuthal angles ϕ_i and ϕ_j of particle i and j. The jet resolution parameter is defined by R, which is called the jet radius.

One advantage of FastJet is the reduction of the computation time [44]. The clustering needs to be done for millions of events which all have multiplicities of a few thousand. For a multiplicity of N there are $O(N^2)$ distances and $O(N)$ iterations. To minimize the computational effort, the problem is reduced to the search for the geometrical nearest particle j that minimizes ΔR_{ij} for a given particle i. Different aspects reduces the computation time, as the fact that if i and k are near and j and k are near particles then particles i and j have to be near too.

Another common algorithm used for the jet finding in heavy-ion collisions is the anti-k_T algorithm. The distance measure of the anti-k_T algorithm is similar to that of the k_T algorithm but with inverse momentum as shown in equation 2.9. The distance between a particle i and the beam is defined as $d_{\mathrm{iB}} = p_{\mathrm{Ti}}^{-2}$.

$$d_{\mathrm{ij}} = d_{\mathrm{ji}} = min(1/p_{\mathrm{Ti}}^2, 1/p_{\mathrm{Tj}}^2)\frac{\Delta R_{\mathrm{ij}}^2}{R^2} \tag{2.9}$$

If the smallest distance d_{ij} between particles i and j are found the particles are combined by adding the components of their 4-momenta. This default recombination scheme is called *E-scheme*. Other schemes and possible settings are described in the manual [44]. If the distance d_{iB} is the smallest, particle i is identified as the final jet.

In addition to the definition of the jet algorithms different cuts are provided in FastJet which can be applied to the jets, for example a p_T and fiducial cut. The jet area is the spatial distribution of the jet in the $y - \phi$ plane. For an active area very soft, randomly generated ghost particles are distributed over the full range. They do not affect the reconstruction of the jets but can be a measure of the jet area (area $\propto$ number of ghosts). Other area definitions are described in the manual [44].

The major difficulty that arises for jet finding in heavy-ion collisions is the large amount of background particles. A measure of the background on an event-by-event basis is ρ, the median of the p_T/A distribution as shown in equation 2.10, where A is the area of the jet.

$$\rho = median\left\{\frac{p_{\mathrm{T,jet}}^{\mathrm{raw,i}}}{A_{\mathrm{jet}}^{i}}\right\} \tag{2.10}$$

The obtained ρ is subtracted from the raw jet p_T of jet i by scaling it with the appropriate jet area $A_{\mathrm{jet}}^{\mathrm{i}}$.

$$p_{\mathrm{T,jet}}^{\mathrm{reco,i}} = p_{\mathrm{T,jet}}^{\mathrm{raw,i}} - \rho \cdot A_{\mathrm{jet}}^{\mathrm{i}} \tag{2.11}$$

However, ρ is only a rough estimation of the background energy density, which does not take into account local fluctuations. In the next section two approaches for the measurement of the uncorrelated background presented by ALICE and STAR are introduced.

2.3.2. Heavy-ion jet analysis

As described in the previous section, jets can be reconstructed with several jet algorithms. To account for the large combinatorial background, often cuts on the reconstructed jet p_{T} are applied. For example in [47] the ALICE collaboration presented a jet measurement in Pb+Pb collisions at $\sqrt{s_{\mathrm{NN}}} = 2.76$ TeV. In order to suppress the uncorrelated background, only jets with $40 < p_{\mathrm{T}} < 120$ GeV/c in central (0-10%) events were used, and in addition only jets with at least one constituent with a momentum larger than 5 GeV/c are selected. The problem with selecting those high p_{T} processes is the bias against jets that have lost significant energy due to quenching. These jets have experienced the greatest interaction in the QGP and are of particular interest in the measurement of jet quenching.

One approach for the background estimation was presented by ALICE [48], where the measurement of jet quenching with a semi-inclusive charged jet spectrum was done. In the analysis jets recoiling from a high p_{T} charged trigger hadron are used which implies the selection of high p_{T} processes. A schematic representation of such a process is shown in figure 2.6, where a recoiling jet at $\Delta\phi$ with respect to the trigger hadron is depicted. No cut on the p_{T} of the selected recoil jets is applied. To account for the combinatorial background, different trigger intervals are used. Recoiling jets from trigger hadrons with $20 < p_{\mathrm{T}} < 50$ GeV/c are used for the signal distribution and jets recoiling from hadrons with $8 < p_{\mathrm{T}} < 9$ GeV/c as reference for the background which is subtracted from the signal. This method enables jet measurements down to 20 GeV/c as reported in [48].

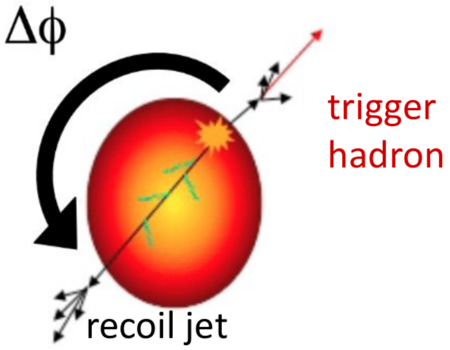

Figure 2.6.: Schematic representation of the recoiling jet at $\Delta\phi$ from a high p_{T} trigger hadron. Figure taken from [49].

In [45] a unique and purely statistical approach to identify lower p_{T} jets was presented by STAR in 2017. They investigated the jet quenching effect in $\sqrt{s_{\mathrm{NN}}} = 200$ GeV Au+Au data, measured with the STAR detector at RHIC. In this analysis a mixed event technique was applied for the estimation of the uncorrelated background. This offers the possibility of jet measurements down to very low p_{T} for the first time. Similar to the analysis in [48] the semi-inclusive hadron-jet (h-jet) distribution was measured with a trigger hadron within $9 < p_{\mathrm{T}} < 30$ GeV. If the trigger hadron is emitted at $\phi_{\mathrm{trigger}} = 0$, jets in the recoil acceptance with $\frac{3}{4}\pi < \phi_{\mathrm{jet}} < \frac{5}{4}\pi$ are used. The event selection is carried out by this requirement of a trigger hadron in the p_T interval. Background fluctuations, resulting in p_T smearing as well as detector effects are corrected with an unfolding procedure.

As mentioned above the uncorrelated background is obtained by the mixed events which are composed of particles each from a different real event. The same jet reconstruction is carried out for the produced mixed event as for the real events which results in the reconstruction of only uncorrelated background jets.

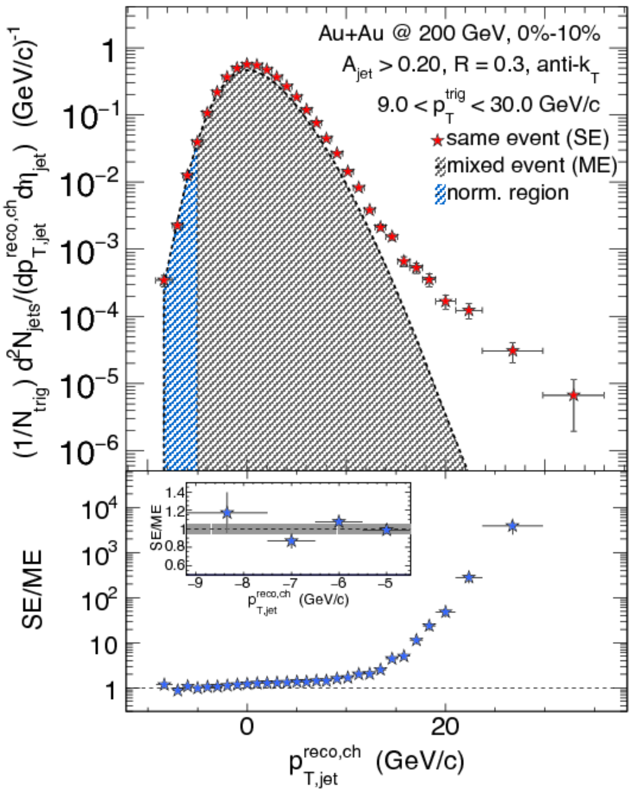

Figure 2.7.: Distribution of $p_{\mathrm{T,jet}}^{\mathrm{reco,ch}}$ of the recoiling jets from a $9 < p_\mathrm{T} < 30$ GeV/c trigger hadron. The jets are reconstructed with the anti-k_T algorithm with $R = 0.3$ and an area cut of $A_{\mathrm{jet}} > 0.2$. The SE distribution is represented by red stars, the ME as black shaded region and the normalization region is depicted in blue. The lower panel shows the ratio SE/ME. Figure taken from [45].

Figure 2.7 shows the raw distribution of the reconstructed charged jet $p_{\mathrm{T,jet}}^{\mathrm{reco,ch}}$ for the data, labeled with SE (red) and the ME (black) as presented in [45]. The blue shaded region is the normalization region. In the lower panel the ratio SE/ME is depicted. They found a very good agreement of the ME with the SE at $p_{\mathrm{T,jet}}^{\mathrm{reco,ch}} < 0$, where the reconstructed jets are expected to be combinatorial fake jets.

In [45] the corrected recoil jet yield measured in central and peripheral collisions was compared and a strong suppression in central collisions was found. The suppression decreases for increasing jet radius R, which indicates a transport of p_T to regions outside the jet radius in central collisions, due to the interaction of the jet with the medium. Indications for intra-jet broadening were not found by comparing the recoil jet yields for different jet radii R. The quasi-particle nature of the medium could be investigated by the recoil jet azimuthal distribution. An increase at large angles with respect to the jet axis might be an indication for large-angle Molière scattering [50]. They found an 90 % statistical confidence upper limit of $50 \pm 30(\mathrm{sys})\%$.

2.4. Overview

Jets are introduced above as unique probes of the QGP. For the measurement of jets in p+p and heavy-ion collisions, the anti-k_{T} algorithm has been established as tool for the jet reconstruction. However, in the reconstruction of jets in heavy-ion collisions, the signal-to-background ratio is very small for low and moderate p_{T} jets. The huge amount of background particles leads to the reconstruction of a large fraction of uncorrelated background jets. This combinatorial background often limited the jet measurements to high p_{T}. Cuts on the reconstructed jets or other biases were applied, in order to reduce the background. However, there are many low p_{T} jets which are allowed in QCD and which aren't studied yet. In addition the jets, which interact strongly with the QGP may no longer be high p_{T} objects, but rather disappeared in the background.

In this thesis the technical limitation of the jet measurements due to the large uncorrelated background is addressed. A novel mixed event technique, which was successfully used in [45] for the h-jet measurement, is applied for the first time to a measurement at higher LHC energies. The purpose of the studies presented in this thesis is an unbiased jet measurement down to very low p_{T}. The limits of pQCD could be tested by studying the correlations above the low p_{T} background.

In the following the ALICE detector is described in section 3 and the used data set with the applied track selection follows in section 4. In section 5 the analysis strategy is presented where the focus is on the mixed event technique. It turns out that several aspects of the mixed event technique have to be improved for the applicability to jet measurements at ALICE, which are presented in this thesis. Different systematic studies are carried out in the following section 6. The raw uncorrected jet distributions are presented in section 7 and the unfolding procedure which is used for the correction of the raw distributions follows in section 8. In the last section a brief summary and outlook of the presented studies are reported 9.

3. The ALICE Experiment at LHC

ALICE (A Large Ion Collider Experiment) is one of the four large experiments at the LHC at CERN [12]. The European Organization for Nuclear Research (CERN) is located near Geneva and was founded in the beginning of the 1950s [51]. Today it is one of the largest physics laboratories in the world. CERN has about 2500 staff members from 23 different states and about 13000 scientists from 70 different countries which participate in research [52].

In 1959 protons were accelerated up to an energy of 28 GeV for the first time by the Proton Synchrotron (PS) [53]. About 15 years later the Super Proton Synchrotron (SPS) went into operation. This was the first underground accelerator in 40 m depth at CERN with a circumference of 7 km. Protons and later antiprotons were accelerated up to $\sqrt{s_{\mathrm{NN}}} = 540$ GeV which made the first measurement of the W and Z bosons possible [54]. In 1986 the investigation of heavy ion collisions began by accelerating ions as oxygen, sulphur and later lead with the SPS. Today the SPS is used as a pre-accelerator before the proton or lead-ions are induced to the LHC.

The LHC was build within the Large Electron Positron Collider (LEP) tunnel which was used until 2000 to accelerate electrons and positrons. It has a circumference of 27 km and is placed 100 m in underground [55]. The LHC is the largest and most powerful particle accelerator in the world. Energies of $\sqrt{s_{\mathrm{NN}}} = 13$ TeV in proton-proton collisions and $\sqrt{s_{\mathrm{NN}}} = 5.02$ TeV in Pb+Pb collisions are reached. The particle beams have nearly speed of light when they brought into collision. A luminosity of $10^{34}\mathrm{s}^{-1}\mathrm{cm}^{-2}$ is reached for the proton collisions [55]. The product of the cross-section and the integrated luminosity, which depends on the number of particles within a bunch and their frequency, defines the number of interactions [1].

To keep the beams on their circular track 1232 superconducting dipole magnets are used [12]. In addition there are 392 quadrupole magnets to focus the beams, in particular just before the collision takes place. For the cooling of the superconducting magnets to temperatures of 1.9 K, liquid helium is used and within the beam pipes a ultrahigh vacuum is produced.

The LHC went into operation in 2008 [53]. The first data taking period (Run 1) was from 2009 to 2013 and the data of Run 2 was taken between 2015 and 2018. After a long shutdown the third run of the LHC is starting in 2022.

There are four large experiments, ALICE, ATLAS, CMS and LHCb at the four collision points of the LHC. The LHCb detector was build for precision measurements to search for physics beyond the Standard Model [56]. In 2012 the Higgs Boson was detected for the first time by ATLAS and CMS [3]. This confirmed the Higgs mechanism and the Nobel Prize was awarded one year later to Peter Higgs und François Englert [57]. The ALICE detector is designed for the measurement of heavy-ion collisions [58]. Due to the high energy and density in heavy-ion collisions, where temperatures 100000 times hotter than the sun are reached, the QGP can be produced. Studying the behavior of the new state of QCD matter and gaining information about the properties of the QGP is the main aim of the ALICE experiment. The hadrons which are produced after the freeze-out of the QGP are measured with the large detector system of ALICE. In the following section the ALICE detector is described in more detail.

3.1. ALICE detector system

The ALICE detector is constructed for the investigation of the QGP produced in Pb+Pb collisions at energies up to $\sqrt{s_{\mathrm{NN}}} = 5.02$ TeV. Therefore it is necessary to identify and reconstruct thousands of particles produced in the hadronization process of one event. In order to achieve this, the ALICE detector is composed of many sub-detectors which are used for tracking and particle identification.

A schematic representation of the detector system is shown in figure 3.1. The whole detector is 26 m long, 16 m high and 16 m wide with a weight of 10000 tons [55]. It can be categorized into the central-barrel detectors, forward detectors and the MUON spectrometer [59]. The forward detectors are mainly used for the event categorization, as the determination of the centrality and for triggering. The central-barrel detector system is surrounded by a magnet with a magnetic field of up to 0.5 T. It allows the identification of charged particles and the measurement of their transverse momenta between 0.15 and 100 GeV/c with resolutions of 1.5 % up to 10 GeV/c [59]. In the following the main tracking and particle identification detectors are described.

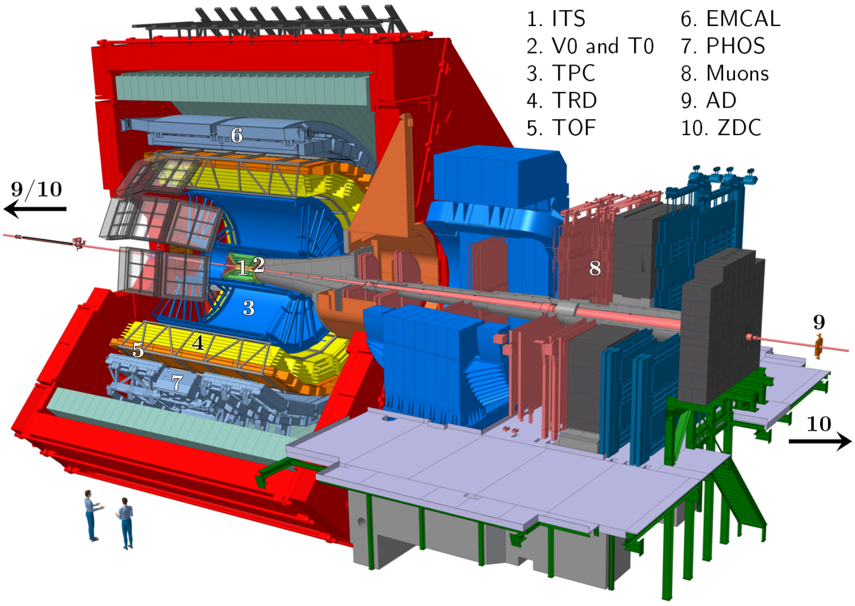

Figure 3.1.: ALICE detector system. Main central-barrel detectors used for tracking and particle identification: ITS (green), TPC (blue), TRD (yellow), TOF (orange) and EMCal (grey). They are placed inside a solenoidal magnet (red). Figure taken from [60].

3.1.1. ITS

The most inner detector, shown in green in figure 3.1, is the Inner Tracking System (ITS) which is 3.9 cm away from the collision point in the center. The described ITS was used during Run 2, which is replaced by a new ITS in the meantime for Run 3. The six cylindrical layers of the ITS are the two from the Silicon Pixel Detector (SPD) and two each of the Silicon Drift Detector (SDD) and Silicon Strip Detector (SSD) [61]. It is mainly used for the reconstruction of primary and secondary vertices with resolutions better than 10 (100) micrometer for the primary (secondary) vertex [62]. In addition the momentum resolution of the TPC (Time Projection Chamber) reconstructed tracks can be improved and low momentum particles with $p_{\mathrm{T}} < 100$ MeV/c can be measured with the ITS [61].

3.1.2. TPC

The TPC, depicted in blue, follows as next detector around the ITS. The TPC is designed for the tracking of charged particles and particle identification [63]. It has a length of 500 cm in beam direction and an inner and outer radius of 80 and 250 cm. The acceptance of the TPC is $|\eta| < 0.9$. A schematic representation of the TPC is shown in figure 3.2. The TPC is filled with gas (neon or argon mixed with CO_2) which is ionized when a charged particle travels through the volume. The free electrons along the track drift to the readout chambers at the end of the cylinder due to an electric field of 400 V/cm, produced by a high voltage of 100 kV at a central electrode. For the readout, multiwire proportional chambers were used [64] in Run 2. As explained later they are replaced by new Gas Electron Multiplier (GEM) foils for Run 3. In azimuthal direction the readout system is divided into 18 segments of chambers, each used for the measurement within an angle of 20°. Each segment is divided into an inner and outer part in radial direction due to the radial dependence of the track density. The x-y position can be measured directly with the multiwire proportional chambers while the z-component is determined from the drift velocity and time of the electron. Its drift velocity stays constant because the acceleration due to the electric field and the energy loss due to the scattering are assumed to be in balance. The energy loss of the particle is proportional to the measured signal and thus the identity of the particle can be estimated by exploiting the Bethe-Bloch formula [1]. The magnetic field enables the determination of the particles momenta and charges by measuring the radius of the track.

3.1.3. TRD

The Transition Radiation detector (TRD) is shown in yellow in figure 3.1 next to the TPC. It has an inner and outer radius of 290 to 368 cm [65]. The working principle is based on the electromagnetic radiation which is emitted when a highly relativistic charged particle travels through layers with different dielectric constants (radiators). This transition radiation depends on the Lorentz factor γ of the particle which enables the discrimination of lighter and heavier particles. After the radiator region the particle in the TRD enters a drift region which is filled with a xenon-based gas mixture. The radiated photon from the transition of the radiator is

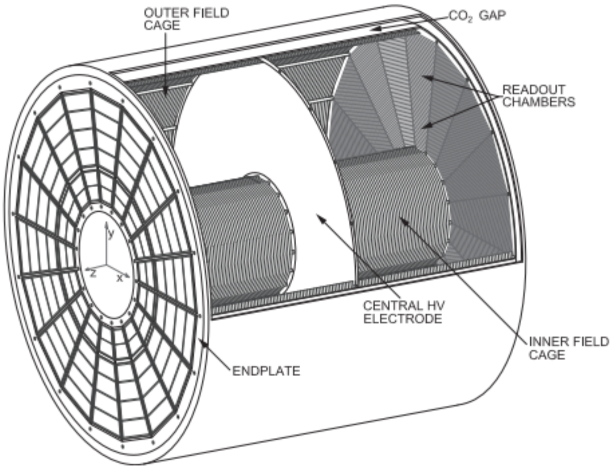

Figure 3.2.: Sketch of the ALICE Time Projection Chamber. Figure taken from [63].

absorbed at the beginning, while the particle travels through the drift region where ionization takes place. Multiwire proportional chambers are used for the readout in the TRD similar as in the TPC. The measured signal is used for tracking and can be matched with the reconstructed tracks in the ITS and TPC. The signal from the absorbed transition radiation photon appears later and is used for the discrimination of electrons/positrons and heavier particles as pions.

3.1.4. TOF

At a distance between 370 and 399 cm from the collision point, the Time Of Flight detector (TOF) follows as next sub-detector [59], depicted in orange in Figure 3.1. The TOF detector is used for the particle identification by measuring the time-of-flight of the particles with resolutions better than 50 ps [66]. Together with the track length, the velocity of the particle can be calculated which enables the determination of the mass of the particle if the momentum is known from tracking detectors. The TOF detector is composed of many Multigap Resistive Plate Chambers (MRPCs). They are made of resisitve plates with gaps filled with gas in between which is ionized by the passing charged particles. The resulting free electrons drift to the electrode where a high voltage is applied which in addition amplifies the signal.

3.1.5. EMCal

The electromagnetic calorimeter (EMCal) is installed next to the TOF detector, shown in grey in figure 3.1. The EMCal is used for the measurement of high p_{T} jets and for the identification of neutral particles as photons and π^0 but also electrons [67]. The acceptance in azimuth is limited to $80 < \phi < 187$ and $|\eta| < 0.7$ due to constraints caused by other detectors as the Photon Spectrometer (PHOS) in the opposite ϕ direction [68]. A sketch of the EMCal is depicted in figure 3.3 where the different super modules are shown. They are divided into 3072 modules where each represents a separate detector unit. Their working principle is based on a Pb-scintillator sampling calorimeter. 76 layers of lead and 77 scintillating layers are installed alternately. The incoming particles shower in the lead absorber and the resulting electrons and photons are measured with the scintillators in between. Up to $p_T = 30$ GeV/c a distinction between γ and π^0 is possible [67].

Concerning jet measurements the EMCal enables the reconstruction of full jets with charged and neutral particles. In addition measurements of γ-jet correlations can be performed with the EMCal. The dominant process for γ-jet production is the QCD Compton process $qg \rightarrow q\gamma$ [5]. The quarks and photons are produced back-to-back. These processes are of particular interest because the photon has no color charge and do not interact with the QGP. The measured photon energy thus corresponds to the full jet energy at the production and provides a clean probe for the jet measurement.

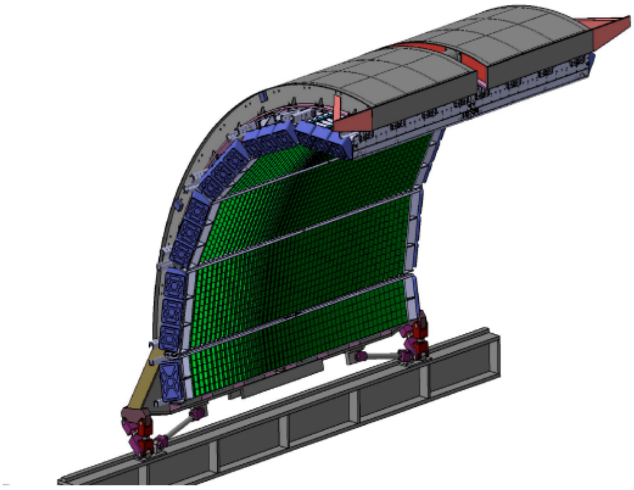

Figure 3.3.: Sketch of the ALICE EMCal. Figure taken from [68].

3.1.6. V0

The V0 detector system shown in grey in figure 3.1 (labeled with 2) is a forward detector, where V0A and V0C are mounted at opposite z-directions [69]. The acceptance is $2.8 < \eta < 5.1$ for V0A and $-3.7 < \eta < -1.7$ for V0C. They consist of plastic scintillators and are mainly used for triggering, the identification of background events as well as the measurement of the luminosity. In addition it is used for the measurement of the multiplicity and azimuthal distribution which can be used to determine the reaction plane.

3.2. Upgrades of the ALICE detector for Run 3

During the shutdown of the LHC between 2018 and 2021 several upgrades of the ALICE detector were installed for Run 3. In Run 3 Pb+Pb collisions will be performed with increased interaction rates from 1 kHz to 50 kHz at the LHC. This high interaction rate requires a continuous read out which is realised in the ALICE upgrade. A new ITS detector was installed which can deal with interaction rates up to 100 kHz for Pb+Pb collisions in comparison to the previous ITS where the limit is reached at 1 kHz. In addition the impact parameter resolution for secondary vertices is improved by a factor 3 [70]. For this, a new ITS with seven layers of silicon detectors based on Monolithic Active Pixel Sensors (MAPS) was installed. The material budget could be reduced by a factor 7 [70].

The readout in the TPC with the multiwire proportional chambers caused dead times of 280 μs which significantly limited the measured interaction rate [63]. In order to achieve continuous read out new Gas Electron Multiplier (GEM) foils were installed in the TPC. GEMs consist of thin insulating foils. The electron avalanche is triggered by high voltages produced inside small holes in the GEM foils instead of the wires in the multiwire proportional chambers.

Several other upgrades of the readout in other detectors were installed [59]. In addition a new software, O^2, was developed to handle the huge amount of produced data in the continuous read out. The main challenge of the large interaction rate will be a huge track density and overlapping events which complicate the track reconstruction.

3.3. Tracking

In this section the track reconstruction is briefly introduced. Tracking is challenging in heavy-ion collisions due to the huge amount of particles which are produced in one event. The produced particles stream to the detectors where they interact and lose energy. From these measured signals within the different detectors, the tracks have to be reconstructed and the particles identified.

A crossing particle produces signals in different cells of the detectors. Groups of adjacent detector cells, where a signal is measured, are called clusters [71]. The clusters are characterized by their signal strength, the amplitude and time, their positions and shapes. They are identified within every detector and are used as input for the track reconstruction [59]. However, the identification of the clusters might be difficult due to the overlapping of clusters from different tracks [72].

The full track reconstruction is performed by using a Kalman filter approach [59]. Kalman filtering is a general approach developed to estimate the best approximation of an unknown variable [73]. By using some prior approximation, the estimation is updated in several steps by using a weighted average at each step, between the current measurement and the prediction. The updated estimation goes into the algorithm as new prior. A detailed description of the Kalman filter is given in [73].

As a first step for the tracking the primary interaction vertex is identified within the SPD by searching for pairs of clusters pointing to the same interaction vertex [59]. Overlapping pileup events can be identified as their particles point to a different interaction vertex. Pileup events are discussed in more detail in 4.3.

After that a track seed is searched in the outer radius of the TPC where less clusters per volume element are measured. The seed is identified by searching two TPC clusters and by using the vertex which was found in the SPD. In a first step additional clusters are added from the outer to the inner radius of the TPC by using the Kalman filtering method. In addition ITS clusters are identified until the primary vertex is reached. After that the procedure is repeated in the outward direction to update the tracks. If possible clusters from the TRD and TOF detectors are added. In a final step a refit is done in the inward direction where the best track parameters are estimated.

There are several advantages of the Kalman filter approach as the simultaneous track identification and fitting, the rejection of incorrect clusters and the extension of the tracks between the different detectors [72]. Disadvantages of the Kalman filter approach are the dependence on the initially determined clusters and seeds. A detailed description of the tracking procedure is given in [72] and [59].

In the next section the data set which is used for the jet analysis and in particular the applied track selection and cuts are described.

4. Data set and track selection

For the jet analysis the 2018 Pb+Pb data set is used which was recorded at a center of mass energy of $\sqrt{s_{\mathrm{NN}}} = 5.02$ TeV and a centrality of 0-10% with the ALICE detector at the LHC. The first 90 out of 136 runs of the LHC18q run list with central barrel tracking are used. While the years of data taking at the LHC with specific sets of detectors are called Run 1 (2009-2013) and Run 2 (2015-2018), the periods are subdivided further. The run list LHC18q refers to a specific data taking period of about three weeks with a magnetic field of $B = 0.5$ T and an interaction rate of 7.5 kHz. This setup is not changed during the runs of one run list, where one single run from the list is a period of several hours of data taking.

The used data set includes about 35 million events after all cuts are applied. In the following sections the data preparation as well as the track and event selections are described. All information about the data structure or the so called hybrid track cuts are taken from internal ALICE pages and [71].

4.1. Data preparation

The first step is the production of TTrees where the data from AOD files (Analysis Object Data) is used as input. The AODs are products from the ESD files (Event Summary Data) which in turn are produced from raw data. They contain the full event information while for the AODs a subset of information was selected.

A TTree is a ROOT object which was developed for the storage of huge amounts of data, as millions of events with several thousands of tracks [74]. The advantages are reduced storage space, faster access to the saved objects and the possible hierarchical data structure.

The TTree described in the following was developed within the scope of this thesis in particular for the jet analysis. In order to produce the TTrees all relevant information about the events and tracks from the AODs are stored. In particular the AODs and not the ESDs are used because a variable associated to the track length was only available for AODs. The variables of the tracks which are kept, are listed in table 4.1 together with some applied pre-selection.

As a charged particle jet reconstruction will be carried out, most of the information are related to the ITS and TPC. In addition, information from the EMCal is stored which could be used to perform a jet reconstruction including neutral particles or γ-jet measurements. The DCA (distance of closest approach) to the primary vertex in x-y and z-direction, the TPC χ^2 and dE/dx as well as the number of TPC cluster, the TOF signal, the track length and the particle momentum $(p_{\mathrm{x}}, p_{\mathrm{y}}, p_{\mathrm{z}})$ are stored. For the jet reconstruction only the momenta of the particles are necessary. However, some additional information is kept in order to perform a track and event selection.

In addition a particle identification could be done later. The variables and the cuts which are applied will be explained in more detail later.

An additional status variable is used where the different bits are set from 0 to 1 for a hit in the different ITS layers (bits 0-5), the ITS refit (bit 6) and the different filter bits 32, 64, 128, 256 and 512 (bits 7-11). The status variable is later used to check the properties of the tracks mentioned above. The different filter bits are sets of cuts which can be applied to the AODs for the track selection. For example filter bit 128 contains only TPC track cuts. Further investigations are carried out for the hybrid track cuts, which are a combination of filter bit 256 and 512, as described in section 4.2.

Table 4.1.: Overview of the variables stored in the TTrees with the applied preselection.

Variable	**Selection**
|DCA x-y & z|	< 1 cm
η	< 1
TPC refit	true
Number of TPC cluster	> 50
TPC χ^2 / cluster	< 8
TPC dE/dx	-
TOF signal	-
track length	-
$p_\mathrm{x}, p_\mathrm{y}, p_\mathrm{z}$	-
Hits in ITS layer 0-5	-
ITS refit	-
Filter bits 32, 64, 128, 256, 512	-

In addition, different event information is stored in the TTrees. The x-, y- and z-vertex positions of the events are kept. In addition, the number of TOF hits, TRD tracklets and V0 hits are saved. They will be used later for the identification of pileup events. This is explained in more detail in section 4.3. In addition, the run IDs of the events are saved to be able to assigned the events in time later.

To reduce the file size of the TTrees, an internal conversion of the variables into data types with smaller size are introduced. The six float values (DCA x-y and z, TPC χ^2, TPC dE/dx, TOF signal, track length) are converted into six short variables. This reduces the size of the variables from 6×32 bits to 6×16 bits [75]. The conversion is done by multiplying the floats with a factor depending on the needed resolution, for example 100 to keep two decimal places. If the functions to get the stored variables are called the values are internally converted back into floats by dividing the shorts with the same factor. It turns out that for the particle momentum a resolution of 5 MeV/c, which is the maximum reached with the short variables, is not enough. Instead of three shorts finally one ULong64 (64 bit) is used and all three momentum values ($p_\mathrm{x}, p_\mathrm{y}, p_\mathrm{z}$) are saved in this one variable by setting every bit separately. In the first 21 bits p_x is stored, p_y follows in bits 21-41 and p_z in bits 42-62. For each value the first bit is used for the sign and the remaining 20 bits for the value itself. A resolution of 167 keV/c is obtained and 1/3 of the storage space can be saved compared to three float values which would need 96 bits.

The size of one TTree is reduced from about 700 to 400 MB by the conversion described above. Producing the TTrees and doing the internal conversion of the data types results in very compact objects which can be easily used for the jet analysis. In the next section the track cuts are described which will be used for the analysis.

4.2. Track selection

Cuts are applied to the reconstructed tracks in order to obtain a clean data set depending on the particular analysis.

In this section different sets of cuts for the event and track selection are compared. In particular for the tracks the hybrid track cuts are compared to a basic selection of cuts without any filter bits. Different properties as the multiplicity of the event or the $\eta - \phi$ distribution of the tracks are studied. All information about the hybrid track cuts are taken from internal ALICE pages.

Table 4.2.: Overview of the different hybrid track cuts and the individual selection of basic cuts.

Basic selection	**Hybrid track cuts (filter bit 256+512)**
$\lvert$DCA xy & z$\rvert < 0.5$ cm	SetMinNCrossedRowsTPC(70)
$\lvert\eta\rvert < 0.9$	SetMinRatioCrossedRowsOverFindableClustersTPC(0.8)
TPC refit = true	SetMaxChi2PerClusterTPC(4)
TPC cluster > 50	SetAcceptKinkDaughters(kFALSE)
TPC $\chi^2 < 300$	SetRequireTPCRefit(kTRUE)
$p_{\mathrm{T}} > 150$ MeV	SetRequireITSRefit(kTRUE)
	SetClusterRequirementITS(kSPD, kAny)
	SetRequireSigmaToVertex(kFALSE)
	SetMaxChi2PerClusterITS(36)
	SetMaxChi2TPCConstrainedGlobal(36)
	SetMaxDCAToVertexXY(2.4)
	SetMaxDCAToVertexZ(3.2)
	SetMaxFractionSharedTPCClusters(0.4)
	(only for filter bit 512)
	SetClusterRequirementITS(kSPD, kOff)

For the jet measurement charged particles which are reconstructed with the ITS and TPC are used. A basic set of quality cuts is listed in the first column of table 4.2.

The DCA (distance of closest approach), which describes the impact parameter of the track to the primary vertex, in x-y and z-direction is required to be smaller than 0.5 cm. This cut is applied to reject secondary particles which are produced for example in interaction processes of primary particles with the detector material or in the decay of V^0 particles like $\Lambda \rightarrow p + \pi$. For the jet measurement only primary particles which are produced in the collision should be included. By cutting on the DCA the rate of secondary particles can be reduced.

In addition a cut on the detector acceptance is applied. As TPC reconstructed particles are used for the analysis a cut on $|\eta| < 0.9$ is used which corresponds to the TPC acceptance for full tracks. As described in section 3.3, one TPC cluster is a group of adjacent detector cells which are firing at the same time if a signal is detected. The number of TPC clusters is required to be larger than 50 in order to reject short tracks. In addition the TPC refit is requested and at least the TPC χ^2 has to be smaller than 300. These requirements are used to reduce the noise and to obtain only good quality tracks.

Only tracks with $p_{\mathrm{T}} > 150$ MeV/c are accepted because smaller momenta can not be measured reliably. In addition a cut on the z-vertex of the events of 8 cm is applied, which will be explained in the following. It should be pointed out that in the basic selection of cuts no requirements for the ITS are used.

The hybrid track cuts are a combination of filter bit 256 and 512. The functions which are connected to the different cuts and the used requirements are listed in the second column of table 4.2. The TPC related cuts are a minimum number of 70 for the crossed rows, which are the number of clusters used for the fit. They should be at least 80 % of the number of crossed pad rows (findable clusters) and the χ^2/cluster should not be larger than 4. In addition the charged daughter particles, which are decay products from charged particles (kinks) which decay into one charged and one neutral daughter particle, are not accepted. The TPC and ITS refit is requested. For the filter bit 256 all tracks with hits in any of the two SPD layers are accepted while the filter bit 512 requires all tracks without hits in the first or second layer of the ITS. Those complementary tracks were introduced to compensate missing tracks due to a hole in the SPD. This is shown in the ϕ distribution in figure 4.5 which is discussed later.

A maximum χ^2 / cluster is set to 36 for the ITS. For the rejection of bad quality primary tracks, the χ^2 between TPC and global tracks is constrained to 36. Values of 2.4 cm and 3.2 cm are used as cuts for the DCA to the primary vertex in x-y and z-direction and the maximum fraction of shared TPC clusters is set to 40%. In addition to the filter bits 256 and 512 the basic cuts described above are applied, in particular only tracks with $p_{\mathrm{T}} > 150$ MeV are used for the hybrid track selection and the DCA in x-y and z-direction is further constrained to 0.5 cm.

For the comparison of the different sets of cuts, the multiplicities of the events are considered. The upper plot in figure 4.1 shows the multiplicity distribution for the hybrid tracks on the x-axis and for the basic selection on the y-axis without any additional requirements on the events. The tail in the particle multiplicity distribution of the hybrid tracks at low multiplicity arises due to the small size of the ITS. The hybrid tracks require a hit in the first or second layer of the ITS, the SPD. The first layer of the SPD has an inner radius of 3.9 cm and the η acceptance is $\eta < 1.98$ ($\theta = 15.72$ deg.) [70]. This corresponds to an extension of 13.85 cm in the positive and negative z-direction. If the z-vertex of the event is slightly moved to the positive or negative side, not all particles can be detected by the first layer of the ITS anymore which results in the low multiplicity tail.

This effect is also observed in figure 4.2. Here the z-vertex is shown on the x-axis

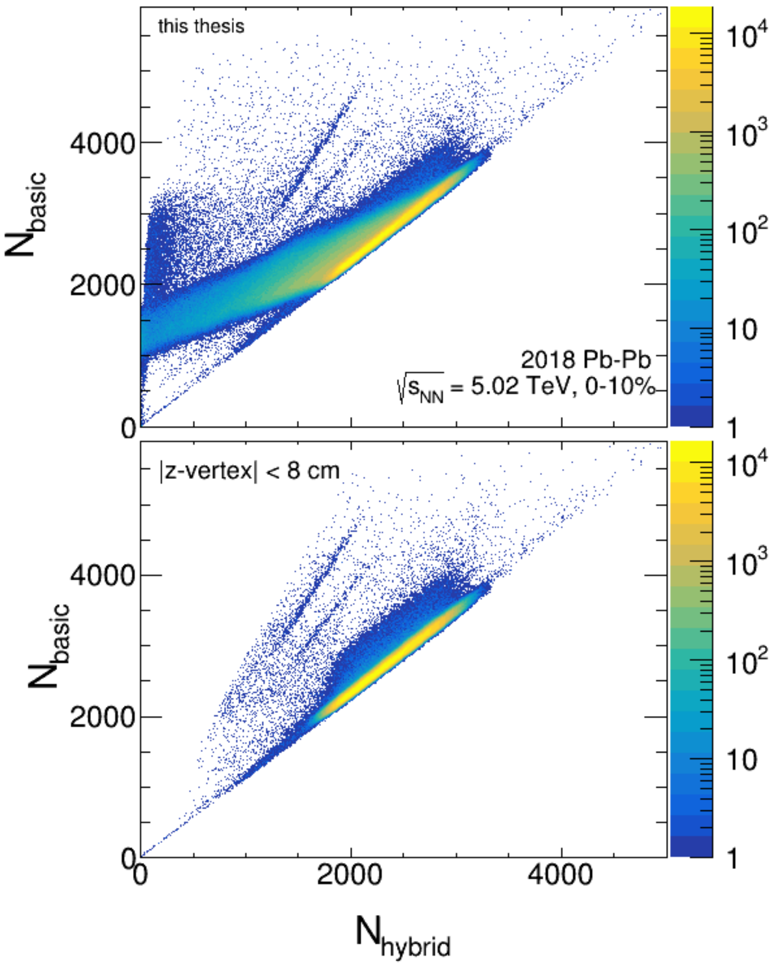

Figure 4.1.: Multiplicity distribution of hybrid tracks N_{hybrid} on the x-axis and tracks which passes the basic selection N_{basic} on the y-axis. Without a z-vertex cut (upper) and with |z-vertex| < 8 cm (lower).

and the number of particles which have at least three hits in the ITS on the y-axis. The wings on the left and right side at z-vertex distances above 8 cm (indicated by the red dashed lines) are a result of the small acceptance of the ITS as described above. The tail at low multiplicities disappears if a cut on the z-vertex is applied. This is shown in the lower plot of figure 4.1 where only events with |z-vertex| < 8 cm are used. For the following analysis this cut on the z-vertex of 8 cm is applied. The additional cuts in the hybrid tracks, for example the requirements on the ITS, clean the track distribution even more.

The two corresponding multiplicity distributions for the hybrid track cuts (red) and the basic selection (black) are shown in figure 4.3. A shift of about 200 is visible between the two distributions and in addition the distribution of the multiplicity becomes narrower if the hybrid track cuts are applied.

For further investigations of the behavior of the ITS, the $\eta - \phi$ distribution of the tracks are studied. In order to do this, only the tracks which passes the basic selection and the additional requirement that there are at least 3 hits in the ITS in

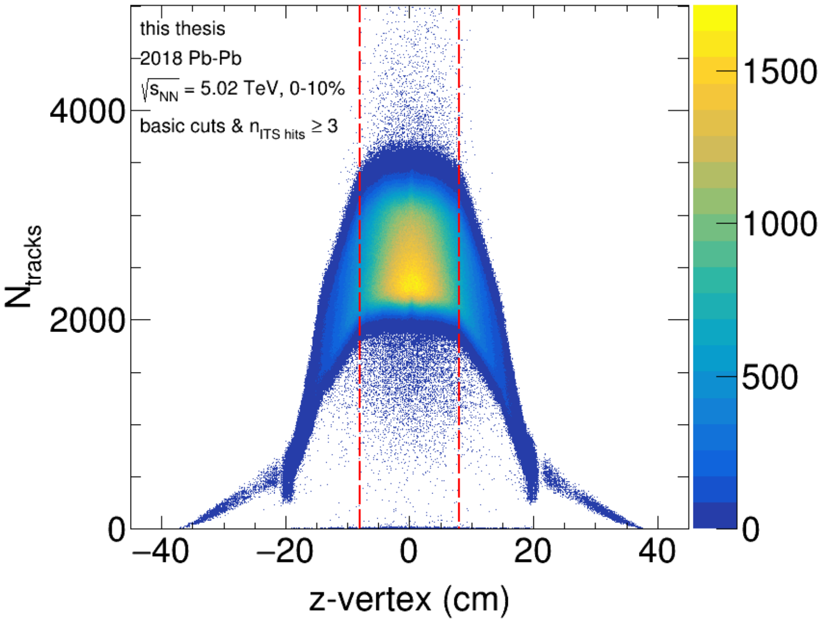

Figure 4.2.: Multiplicity distribution in dependence of the z-vertex position of the event. N_{tracks} are all tracks which passed the basic track selection and the requirement of at least three hits in the ITS. The red lines indicate the cuts at ±8 cm which are applied to the z-vertex.

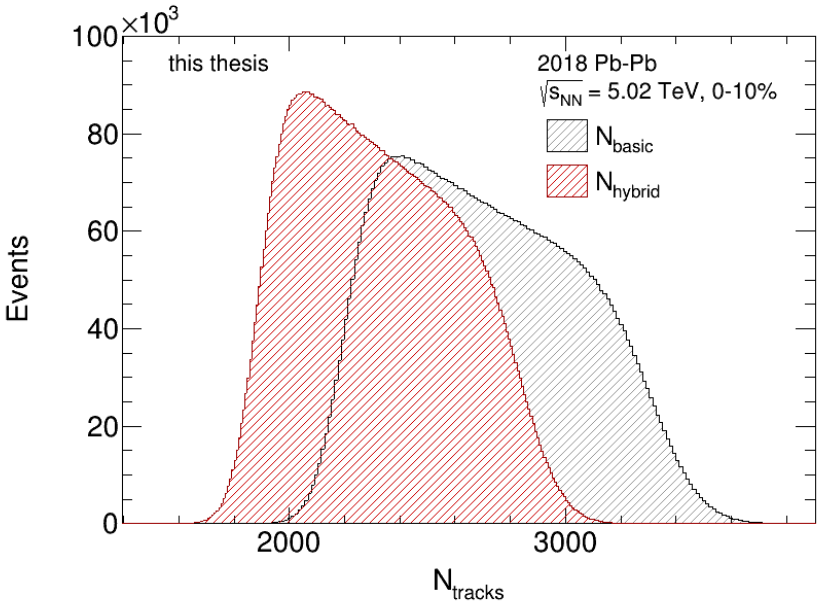

Figure 4.3.: Multiplicity distributions with the basic track selection (black) and hybrid track cuts (red). Only events with |z-vertex| < 8 cm are used.

any of the six layers are used. In addition always one of the six layers of the ITS is excluded. The resulting distributions are inefficiency plots of the layer which is required to be without a hit. In the left panel of figure 4.4 layer 0 of the ITS is excluded. The yellow region around $\phi = 130°$ is an inefficient region of this layer. The same is observed for layer 1 which is shown in the right panel of figure 4.4. In the case of perfect layers, there would be no entry in any of those distributions because every layer would have a hit for every particle. Due to the inefficient region around $\phi = 130°$ the hybrid tracks will be used in the following for the analysis because complementary tracks were added to compensate the missing tracks. This is studied in the following ϕ distribution.

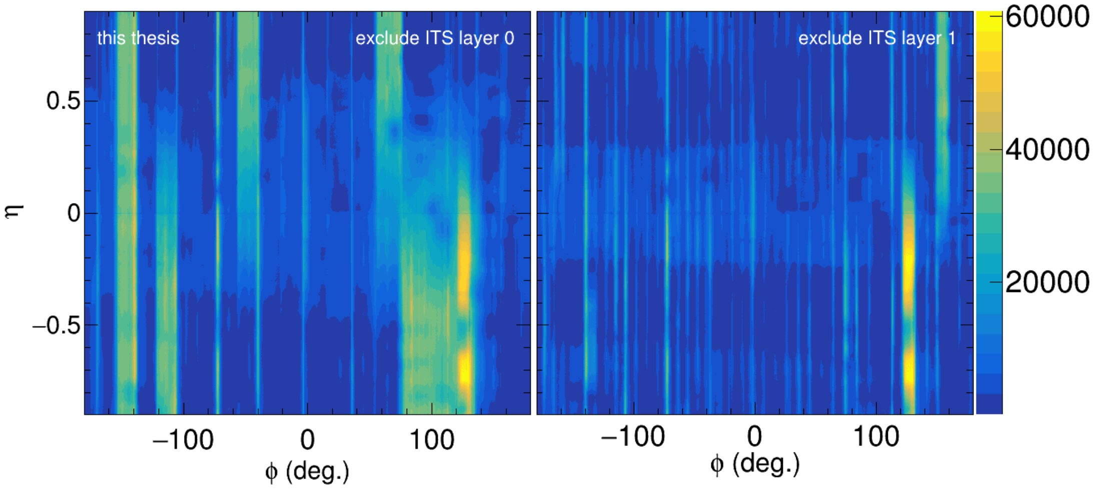

Figure 4.4.: η-ϕ distribution of tracks which passed the basic cuts and have at least three hits in the ITS. The three hits are not restricted to specific layers. Layer 0 (left) or layer 1 (right) is excluded. In addition only events with $|\text{z-vertex}| < 2$ cm are used.

Figure 4.5 shows the ϕ distributions for the different sets of cuts. The distribution for the basic cuts is shown in black and the hybrid tracks in blue. In addition the two different filter bits which corresponds to the hybrid track cuts are used separately. The gap which is observed between $\phi = 120°$ and $\phi = 140°$ for the tracks which passes filter bit 256 (red) is filled by the complementary tracks of filter bit 512 (green). This results in the relatively flat distribution of the hybrid tracks (blue). The same effect of the missing particles around $\phi = 130°$ is shown above in figure 4.4, where an excess of tracks was observed in this region if layer 0 or 1 of the ITS are excluded. The peak around $\phi = 130°$ for the basic selection might be a result of some double counting of the tracks. A rejection of about 15% of the tracks by applying the hybrid tracks cuts is observed.

As an additional check, three different runs were used for the investigations described above where no significant differences between the runs were found regarding the multiplicity or other parameters.

In the following analysis the hybrid track cuts are used. Because no selection of cuts were done before the production of the TTrees, it is possible to easily change the applied cuts for the jet analysis. In addition, only tracks with $p_{\mathrm{T}} > 150$ MeV/c

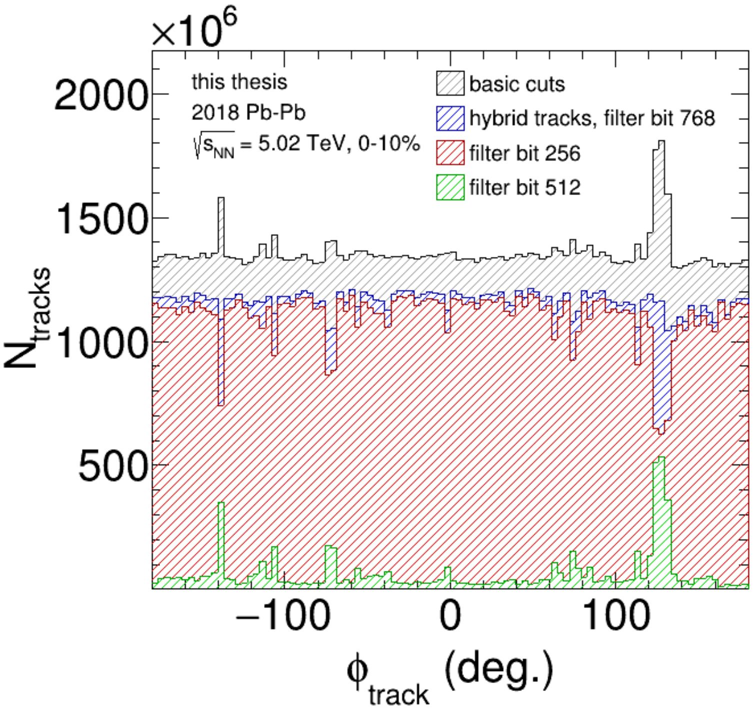

Figure 4.5.: ϕ distribution of the tracks which fulfill the basic selection (black), the hybrid track cuts (blue), filter bit 256 (red) and filter bit 512 (green).

are used as well as tracks with $|\eta| < 0.9$ and $|\text{DCA xy \& z}| < 0.5$ cm. For the event selection the requirement of $|\text{z-vertex}| < 8$ cm is used. Unless otherwise stated all studies in section 5 and 6 are done with this selection of events and tracks. In the next section the cuts which are applied to reject pileup events are presented.

4.3. Pileup rejection

In this section, the rejection of pileup events is presented which turned out to be necessary at a later stage of the analysis. Therefore the studies presented in this section are done with the data set used for the production of the mixed events, where cuts on the edges of the multiplicity distribution were applied. This is explained in more detail in section 5.3. All other cuts are the same as described above.

The collision of two lead nuclei is described by one event. The produced particles of an event stream to the detectors where they are measured. During the readout time of the detectors it is possible that one or more additional events take place which are overlapping with the first event. The additional collisions are called pileup events. The produced particles from pileup events are possibly assigned to the first collision which leads to a mixture of the events.

One distinguishes same-bunch-crossing pileup events and out-of-bunch pileup [71]. In the first case two or more events take place in the same bunch crossing. The collision points are separated in beam direction but they happen very close in time. Lots of those pileup events are rejected by identifying the tracks which point to the different interaction vertices. However, if two or more collisions take place very close to each other with a very small vertex separation, they can not be distinguished which leads to an increase in the multiplicity. Out of bunch pileup events are from collisions of different bunch crossings. They are separated in time which leads to a spatial shift between the measured tracks as they are produced at different times. Depending on the readout time the detectors are differently affected by the pileup events.

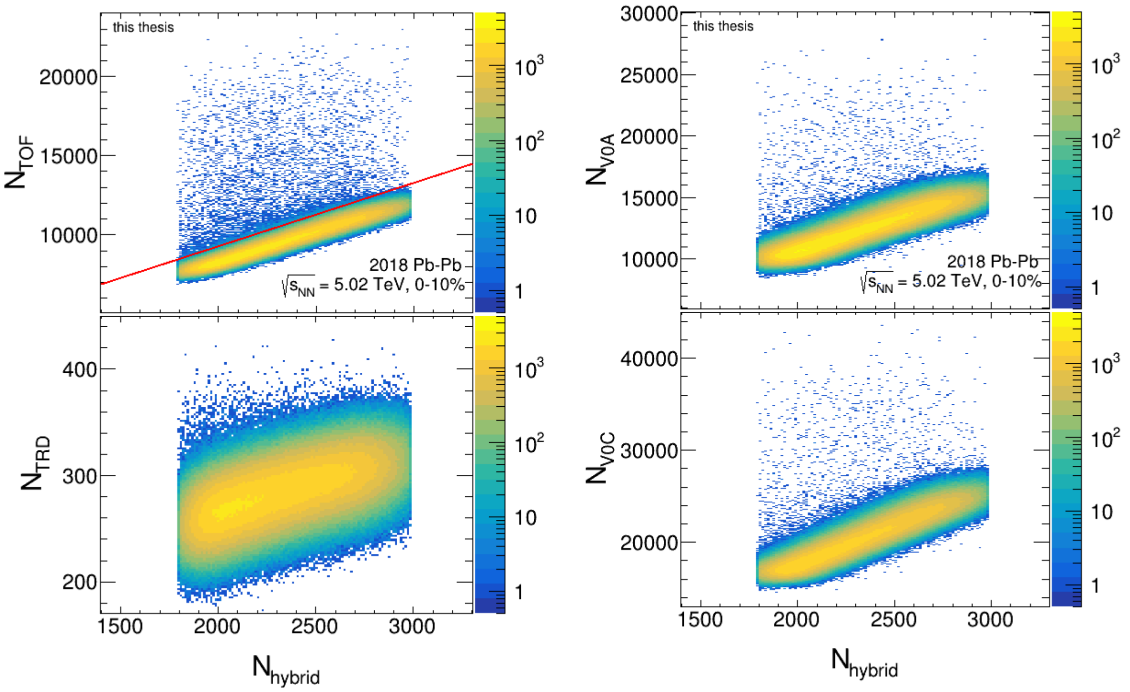

Figure 4.6.: Number of TOF hits (upper left panel), online TRD tracklets (lower left panel), V0A (upper right panel) and V0C (lower right panel) hits in dependence of the charged particle multiplicity for the hybrid track cuts N_{hybrid}. All events above the red line are rejected to reduce the contribution of pileup events.

Remaining pileup events can be identified by comparing the number of TOF hits, TRD tracklets or V0 hits with the TPC reconstructed track multiplicity. Due to the faster readout time of the TOF (0.5 μs) and TRD (1 μs) detector in comparison to the TPC (100 μs), particles from pileup events can be identified by comparing the multiplicities measured in the different detectors. In figure 4.6 the number of TOF hits (upper left), online TRD tracklets (lower left), the V0A (upper right) and V0C (lower right) hits in dependence of the multiplicity are shown. The charged particle multiplicity N_{hybrid} is the number of tracks which passes the hybrid track selection which are based on ITS and TPC reconstructed tracks. In the upper left panel the correlation between the TOF hits and the multiplicity is visible. In addition some events have a large number of TOF hits while the hybrid track multiplicity stays the same. These events are same bunch crossing pileup events. Due to a shift between the vertices larger than the applied DCA cut of 0.5 cm, the tracks from the pileup events are not or only partly within the hybrid tracks detected with the TPC. For distances smaller than the DCA cut, no distinction between the events would be possible. The pileup events are observed on the right side too, where the V0A and V0C signal is shown in dependence of the hybrid track multiplicity. The pileup is visible for the TOF and V0 detectors as no restriction on the DCA of the tracks to the primary vertex are applied for the particles measured in these detectors.

A small increase of the online TRD tracklets at lower multiplicities N_{hybrid} is observed too in figure 4.6 (lower left). However, for the online TRD tracklets a connection to the vertex is required and thus the tracks from pileup are not completely visible.

Further investigations on pileup could be done by varying the DCA cut and studying the behavior of the multiplicity.

In order to reject the pileup events, a two-dimensional cut is applied. As indicated in the upper left panel all events with TOF hits above the red line are rejected. The results of this cut are shown in figure 4.7. All events from pileup which lead to an increase of the TOF multiplicity are rejected. In addition most of the V0A and V0C entries of pileup events are discarded by the cut on the TOF multiplicity. For the online TRD tracklets the effect of the cut is smaller due to reasons described above. As there are still some pileup events in the TRD, V0A and V0C distributions additional cuts are applied, as indicated by the red lines, in order to reject the remaining pileup.

All additional cuts as described above to reject pileup events are applied for the results presented in section 7. For the systematic studies as presented in 6 they are not applied unless otherwise stated.

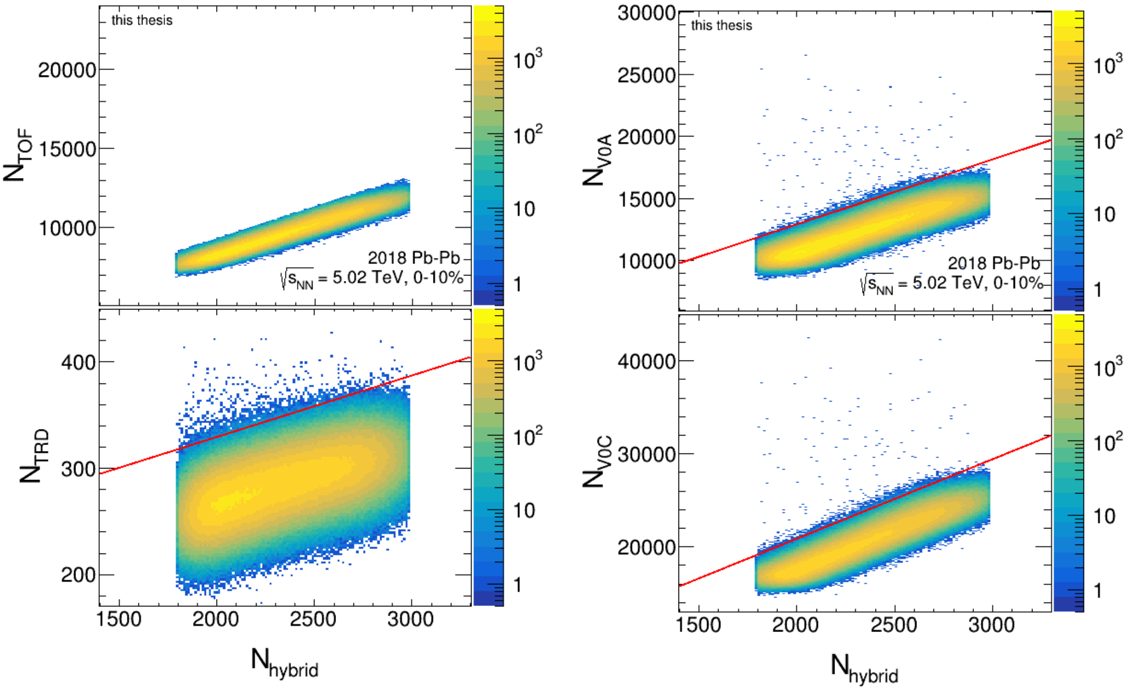

Figure 4.7.: Number of TOF hits (upper left panel), online TRD tracklets (lower left panel), V0A (upper right panel) and V0C (lower right panel) hits in dependence of the charged particle multiplicity for the hybrid track cuts N_{hybrid} after the cut on the TOF hits as shown in figure 4.6 was applied. In addition all events above the red lines will be rejected to reduce the remaining contribution of pileup events.

5. Analysis strategy

In this chapter the analysis strategy for the jet measurement in heavy-ion collisions at ALICE is presented. The focus is on the production of the mixed events which will be used for the description of the uncorrelated background in the jet measurement. In the first section the general setup for the jet reconstruction is described 5.1 followed by the event plane reconstruction 5.2 which is necessary for the further proceedings.

After that the main idea of the analysis follows by the introduction of the mixed events. The mixed events will be used as a new approach for the estimation of the uncorrelated background as a solution to carry out jet measurements down to low p_{T} as presented in [45]. It enables jet measurements without high p_{T} cuts on the reconstructed objects. In section 5.3 the general production of the mixed events is described. The used strategies to obtain a mixed event which gives a reasonable description of the uncorrelated background in the real data are presented in 5.3.1. Different modifications and systematic studies of the mixed event are shown in the next section 6.

5.1. Jet reconstruction setup

In this section the setup which is applied for the reconstruction of the jets, is described. The FastJet software package [44] as introduced in section 2.3.1 is used for the analysis. A charged particle jet reconstruction is carried out where the anti-k_{T} algorithm is used for the jet reconstruction and the k_{T} algorithm for the estimation of the background. This is described later in more detail. The distance measures of the two algorithms are given in equation2.8 and 2.9. As input for the clustering a PseudoJet vector, which in principle is a Lorentz vector, is used. The momentum components of the particles (p_{x}, p_{y}, p_{z}) and their energy is used. The energy is calculated with the mass of the pions [76] because they represent the largest fraction of produced particles. However, this results in a systematic uncertainty. To avoid this, a particle identification (PID) should be performed which is possible at ALICE. In particular the relevant information for the PID are already stored in the TTrees. The particles or fractions of jets before the full jet is found are called PseudoJet objects in the FastJet package [44]. All particles which passes the selections described in chapter 4.2 are used for the jet reconstruction.

The jet radius R is given in equation 5.1 and is set to $R = 0.3$ as default value of intermediate size [10].

$$R = \sqrt{(\Delta\phi)^2 + (\Delta\eta)^2} \tag{5.1}$$

It is calculated from the extension in ϕ and η direction. However, in the FastJet package the rapidity y is used, as described in section 2.3.1, and thus the PID as described above would be necessary. In the following the unit of the jet radius is set to one. Different variations of the jet radius are presented in section 7.2.1.

For the clustering the standard recombination scheme ($E-scheme$) is used where the 4-vectors of the particles are added. To guarantee that the whole jet is within the detector acceptance a fiducial cut is used in the analysis. Only jets which are within $|\eta| < 0.9 - R$ are accepted and all jets which are (partly) outside this region are rejected. For the area estimation an active area is used, where ghost particles with a ghost particle area of 0.01 are distributed over the acceptance, as described in section 2.3.1. Although the jet area has the unit sr, it is set to one in the following.

In addition, any object which is reconstructed with the anti-k_{T} algorithm is called a "jet", although lots of the reconstructed objects are only combinatorial background and no true jets.

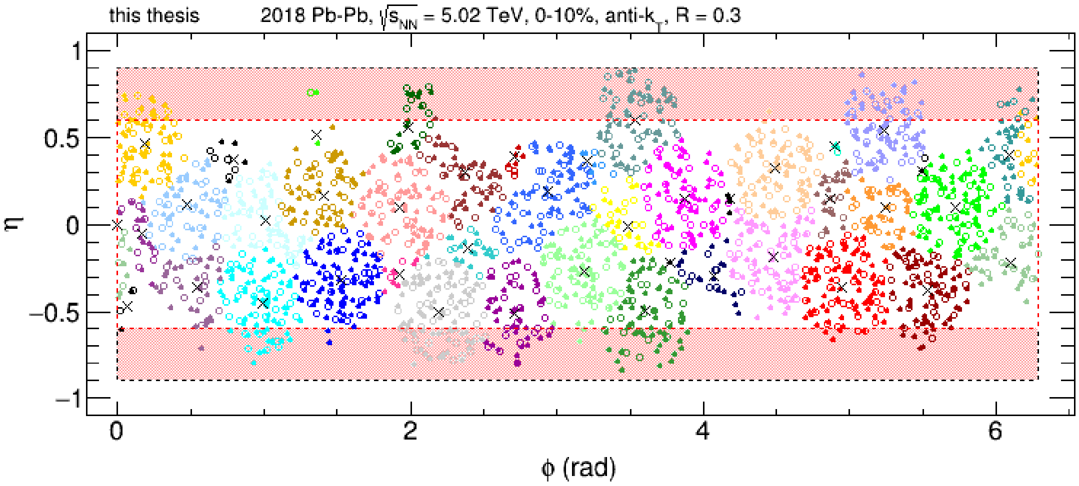

Figure 5.1.: Event display of reconstructed charged jets in η-ϕ. One event of the 2018 Pb+Pb data set at $\sqrt{s_{\mathrm{NN}}} = 5.02$ TeV with 0-10% centrality was used. The jets are reconstructed with the anti-k_{T} algorithm with $R = 0.3$. The tracks are shown with filled circles and the ghost particles with open circles. Tracks and ghost particles of one jet are represented by the same color. The "x" indicates the centroid of the reconstructed jet. The acceptance of $|\eta| < 0.9$ is shown and in addition the fiducial cut at $|\eta| < 0.6$ is represented by the red shaded region.

In figure 5.1 an event display of the reconstructed jets within one event of the 2018 Pb+Pb data set at $\sqrt{s_{\mathrm{NN}}} = 5.02$ TeV with 0-10% centrality is shown. For the reconstruction the anti-k_{T} algorithm with $R = 0.3$ is used. The reconstructed jets are shown in the η-ϕ plane. The constituents of each jet are depicted in a different color, where the filled circles are the charged tracks and the open circles are the ghost particles. The centroid of each jet is represented by the "x". The full acceptance in η and ϕ is shown and in addition the applied fiducial cut is represented by the red shaded region.

In total 41 jet candidates are reconstructed in the event shown in figure 5.1. However, lots of the reconstructed objects have a small area and jet p_{T} and are expected to be combinatorial background. In order to reject these objects, which contain only few particles an area cut is applied. For the jet radius of $R = 0.3$ only jets with areas larger than 0.2 are accepted. The area distribution will be shown in section 6.3. With the described setup for the jet finding on average 40 objects are reconstructed within one event. Roughly one half of these objects are discarded after the area cut was applied but there are still large contributions from uncorrelated background.

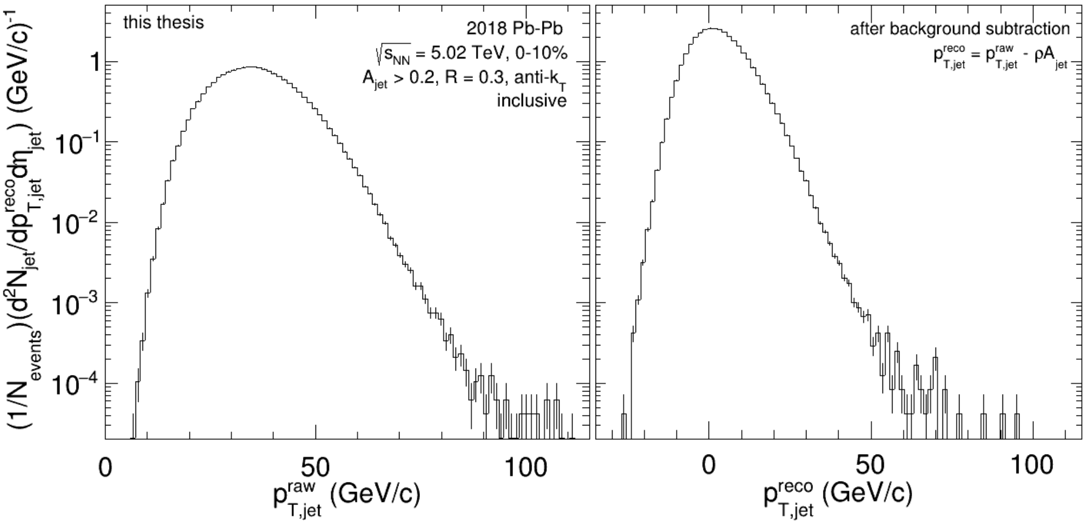

Figure 5.2.: Reconstructed jet distribution of a subset of 10% of the full data set. The anti-k_{T} algorithm was used with $R = 0.3$ and the setup described above. In the left panel the raw jet $p^{\mathrm{raw}}_{\mathrm{T,jet}}$ is shown. In the right panel the reconstructed jet $p^{\mathrm{reco}}_{\mathrm{T,jet}}$ is shown where the event-to-event background energy density ρ times A_{jet} was subtracted. Both distributions are normalized by the number of used event N_{events}.

A resulting raw jet distribution for a subset of the full data set is shown in the left panel of figure 5.2. The jet reconstruction setup with $R = 0.3$ as described above was used. However, in the jet reconstruction lots of underlying particles which do not correspond to the real jet energy are used. This background can be reduced on an event-by-event basis.

For the calculation of the event-to-event background energy density ρ, given by equation 2.10, the k_{T} algorithm is used for the reconstruction with a radius of $R_{\mathrm{bckg}} = 0.3$. Some reconstructed jets with the largest energy are removed in the ρ estimation. As default value three jets are removed to carry out the background estimation without true jets. For the mixed events zero jets will be removed later, as no real jets are expected. Variations of these values are shown in 6.3.1. The event-to-event background energy density ρ is described in the following with the explicit unit of GeV/(c sr), following the convention used in [45].

The resulting jet distribution, where the event-to-event background energy density scaled with the jet area was subtracted, is shown in the right panel of figure 5.2. On the x-axis $p^{\mathrm{reco}}_{\mathrm{T,jet}}$ is shown which is given by equation 2.11. After the background subtraction the jet distribution gets narrower and has a maximum at $p^{\mathrm{reco}}_{\mathrm{T,jet}} = 0$

GeV/c. As expected, the jet distribution is broader due to the background fluctuations, before the subtraction of the event-to-event background energy density was done. In addition, entries at negative $p_{\mathrm{T,jet}}^{\mathrm{reco}}$ are observed after the subtraction of ρA_{jet}, which arise due to background fluctuations. Only an average value of the event-to-event background energy density is subtracted for each event. However, local fluctuations of this value lead to negative reconstructed jet energies. The fluctuations in the background energy density are described by δp_{T} given by equation 5.2. It is the difference between the reconstructed and the true jet p_{T}.

$$\delta p_{\mathrm{T}} = p_{\mathrm{T,jet}}^{\mathrm{reco}} - p_{\mathrm{T}}^{\mathrm{true}} \tag{5.2}$$

The fluctuations can be calculated by the embedding of true jets, for example generated with PYTHIA, into the real events. After the reconstruction the jets are matched to the true jets. The difference between the reconstructed jets with the embedded true jet and the true jet energy results in δp_{T}. The embedding procedure is described in more detail later in section 8.3, where the corrections of the raw jet distributions are discussed.

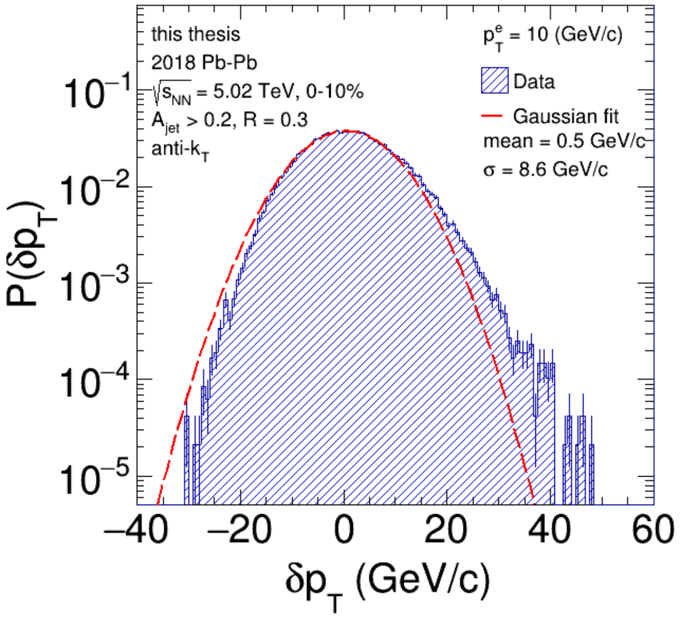

Figure 5.3.: Probability distribution of δp_{T} where one track with $p_{\mathrm{T}}^{\mathrm{e}} = 10$ GeV/c is embedded into the events.

An example of a resulting δp_{T} distribution is shown in figure 5.3. In this example only one track with $p_{\mathrm{T}} = 10$ GeV/c was embedded into the events, which represents $p_{\mathrm{T}}^{\mathrm{true}}$. After the jet reconstruction the track is located within the constituents of the jets in order to do the matching.

Only entries at $\delta p_{\mathrm{T}} = 0$ GeV/c would be visible if no fluctuations of ρ within the events exist. However, only an average value of the background energy density is estimated and subtracted from the raw jet p_{T}. Thus the resulting δp_{T} distribution has a finite width. In the extreme case fluctuations of almost ±40 GeV/c are observed. For comparison, the δp_{T} distribution is fitted with a Gaussian function, where a mean value of 0.5 GeV/c and a width of 8.6 GeV/c is obtained. The distribution is not exactly centered around $\delta p_{\mathrm{T}} = 0$ GeV/c, as more entries are observed at positive δp_{T}.

In the following the inclusive jet distribution, where no further cuts or constraints are used and all objects which are reconstructed with the setup described above are accepted, is studied. In addition the quasi-inclusive jet distribution is studied where a small bias is applied to the jets. The leading track of the jets is required to have a p_{T} above some certain threshold $p_{\mathrm{T}}^{\mathrm{min}}$. Different values of $p_{\mathrm{T}}^{\mathrm{min}}$ are used in order to find the p_{T} region where the small bias is negligible. The idea of quasi-inclusive distributions with a small bias in comparison to the concept of inclusive jet distributions is discussed in more detail in chapter 7. In addition to the inclusive jet distributions the h-jet distribution is studied, where a trigger hadron with $p_{\mathrm{T}} > p_{\mathrm{T}}^{\mathrm{trig}}$ is required and the recoiling jet distribution is used. This semi-inclusive distribution was already used in the jet analysis in [45] and will be described in more detail in section 7.3.

In the next section the event plane reconstruction is presented followed by the mixed events which are introduced as solution to reject the reconstructed objects of the large uncorrelated background. The procedure of the creation of the mixed events as well as several properties are presented.

5.2. Event Plane reconstruction

In this section the event plane reconstruction is described which is a necessary step for the production of the mixed events. In order to do the mixing of the events properly, only events with similar event plane angles are used for one mixed event. A detailed description of the mixed event production is described in the next section 5.3.

The event plane angle Ψ_2 is calculated following the description in [20] where equation 5.3 is proposed. The anisotropic flow as described in section 1.3 is used in this approach for the calculation of the event plane. For our estimation the elliptic flow is used and thus the second harmonic with $n = 2$.

$$\Psi_{\mathrm{n}} = \left(\tan^{-1} \frac{\sum_i w_{\mathrm{i}} \cos(n\phi_{\mathrm{i}})}{\sum_i w_{\mathrm{i}} \sin(n\phi_{\mathrm{i}})} \right) \Big/ n \tag{5.3}$$

In the calculation the transverse momentum of particle i is used for the weight w_{i} and ϕ_{i} is the azimuthal angle of the particle. Only particles with $p_{\mathrm{T}} < 3$ GeV/c are used for the event plane estimation in order to exclude high p_{T} particles from jets which would bias the calculation. In addition Ψ_2 is calculated for positive and negative pseudo-rapidity $0.1 < |\eta| < 0.9$ separately and merged afterwards.

The plots in figure 5.4 depict the calculated event plane angle for the full (red), positive (green) and negative (blue) pseudo-rapidity. In the left plot the uncorrected event plane distribution is depicted. Large differences between negative and positive Ψ_2 of 30% are visible and thus it is necessary to correct the event plane distribution,

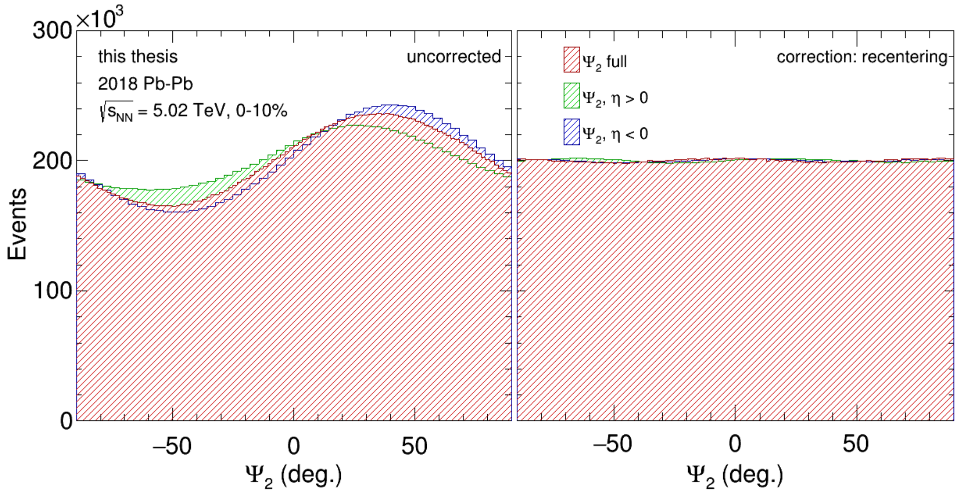

Figure 5.4.: Event plane angle Ψ_2 over the full acceptance (Ψ_2 full) and for positive (green) and negative (blue) η without corrections (left) and after recentering (right).

where different methods are possible. The correction is done because a flat distribution of the event plane angles are expected as no orientation of the event plane should be favoured. Instrumental effects as broken sections in the detector could be the reason for non-uniform distributions of the event plane angle.

The right plot in Figure 5.4 shows the event plane after the application of the recentering method as used in [19]. For this correction the Q-vector components $Q_\mathrm{x} = \sum_i w_\mathrm{i}\cos(2\phi_\mathrm{i})$ and $Q_\mathrm{y} = \sum_i w_\mathrm{i}\sin(2\phi_\mathrm{i})$ are stored for the uncorrected event plane, for positive and negative η separately. The distributions should be centered around zero in the case of a perfect detector. In case of any deviation, for example a gap at one side of the detector, the distribution is slightly shifted. For the correction this deviation from zero, the mean value of Q_x and Q_y, are subtracted from every Q-vector in the calculation of the event plane. As shown in the right plot in figure 5.4, the result is an almost flat event plane distribution. The used Q_x and Q_y distributions and the mean values are shown in the appendix A.1.

An inverse ϕ weight can be used as a different method for the correction [19]. An additional weight is applied which is extracted from the ϕ distribution of the tracks. Each track which is used in the sum to calculate the Q-vectors is weighted by the inverse of the bin content of the ϕ distribution for the current ϕ of the track. This method produced a similar result as obtained by recentering. The results for a subset of the data is shown in the appendix A.2. In the following the correction with recentering is used in the analysis.

Due to the finite number of particles which are used in the event plane calculation the resulting event plane angle has a limited resolution [20]. In figure 5.5 the event plane for the positive and negative pseudo-rapidity range is depicted where the correlation between the two values is visible. The event plane resolution can be calculated by using the difference $\Psi_{\eta>0} - \Psi_{\eta<0}$ [20]. In figure 5.6 the resulting distribution of $\Psi_{\eta>0} - \Psi_{\eta<0}$ is shown. A fit of a Gaussian function is used to estimate the width of the distribution. A value of $\sigma = 18°$ was found which is divided by a

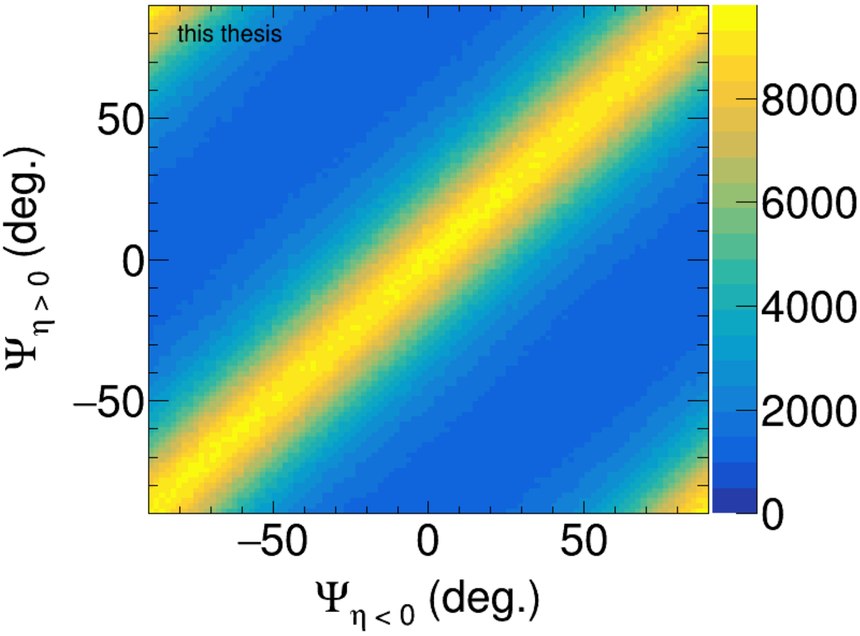

Figure 5.5.: Correlation of the event plane angle Ψ_2 between positive (y-axis) and negative (x-axis) η.

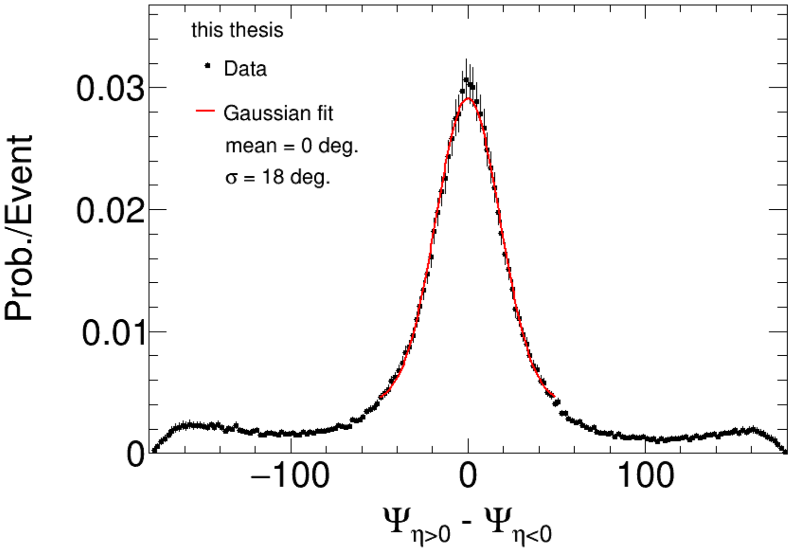

Figure 5.6.: Distribution of the probability per event of the difference $\Psi_{\eta>0} - \Psi_{\eta<0}$ and a fit of a Gaussian function (red) with a width of $\sigma = 18°$.

factor $\sqrt{2}$ in order to avoid the double counting and get the resolution of the full event plane. A result of $\Delta\Psi_2 = 12.73°$ is obtained for the resolution of the full event plane. As described later in section 5.3 only events with similar event plane angles are used for the mixed event, where a classification of the events into event plane bins is done. A limit of this binning is represented by the event plane resolution.

As already mentioned in the introduction in section 2.2 the elliptic flow has great impact on the background of jet measurements. Particle correlations due to the anisotropic distribution of tracks have to be eliminated in jet correlation measurements. The description of the uncorrelated background by the mixed events, which consists mainly of particles from the bulk, is influenced by the elliptic flow too. This effect is studied in more detail in section 6.4.1. In the next section the introduction of the mixed event production follows.

5.3. Event mixing

The general concept of mixed events for the description of uncorrelated background was already used successfully in several measurements. They are useful in correlation measurements of observables where a large background arises due to the false combination of uncorrelated objects within one event. This background can be estimated by using mixed events where only uncorrelated objects are assigned. By construction no true correlated objects can be found in the mixed events.

One example is the reconstruction of J/Ψ mesons from the e^+e^- decay channel as performed in [77]. The reconstructed J/Ψ candidates from combinatorial background are rejected by using uncorrelated electrons and positrons from different events, the mixed events. The obtained invariant mass distribution of the mixed electron positron pairs is subtracted from the measured distribution in order to obtain the signal of real correlated pairs. In [78] and [79] mixed events are used for the search of event-by-event fluctuations of the mean transverse momentum of the particles within an event. The distribution of the mean transverse momentum is well described with the distribution obtained from mixed events. This implies that a large contribution arises from statistical fluctuations and dynamical fluctuations are much less significant.

In the jet analysis mixed events will be used as a new approach to get a description of the uncorrelated background in jet measurements. The aim is to perform unbiased jet measurements without cuts on the reconstructed jet energy down to low p_{T}. In this section the production of the mixed events as well as some characteristics are described. The general procedure follows the description in [45] where the mixed events were successfully used in the semi-inclusive h-jet measurement. In the following the real events are called same events (SE) to distinguish them from the mixed events (ME).

The aim of the ME is to describe the uncorrelated background of reconstructed jets. Thus all jet like correlations have to be destroyed. This is done by selecting tracks from different real events and put them together to one ME. In particular only one track is used from every event. This guarantees the destruction of all correlations between the particles. The ME used in J/Ψ measurements as described above, is produced by assigning uncorrelated e^+e^- pairs from different events. In comparison, the full event is mixed for the jet measurements because jets are large objects in space. In addition jets are multi-particle objects with an unknown number of particles. In order to describe the uncorrelated background jets the same jet reconstruction is carried out for the ME as it is done for the SE described in section 5.1.

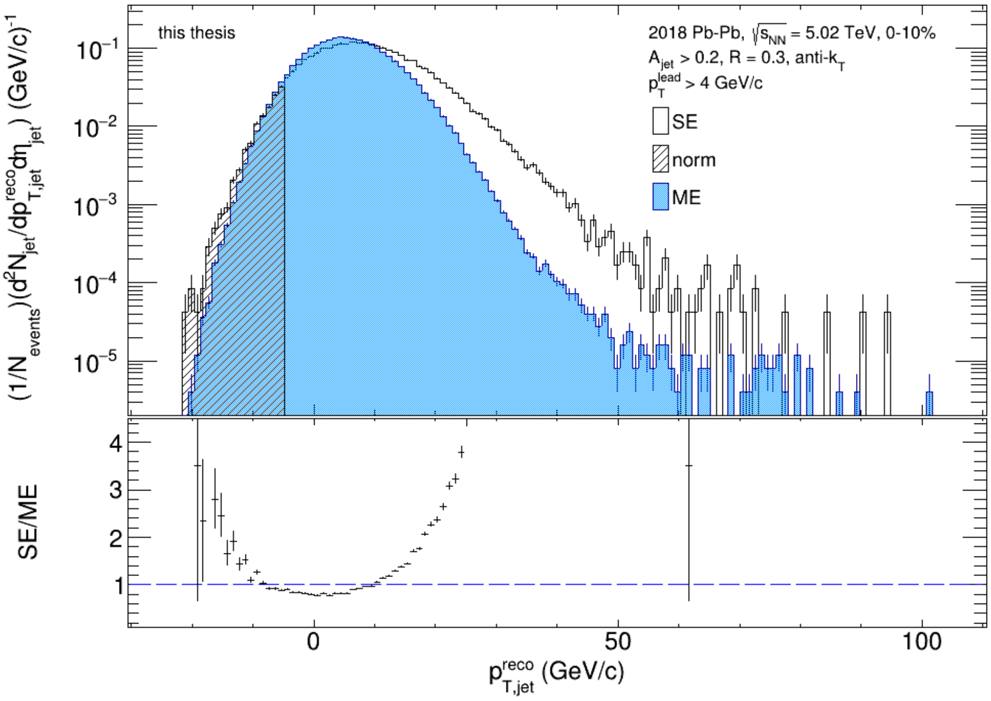

Figure 5.7.: Raw SE (black) and ME (blue) jet p_T distributions with a 4 GeV/c bias as function of $p^{reco}_{T,jet} = p^{jet}_T - \rho A$. The range for the normalization of ME to SE is indicated by the shaded region. The ratio SE/ME is depicted in the lower panel. For the ME production randomly selected events and multiplicities were used.

As a first approach the SE and ME jet distributions are studied by producing the ME simply out of random tracks from different events, without a deeper look at the event properties. Figure 5.7 shows the resulting jet distribution. A biased jet population is shown where the transverse momentum of the leading track p_T^{lead} of the jets is required to be larger than 4 GeV/c in the SE and ME. The bias is just a choice which was made. Different values and a detailed discussion of the quasi-inclusive jet distribution follows in section 7.2. In this section the focus is only on the production of the ME background jet population.

The SE jet distribution is depicted in black and the ME distribution in blue. The shaded region indicates the normalization region which is used to normalize the ME to the SE. The normalization is done only up to -5 GeV/c which is a choice where less jets are expected. The region which is used for the normalization is studied later in more detail 6.2. In addition both distributions are normalized to the number of used events in the jet reconstruction N_{events}. The jet yield is shown as function of $p^{reco}_{T,jet}$ which is given by the raw jet p_T where the background energy density ρ scaled by the jet area A_{jet} was subtracted as shown in equation 2.11. An area cut of $A_{\text{jet}} > 0.2$ was used.

In order to produce the ME, different randomly selected real events are used. For the multiplicity of the ME a random value from the middle of the SE multiplicity distribution was used. This random selection of the events for the mixing results in a large discrepancy between the SE and the ME distribution at low $p_{\text{T,jet}}^{\text{reco}}$. In the low $p_{\text{T,jet}}^{\text{reco}}$ region at the left side tail a similar distribution of SE and ME is expected because all reconstructed objects in the SE are expected to be uncorrelated background. The yield of the ME is too low in this region while it exceeds the SE distribution between -5 and 10 GeV/c.

The particle distribution in the SE is influenced due to the elliptic flow or the z-vertex position of the event which are not considered in the ME. All those additional effects of the events are destroyed by the mixing procedure if one random track is used in the mixing without a further specification of the real events. Thus no reasonable description of the uncorrelated background in the SE by the ME can be obtained by using events of all classes in the mixing procedure and by no further definition of the ME multiplicity. As a solution to improve the description of the uncorrelated background in the SE by the ME, the event categorization as presented in [45] is introduced in the following.

5.3.1. Event categorization

For the description of the uncorrelated background in the SE jet distribution by the ME a realistic reproduction of the SE properties is required. Therefore the event categorization for the mixing is introduced in this section. In [45] it is proposed that one ME should be only created out of real events which are similar within the centrality, the event plane and the z-vertex position. In the following an overview of the basic rules to produce the ME is presented:

- The multiplicity of the ME is sampled from the SE multiplicity
- One random track is used from N real events to produce a ME with N tracks

Only real events which have the same topology are used for the mixing. For one ME N events which are similar in the

- centrality (10 multiplicity bins within the 0-10% bin)
- event plane angle (10 event plane bins, each of 18°)
- z-vertex position (4 z-vertex bins, each of 4 cm)

are used. In the following the mixing procedure is described in more detail.

In order to do the mixing only among events with equal properties, it is necessary to classify all events and divide them into different categories before the mixing is done. In total 400 different categories are used. Four classes of events are created for the different z-vertex positions. Due to the strong z-vertex dependence of the ITS, as described in section 4.2, only events with $|\text{z-vertex}| < 8$ cm are used and the events are separated into four different z-vertex bins each of 4 cm. For the analysis only the 0-10% centrality class is used but an additional splitting of the events into 10 multiplicity bins is applied. The bin width is chosen such that all bins contain the same number of events. The multiplicity bins are listed in table 5.1 and shown in the next section in figure 5.8. The events with smaller multiplicities than 1800 or larger multiplicities than 2986 are discarded because they are only a very small fraction of the total events as shown in figure 4.1. The last categorization depends on the event plane, where 10 bins each of 18 degrees are used. The estimation of the event plane was already described in section 5.2.

Table 5.1.: Multiplicity bins used for the production of the ME.

Bin	0	1	2	3	4	5	6	7	8	9
Mult.	1800-1961	1962-2045	2046-2125	2126-2209	2210-2297	2298-2389	2390-2489	2490-2597	2598-2721	2722-2986

For each of the 400 categories a new TTree is created, which contains the same information regarding the track parameters as the original produced TTrees, but only a certain class of events as described above. In addition, the calculated event plane angle as well as histograms with the multiplicity and z-vertex distributions are stored. The advantage of the splitting into the different TTrees is explained later in this section.

In the following the categorized TTrees are used for the jet analysis. In a loop over the events the categorized TTrees are opened one after the other such that only events within the same class are loaded at the same time. For each event the category in terms of z-vertex bin, event plane bin and multiplicity bin is determined. In addition a sub bin can be obtained for each z-vertex and event plane bin which will be described later. The event number is kept for the appropriate category in a multidimensional vector. As soon as more events of one category than the upper edge of the corresponding multiplicity bin are loaded, the mixing starts.

A loop over all events of the current category starts again which is possible because the event numbers are saved before. The cuts on the tracks as described in 4.2 are applied and the remaining tracks of the events are stored in a TLorentzVector. After that a random multiplicity is selected from the SE multiplicity distribution. As input for the sampling of the multiplicity, histograms of the SE multiplicity distribution for all 400 categories are used. As the multiplicity, event plane and z-vertex bin was determined before, the appropriate histogram can be selected. The mixing starts and one random track is taken from every event until the desired number is reached. With this procedure all jet correlations between the particles are destroyed and only uncorrelated tracks are left by construction which can be used to describe the uncorrelated background. The mixed tracks are stored in a PseudoJet vector which is used as input for the jet reconstruction with FastJet as described in section 5.1.

The jet reconstruction in the ME is done with the same setup as the reconstruction in the SE which is described in section 2.3.1 and 5.1. The only difference between SE and ME is the choice of removed jets for the ρ calculation. While for the SE some jets with the largest energy are removed, to ensure no real jet goes into the background calculation, no jet is removed for the ME. By construction all jets which are reconstructed with the anti-k_T algorithm are uncorrelated background jets in the ME but further studies are presented in 6.3.

There are three different possibilities how many ME can be produced from the SE. In the following it is assumed that enough events of one category (upper edge of the multiplicity bin) are loaded into the buffer. For example 1961 are enough for the first multiplicity bin to start the mixing. In a first approach only one single ME is produced because only one track is used from each event and the other tracks are discarded. This would always result in much more SE (1961 events) than ME (only 1 event) in each mixing procedure. Alternatively each used track could be removed from the events as soon as it was used in one ME. This guarantees again that each track is only used once in all ME and would reproduce an amount of ME given by the lower edge of the multiplicity bin (1800 events) in comparison to the upper edge for the SE (1961 events). However, this method requires more computational effort.

In addition it is possible to produce an arbitrary number of ME out of the 1961 SE by using the events several times without removing the tracks. We repeat the mixing procedure N times, where N is the average of the multiplicity bin ($N = 1880$ in the example of bin 0). The usage of the average of the multiplicity bin is one choice and other values are possible too. Some tracks might be used twice, but on a statistical level the ME are unique with this procedure. After the N iterations the used events for the mixing are discarded and the loop over the same events continues. The mixing starts again as soon as there are enough events of one category in the buffer. While waiting for enough events to do the mixing, the SE jet reconstruction is ongoing for each event.

Since the mixing should be done only among events which are within the same class, one has to ensure that enough SE of the different classes are provided. Due to technical limitations the splitting of the TTrees into the different categories was necessary because the size of all root files, which contain the events, is about 2.5 TB. Therefore not all events can be loaded into the memory at the same time. Alternatively one could jump on the disc from event to event, depending on which one is needed for the mixing. However this procedure makes the process of creating the mixed events very slow. As solution the TTrees are separated into the different categories. With the classified TTrees the events are read in category by category because they are ordered, which enables an earlier mixing and thus prevents the loading of too many events at the same time.

At the end, the ME jet p_T distribution as well as distributions of other properties as ρ are normalized to the corresponding SE distribution by their integrals. This is done for each category to ensure that there arises no differences due to different amounts of SE and ME in the different classes. After that the histograms can be merged for the different categories to obtain the full distribution.

In the next section the multiplicity and track distribution of the ME is studied in more detail before the resulting jet distributions of the SE and ME with the event categorization follow.

5.3.2. Multiplicity and track distribution of the mixed events

For further comparison of the SE and ME their charged particle multiplicity and track distributions are studied. Because the multiplicities for the ME are sampled from the SE multiplicity distribution the same distribution is obtained as shown in figure 5.8. The SE multiplicity distribution is depicted in blue (circles) and the ME distribution in red. The dashed lines represent the edges of the different multiplicity bins listed in table 5.1.

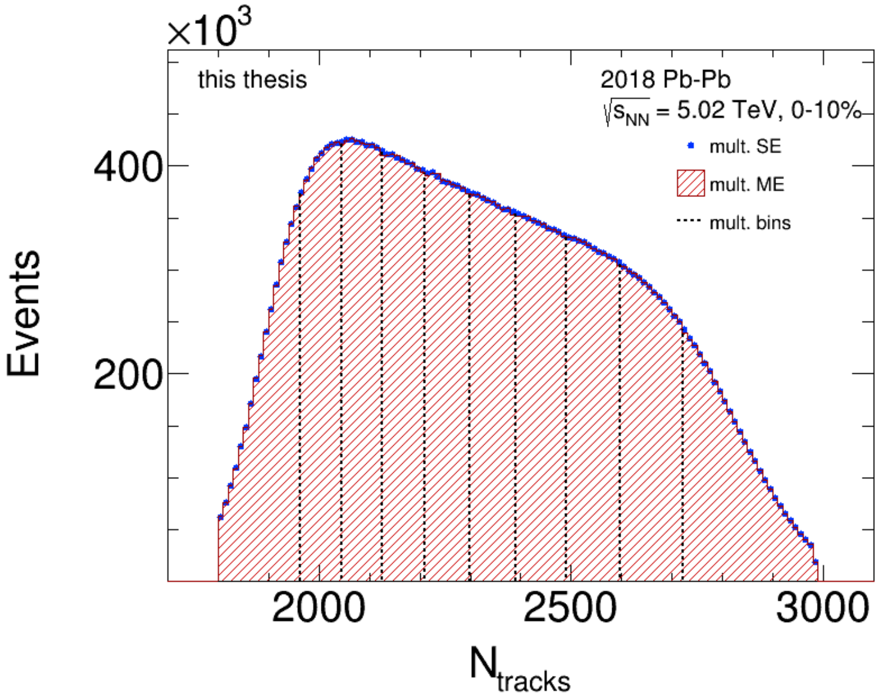

Figure 5.8.: Multiplicity distribution of SE (blue points) and ME (red) of the data which was divided into the 400 categories. The black dashed lines indicate the 10 multiplicity bins used for the mixing.

By producing exactly the same multiplicities in the ME distribution it is ensured that no differences in the resulting jet energy distributions between ME and SE arises due to different multiplicities. The only difference between SE and ME which should be produced by the construction is the destruction of the jet correlations. For the sampling separate input histograms of the SE multiplicity distribution for each of the 400 categories are used. This is necessary because the multiplicity distribution of the different multiplicity bins depends on the current z-vertex and event plane bin too. Without this separation small differences between the SE and ME multiplicities were observed.

For the event plane this exact reproduction of the SE distribution with the ME is not possible. With a known event plane angle the tracks for the ME can not be distributed in an explicit way corresponding to the given angle. Only events with similar event plane angles can be used within the mixing to reproduce at least a ME which is close to the real events regarding the event plane. In addition, the limiting event plane resolution prevents an exact reproduction of the SE event plane

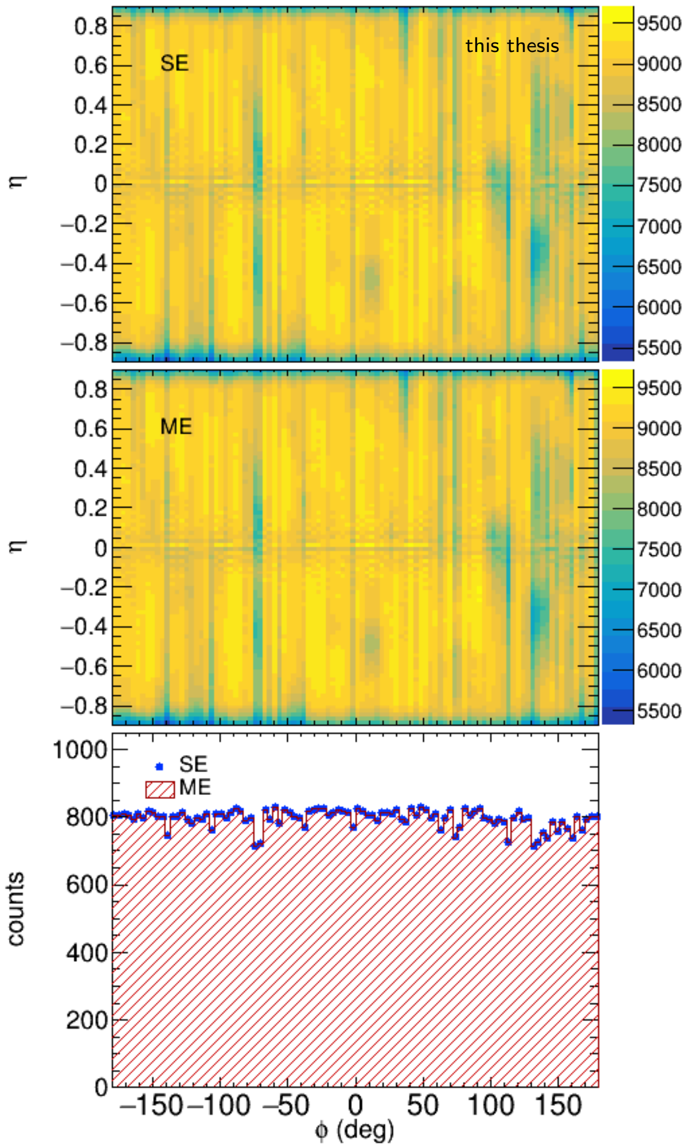

Figure 5.9.: $\eta - \phi$ distribution of charged tracks for SE (upper panel) and ME (middle panel) and projections to the x-axis (lower panel) for SE (blue points) and ME (red).

angle. The event plane dependence of the ME and the resulting description of the background in SE is studied in more detail in section 6.4.1.

In addition all acceptance effects from real data are reproduced in the mixed events. Figure 5.9 shows the $\eta - \phi$ distribution for the SE (upper panel) and ME (middle panel) and the ϕ projections for SE and ME (lower panel). Both distributions for SE and ME are in a perfect agreement. Despite the coincidence of the distributions for all events, there may still be differences in the SE and ME apart from the jet correlations on an event-by-event basis. The classifications into event plane, multiplicity and z-vertex bins might not be enough in order to do the mixing only among similar events. The dependence on the used bins for the mixing is studied in more detail in section 6.4. It will turn out later, that additional bins for the mixing regarding the p_{T} fluctuations of the same events are necessary. A further binning of the events into equal sums of all transverse momenta of the tracks in the SE will be introduced later in section 6.6.

Additional other correlations in the SE are destroyed in the mixing procedure. For example all decay particles of resonances, as the Δ resonance, are correlated objects. In addition to the elliptic flow v_2 there exist correlations due to the other flow coefficients v_n. They might be the reason for some remaining differences between the SE and ME.

In addition other approaches exist for the production of mixed events. For example the η and ϕ values of real tracks from the SE could be kept for the ME and only the track p_{T} could be mixed. This would be a solution for the track distribution on an event-by-event basis but the problem of the event plane reproduction is not fully solved. As given in equation 5.3 the event plane angle is calculated with a p_{T} weight of the tracks and thus it depends on the p_{T} distribution too. There is no clear solution how to distribute the energy of the tracks. In addition the results might have some remaining jet correlations which are destroyed if only one particle per event is used in the mixing as described above.

5.3.3. Same and mixed event jet distribution

The resulting jet distributions of the SE and ME with the event categorization described above are shown in figure 5.10. Again the quasi-inclusive jet distribution with all jets with a leading track p_{T} above 4 GeV/c are presented. The setup for the jet and background reconstruction as described in 5.1 is used where three jets with the largest energy are removed in the SE ρ calculation and zero in the ME. The used data set is a subset of 10% of the full statistics with one multiplicity bin (bin 0: 1800-1962) and all event plane and z-vertex bins.

A clear improvement of the SE (black) description by the ME (blue) is found in comparison to the ME without the event categorization which was shown in figure 5.7. The distributions are again normalized to the number of used events N_{events} and in addition the ME is normalized to the SE within the shaded region up to -5 GeV/c. As expected the description of the SE by the ME at negative $p_{\mathrm{T,jet}}^{\mathrm{reco}}$ improves if the categories are used in the mixing. In the lower panel the ratio SE/ME is almost one for negative $p_{\mathrm{T,jet}}^{\mathrm{reco}}$. At positive $p_{\mathrm{T,jet}}^{\mathrm{reco}}$ the ratio SE/ME grows as expected, since the uncorrelated background becomes smaller with larger jet p_{T}.

The good description of the SE by the ME implies that the features of the SE, as the event plane orientation or the z-vertex position could be reproduced by mixing only events within the same category. It becomes obvious that the reconstructed jet population depends on the event plane, the multiplicity and the z-vertex of the events. All those features are missing in the ME if random events are used for the mixing because all particle correlations for example from flow are destroyed. With the categorization into 400 different classes a very good description of the uncorrelated background in the SE can be obtained.

In the next section systematic variations to study the behavior of the description of the uncorrelated background by the ME are presented. Different properties of the SE and ME and their jet distributions are studied.

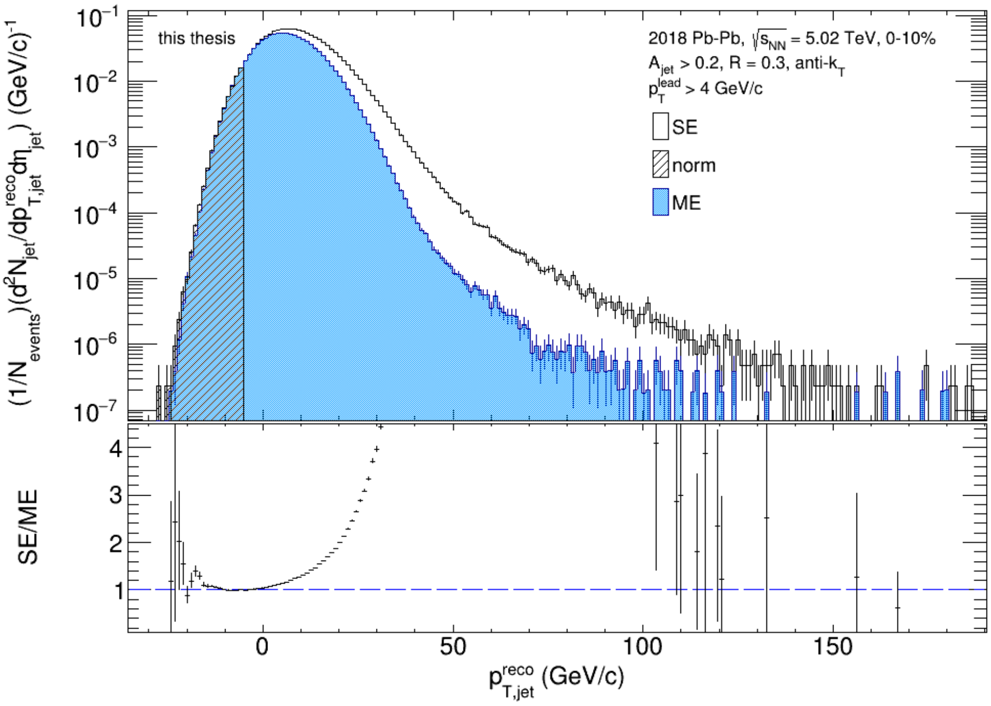

Figure 5.10.: Raw SE (black) and ME (blue) jet p_T distributions with a 4 GeV/c bias as function of $p_{\mathrm{T,jet}}^{\mathrm{reco}} = p_{\mathrm{T}}^{\mathrm{jet}} - \rho A$. The range for the normalization of ME to SE is indicated by the shaded region. The ratio SE/ME is depicted in the lower panel. For the ME production only events within the same category (multiplicity bin 0, event plane bin 0 and z-vertex bin 0) are mixed.

6. Systematic studies of the mixed events

In this section different systematic studies of the ME are presented. The systematic studies are done with a subset of 10% of our full data set with 40 out of the 400 categories, where the exact selection depends on the particular study.

While the focus in this section is on the quasi-inclusive jet distribution with a 4 GeV/c bias, the studies were performed for the inclusive and h-jet distributions too. Similar solutions regarding the systematic studies were found in all cases. For the biased jet distribution all jets in the SE and ME which are reconstructed with the anti-k_T algorithm are used with the requirement that they have at least one constituent with $p_\mathrm{T} > 4$ GeV/c.

The modifications are done in order to study the mixed event behavior and stability and to find the best description of the uncorrelated background in the SE. To ensure no objects from real jets are included in the ME a splitting of the high momentum tracks in the ME is introduced 6.1. In section 6.2 different normalization regions for the ME are used in order to study the description of the uncorrelated background in the SE. In addition the area and ρ distributions are analysed in section 6.3 where variations of the hardest jets which are removed for the ρ calculation in the SE and ME are presented 6.3.1. In 6.4 different studies concerning the classes for the production of the mixed events were done, where smaller event plane and z-vertex bins are used. In particular the event plane dependence is studied in 6.4.1 as correlations from flow are expected to have a great impact on the uncorrelated background description by mixed events. A run dependent observation in the inclusive jet distribution is reported in section 6.5. In the last section 6.6 an observation of the p_T fluctuations in the SE and ME as well as the introduction of an additional binning for the mixing is described.

6.1. Splitting of high momentum tracks in the mixed event

To described the fully uncorrelated background with the ME it is necessary to ensure a ME production without major fractions from real jets. Because only one random track is used from each real event to produce a ME no real jet correlations are present in the ME. But it is still possible to reconstruct a true jet which is driven by one high p_T particle if this particle is selected for the ME. The reconstructed object in the ME would have nearly the same energy as the true jet. This was already observed in figure 5.10, where lots of entries in the ME distribution at large jet p_T above 70 GeV/c are visible. In this high p_T regime we expect the reconstructed jets to be true jets. These high p_T objects in the ME are the reason for the introduction of the splitting of the leading tracks in ME as presented in the following.

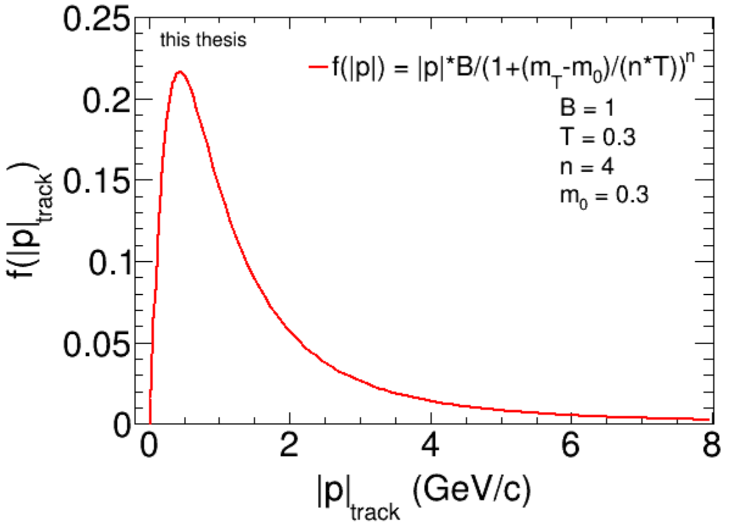

Figure 6.1.: Distribution used for the splitting of the high momentum tracks in the ME.

In order to do this all tracks with momenta $|p|$ above some certain threshold are divided into N collinear tracks with smaller momenta. The $\eta - \phi$ position of the original track is not modified and stays the same for all tracks. The momenta of the divided tracks are sampled from a Levy function [80] as shown in figure 6.1, until the original momentum of the initial particle is reached. The last track simply gets the remaining energy to guarantee that the initial energy is not modified. The Levy function was used in [80] to described the invariant yields of pions and protons between 0.3 and 10 GeV/c measured in p+p and d+Au collisions. It is defined in equation 6.1 with $T = 0.3$, $n = 4$, $B = 1$, $m_0 = 0.3$ and $m_\mathrm{T} = \sqrt{p_\mathrm{T}^2 + m_0^2}$.

$$f(|p|) = |p| \cdot \frac{B}{(1 + (\frac{m_\mathrm{T} - m_0}{n \cdot T}))^n} \tag{6.1}$$

Only one of the new tracks can participate in a single ME because only one track from each event is kept. With this splitting of the high momentum particles no high p_T objects from real jets which result in partly true reconstructed jet energies are left.

In QCD there is no difference between a jet driven by one high momentum track or the same jet with multiple collinear particles with lower momenta. A sketch is shown in figure 6.2 where one jet with a single high p_T particle (left) and the same jet with multiple lower p_T particles (right) which point in the same direction is depicted. As long as the total jet energy and the direction of the particles stays the same, the two jets can not be distinguished and are equal objects. The only change which is introduced by the splitting is a change in the multiplicity of the event which is slightly enhanced. As the multiplicity of the ME is sampled from the SE multiplicity distribution this does not change the multiplicity distribution of the

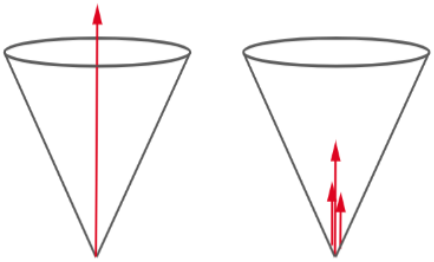

Figure 6.2.: Sketch of a jet with one high p_{T} particle (left) and with multiple lower p_{T} particles (right). As long as the jet energy and the direction of the particles is the same, there is no difference between the two cases.

ME. In addition all divided tracks get different momenta and thus it is not possible that some particles being taken twice which would be the case if the original track is divided into N equal tracks.

The impact of this splitting on the jet spectra is shown in figure 6.3. The same subset of 10 % of the whole data set was used as for the jet distribution in figure 5.10. In addition, the same setup for the jet reconstruction was used to get a reasonable comparison. Again all reconstructed jets with a leading track with $p_{\mathrm{T}}^{\mathrm{lead}} >$ 4 GeV/c are accepted and this bias is applied to the SE and ME jet population. The plot shows the reconstructed jet distribution for SE (black) and ME with (red) and without (blue) the splitting as function of $p_{\mathrm{T,jet}}^{\mathrm{reco}}$. The shaded region is the normalization region. It is used to normalize the ME to the SE distribution in the region where no true jets are expected. This is studied in more detail in section 6.2. In addition the normalization to the number of events N_{events} was applied.

All tracks in the ME (red) with $|p| > 10$ GeV/c are split into tracks with smaller momenta between 0.15 and 3 GeV/c in the way described above. In the resulting distribution all high p_{T} objects in the ME are rejected and the ratio SE/ME grows for $p_{\mathrm{T,jet}}^{\mathrm{reco}} > 0$ GeV/c. In comparison lots of entries in the ME (blue) distribution at large jet p_{T} above 50 GeV/c are visible before the splitting of high momentum tracks was applied. At the left side of the distribution below $p_{\mathrm{T,jet}}^{\mathrm{reco}} = 0$ GeV/c no large differences between the ME with and without the splitting are visible. A very good description of the uncorrelated background in the SE is obtained between -15 and 0 GeV/c where the ratio SE/ME is one. Small deviations of 2-3 sigma are observed below $p_{\mathrm{T,jet}}^{\mathrm{reco}} = -15$ GeV/c where in addition the jet yield has already fallen by three orders of magnitude below a jet $p_{\mathrm{T,jet}}^{\mathrm{reco}}$ of -20 GeV/c in comparison to the peak.

For further studies, the threshold of the splitting is varied. In order to get a better comparison between the different jet populations, the correlated jet distribution is studied in the following. Figure 6.4 shows the correlated jet distribution, where the ME was subtracted from the SE, without the applied splitting of the high momentum tracks (blue), with a 10 GeV/c threshold (black) and for comparison a threshold of 15 GeV/c (red) was used. In both cases the splitting into tracks with momenta between 0.15 and 3 GeV/c was performed. Only small differences between the three curves are visible. The signal is slightly larger if the 10 GeV/c threshold was used in comparison to the 15 GeV/c threshold or no splitting. This

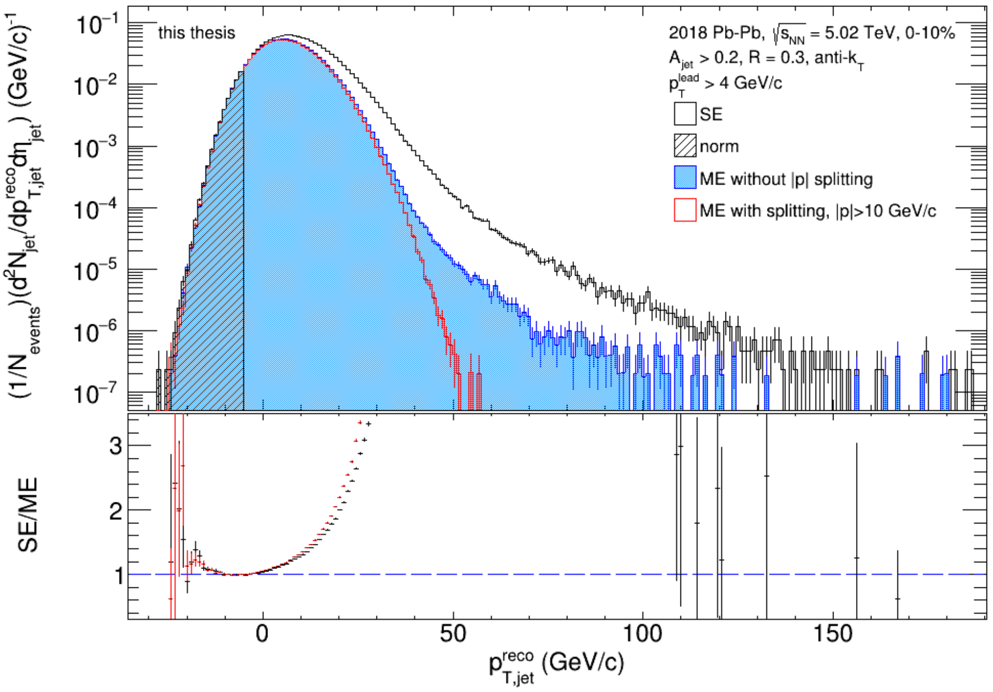

Figure 6.3.: Raw SE (black) and ME jet $p_{\mathrm{T,jet}}^{\mathrm{reco}}$ distributions with $p_{\mathrm{T}}^{\mathrm{lead}} > 4$ GeV/c. The range for the normalization of ME to SE is indicated by the shaded region. The ME distribution is shown without (blue) and with (red) the splitting of the high momentum tracks with $|p| > 10$ GeV/c. The ratios SE/ME are depicted in the lower panels.

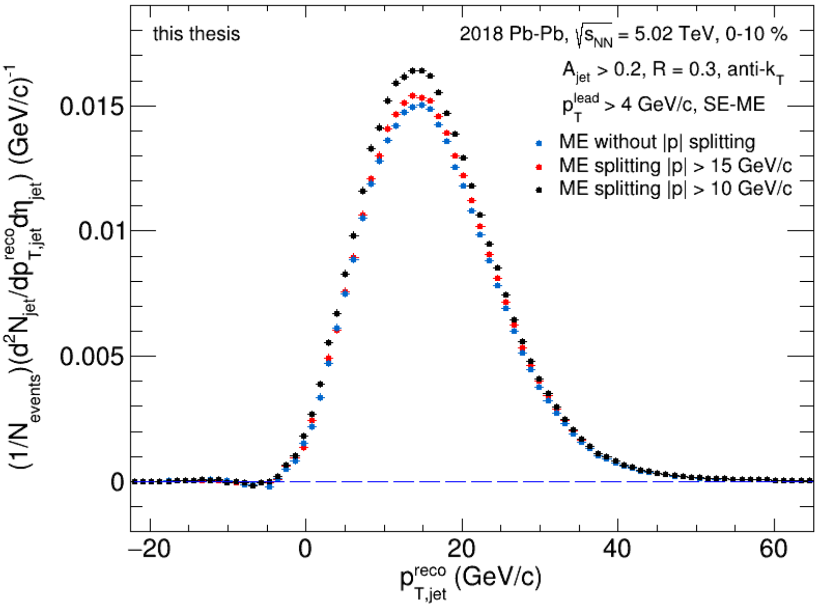

Figure 6.4.: Raw correlated quasi-inclusive jet distribution (SE-ME) with a bias of $p_{\mathrm{T}}^{\mathrm{lead}} > 4$ GeV/c. The ME without momentum splitting (blue) and with momentum splitting with 15 GeV/c threshold (red) and 10 GeV/c threshold (black) was used. The distributions are normalized to the number of events N_{events}.

was expected since reconstructed objects from high p_{T} particles are removed and the reconstructed jet population in the ME is slightly reduced which results in a larger SE-ME distribution. In all three cases a very good description of the uncorrelated background in the SE by the ME distribution is observed. Almost no deviations from zero are visible at the left side at low jet p_{T}. The small yield at negative $p_{\mathrm{T,jet}}^{\mathrm{reco}}$ arises due to background fluctuations and is expected as shown in section 5.1.

However, the main difference between the ME with and without the high momentum splitting of leading tracks is the rejection of the high p_{T} objects in the ME which was the aim of this procedure. In the following the high momentum splitting for the ME is always applied with a 10 GeV/c threshold unless otherwise stated.

More studies can be done by using other thresholds for the splitting or by varying the momentum range of the divided tracks. In addition, the function given by equation 6.1 describes only one choice to distribute the tracks for the splitting. Other functions as input could be used for some further studies of the splitting of high momentum tracks in the ME.

6.2. Normalization

As already mentioned in 5.3, the ME distributions are normalized to the SE distributions within each category by their integrals over the full range. This is done for each event category to ensure no differences arise due to different amounts of same and mixed events. Thus the integrals of the SE and ME distributions are in agreement. Since there are no entries in the ME at high $p_{\mathrm{T,jet}}^{\mathrm{reco}}$ the yield at low jet $p_{\mathrm{T,jet}}^{\mathrm{reco}}$ is larger as for the SE. In order to use the ME distribution for the subtraction of the uncorrelated background in the SE, it is necessary to perform an additional normalization within the region where only uncorrelated background is expected. In the previous section the jet $p_{\mathrm{T,jet}}^{\mathrm{reco}}$ distributions for SE and ME are presented with an additional normalization of the ME to the SE in the region from the left side of the distribution up to -5 GeV/c.

In this section different normalization regions are studied. Since the ME should be normalized to the SE only within the region where all reconstructed objects are uncorrelated background a normalization at negative $p_{\mathrm{T,jet}}^{\mathrm{reco}}$ is not possible. As shown in section 5.1 background fluctuations might lead to jet correlations at $p_{\mathrm{T,jet}}^{\mathrm{reco}} < 0$ GeV/c. In the case of a 4 GeV/c biased jet distribution only jets with $p_{\mathrm{T,jet}}^{\mathrm{reco}} > 4$ GeV/c are candidates for true correlated jets however deviations due to background fluctuations are possible. As presented in [45] variations of the normalization region should be done in order to find the most appropriate region which is identified by the left most normalization region which can be used in order to obtain a flat SE/ME ratio at unity. The additional scaling factor which is applied to the ME is labeled with f^{ME}.

For this study the SE and ME jet distributions with a 4 GeV/c leading track cut are used as shown in figure 6.3 where the splitting of all tracks in the ME above 10 GeV/c was applied.

The ratio of the SE and ME jet distribution as function of $p_{\mathrm{T,jet}}^{\mathrm{reco}}$ for different normalization regions is depicted in figure 6.5. The ratio SE/ME where only an absolute normalization of the ME to the SE jet distribution was performed is depicted in green. In this case a large deviation from unity is observed at $p_{\mathrm{T,jet}}^{\mathrm{reco}} < 0$ GeV/c, where the ME should describe the uncorrelated background in the SE. As expected, the yield of the ME distribution is larger than the yield of the SE distribution at low jet p_{T} which results in a ratio SE/ME < 1.

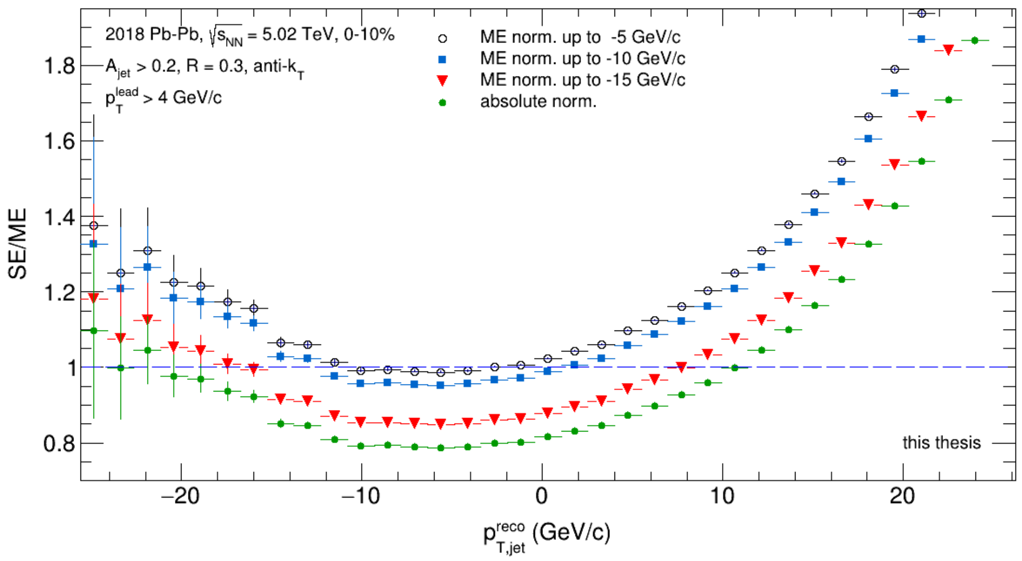

Figure 6.5.: Ratio of the SE and ME raw jet distributions with a 4 GeV/c bias. The setup for the jet reconstruction is the same as for figure 6.3. Different normalization regions are used to normalize the ME to the SE distribution with a lower value of −35 GeV/c and −5 GeV/c (black), −10 GeV/c (red) and −15 GeV/c (blue) as upper value. In addition only the absolute normalization was done (green).

In addition, the results for normalization regions from −35 GeV/c up to −15 GeV/c (blue), −10 GeV/c (red) and −5 GeV/c (black) are presented. An improvement of the description of the uncorrelated background by the ME is observed if an additional normalization is done and the SE/ME ratio gets closer to one if a larger region is used. While still a large difference in the ratios is observed between −15 GeV/c and −10 GeV/c as an upper edge for the normalization, the improvement becomes smaller if −5 GeV/c is used. However, between −13 and −2 GeV/c the ratio is almost equal to one if the ME is normalized to the SE up to −5 GeV/c, while a deviation of 5% is observed for −10 GeV/c as upper edge.

The integrals of the SE and ME raw jet distributions, after the normalization, are listed in table 6.1. In addition the scaling factor f^{ME} is shown which was used to normalize the ME to the SE distribution. The scaling factor becomes smaller for larger normalization regions which results in a smaller integral of the ME after the scaling. The discrepancy between the integrals of the SE and ME gets larger with larger normalization regions. By increasing the region by 5 GeV/c the integral of the ME decreases by 0.04. Differences between the SE and ME integrals of 12% to 25% depending on the normalization region are observed.

As the best description of the uncorrelated background in the SE by the ME is obtained by a normalization region up to -5 GeV/c this is used as default value in the following.

Table 6.1.: Integrals of the SE and ME reconstructed jet distributions with $p_T^{\text{lead}} > 4$ GeV/c and scaling factor f^{ME} for different normalization regions.

Norm. region	**Integral**		$\mathbf{f^{ME}}$
	SE	ME	
absolute	1.28	1.28	1
-35 to -15 GeV/c	1.28	1.13	0.89
-35 to -10 GeV/c	1.28	0.99	0.77
-35 to -5 GeV/c	1.28	0.95	0.75

6.3. Area and ρ distributions of same and mixed events

For further studies and comparison of the same and mixed events the area distribution of the jets and the ρ distributions of the events are compared. The results of all jets which are reconstructed with the anti-k_T and k_T algorithm are presented and no further cuts are applied. For the background reconstruction a jet radius of $R_{\text{bckg}} = 0.3$ was used and the three hardest jets are removed for the ρ calculation in the same event. This value is varied in section 6.3.1.

In figure 6.6 the area distributions of the reconstructed jets in the SE (blue points) and the ME (red) are depicted. Both distributions are very similar and no significant deviations are observed. As expected from the used jet radius of $R = 0.3$, the maximum is reached around $A_{\text{jet}} = \pi R^2$. This value is depicted as dashed line in the figure. The distribution drops afterwards. Lots of the reconstructed jets have a very small jet area $A_{\text{jet}} < 0.02$. In order to reject these jets an area cut of $A_{\text{jet}} > 0.2$, depicted as solid line, is applied. About one half of the reconstructed jets are discarded with the area cut. The cut off value for the area was taken from [45] and could be changed later. In general area cuts are applied to reject small reconstructed jets which contain only a few particles. However, these are mostly low p_T objects in which we are particularly interested. Further studies on this area cut will be carried out in the future.

The agreement between the areas of the SE and ME indicates that the presence of uncorrelated background do not affect the area distributions of the reconstructed jets. In addition the true correlated jets have a minor influence which was already observed in [45].

Figure 6.7 shows the ρ distributions of the SE (upper) and ME (lower) in dependence of the track multiplicity N_{tracks}. The event-to-event background energy density ρ is calculated as the median of the raw jet p_T scaled by the jet area given by equation 2.10. The k_T algorithm is used with a jet radius of $R_{\text{bckg}} = 0.3$. In the SE the three jets with the largest p_T are not considered in this estimation to exclude at least the true highest p_T jets from the background calculation. For the

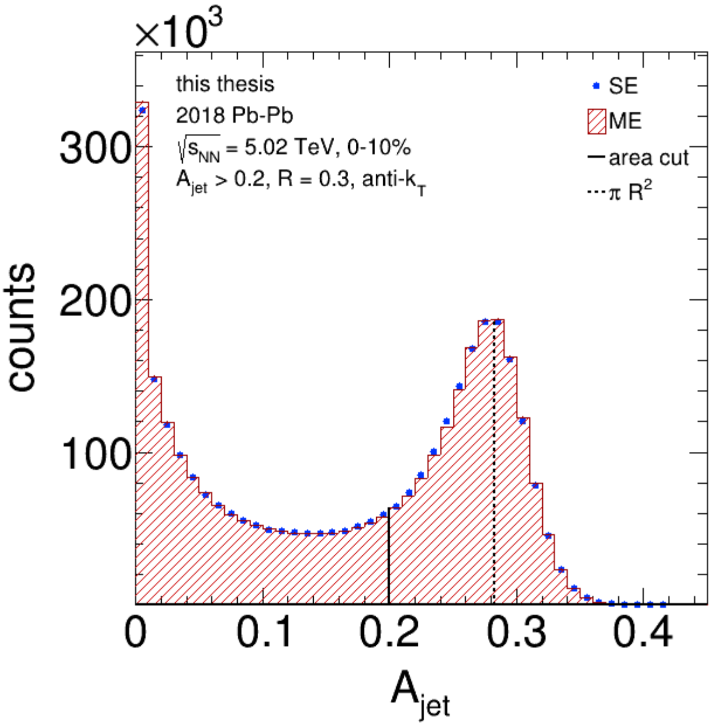

Figure 6.6.: Area distributions of all objects reconstructed with the anti-k_T algorithm and $R = 0.3$ for SE (blue) and ME (red). The area cut of $A_\mathrm{jet} > 0.2$ is represented by the solid line and the jet area at $A_\mathrm{jet} = \pi R^2$ by the dashed line.

ρ calculation in the ME no jets are removed because only uncorrelated background is assumed. The number of jets removed in the calculation is studied in more detail later.

As expected for both SE and ME a correlation between ρ and the multiplicity is observed. Larger multiplicities result in a larger background energy density. However, a difference between SE and ME is observed for all multiplicities. Some entries at low ρ are observed for the SE which are not calculated within the ME. In particular at lower multiplicities entries below $\rho = 90$ GeV/(c sr) are observed which are not present in the ME.

It turns out that the events which produced the relatively small ρ in the SE are pileup events as described in section 4.3. Since these are very few events they are not reproduced in the ME because only one track is used from each SE. After the pileup rejection as described in 4.3 the low ρ entries disappeared. The projections of the distributions in figure 6.7 to the y-axis are shown in figure 6.8 in the left panel. The SE ρ distribution where $N_\mathrm{jet}^\mathrm{removed} = 3$ is depicted in blue and the ME ρ distribution with $N_\mathrm{jet}^\mathrm{removed} = 0$ in red. In the SE the low $\rho = 90$ GeV/(c sr) entries are observed. They are rejected after the pileup cut to the TOF hits is applied as shown in the right panel of figure 6.8.

However, in both cases the overall shapes of the SE and ME ρ distributions are similar but small deviations are visible. The ME ρ distribution is narrower than the distribution for the SE. In addition a shift between the two curves is observed

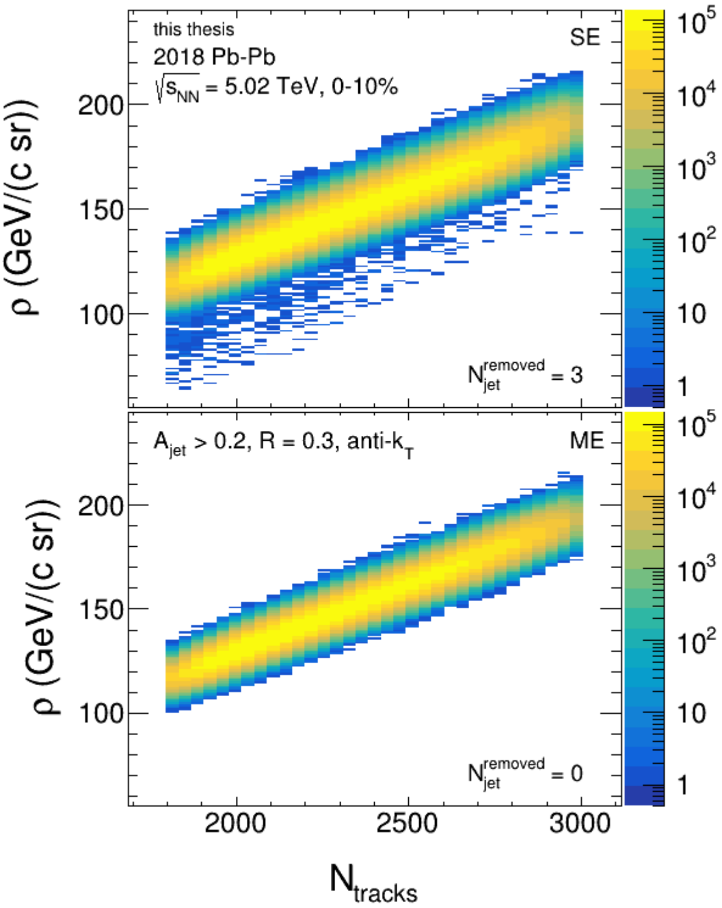

Figure 6.7.: Distributions of the background energy density ρ of SE (upper) and ME (lower) in dependence of the track multiplicity N_{tracks}. Three hardest jets are removed in the SE ρ calculation and zero in the ME. For the background reconstruction the k_T algorithm with $R_{\text{bckg}} = 0.3$ was used. The cuts of N_{tracks} at 1800 and 3000 arise due to the splitting of the events into different multiplicity bins.

which might be a result of the different number of removed jets and will be studied in more detail in the following.

In general is is not stated that the SE and ME ρ distributions have to be equal. Additional correlations in the SE which are destroyed in the ME, as already described in 5.3, might be the reason for some deviations. It is shown later that the presence of correlations broaden the distributions. This is studied in more detail in sections 6.4.1 and 6.6. In addition the setup which is used for the calculation of ρ is only one choice. Different jet algorithms and jet radii might lead to different results. However in [45] a difference between the ρ distributions of SE and ME in central collisions smaller than 60 MeV/c was observed.

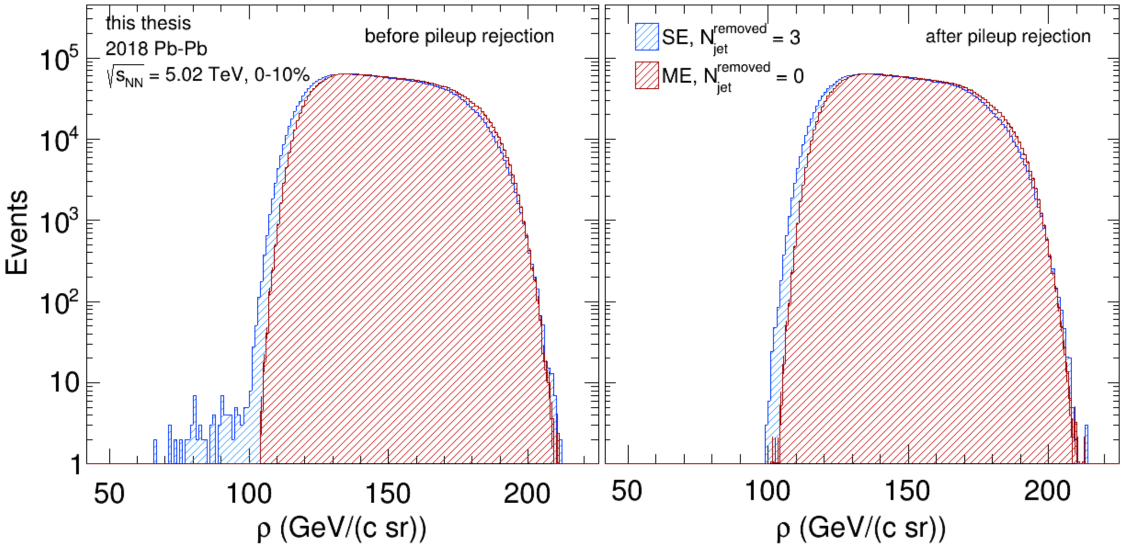

Figure 6.8.: Distributions of the background energy density ρ calculated with the k_{T} algorithm with $R_{\mathrm{bckg}} = 0.3$ for SE (blue) and ME (red) before the pileup events are rejected (left panel) and after the rejection (right panel). Three hardest jets are removed in the SE ρ calculation $N_{\mathrm{jet}}^{\mathrm{removed}} = 3$ and $N_{\mathrm{jet}}^{\mathrm{removed}} = 0$ in the ME.

6.3.1. Variations of removed jets in the ρ calculation

In this section the ρ distributions of the SE and ME are studied in more detail. In the following the ρ distributions as well as the raw jet distributions are compared for different numbers of removed jets.

Figure 6.9 depicts the ρ distributions for the SE where one (blue), two (green) and three (black) hardest jets are removed in the calculation and the ME ρ distribution with three (orange) and without removed jets (red). A subset of 10% of the data set was used, with one event plane bin (-90 to $-72°$) and all 10 multiplicity and 4 z-vertex bins.

Only small differences of at maximum 1 GeV/(c sr) between the three different SE ρ distributions are found. The more jets are removed in the ρ calculation the more the distribution is shifted to lower values as expected. As already described above, the deviation between ME and SE is larger. The same behavior between the SE and ME distributions is observed independent of the number of removed jets. The ME distribution is narrower than the SE distributions and in addition a small shift is observed. The ME ρ distribution is larger than the SE ρ distribution between 175 and 195 GeV/(c sr). The deviation is slightly smaller if less jets are removed in the SE. Therefore the number of removed jets in the ME is varied too. The orange curve represents the ρ distribution for the ME where three jets are removed. The deviations between 175 and 195 GeV/(c sr) between SE and ME vanish in this case. However, the ME distribution is still narrower. By removing three jets in the ME ρ calculation the whole distribution is shifted to lower values. At the lower edge a difference of about 1 GeV/(c sr) is still visible between SE and ME. The difference at the upper edge gets larger because the width stays the same in comparison to the

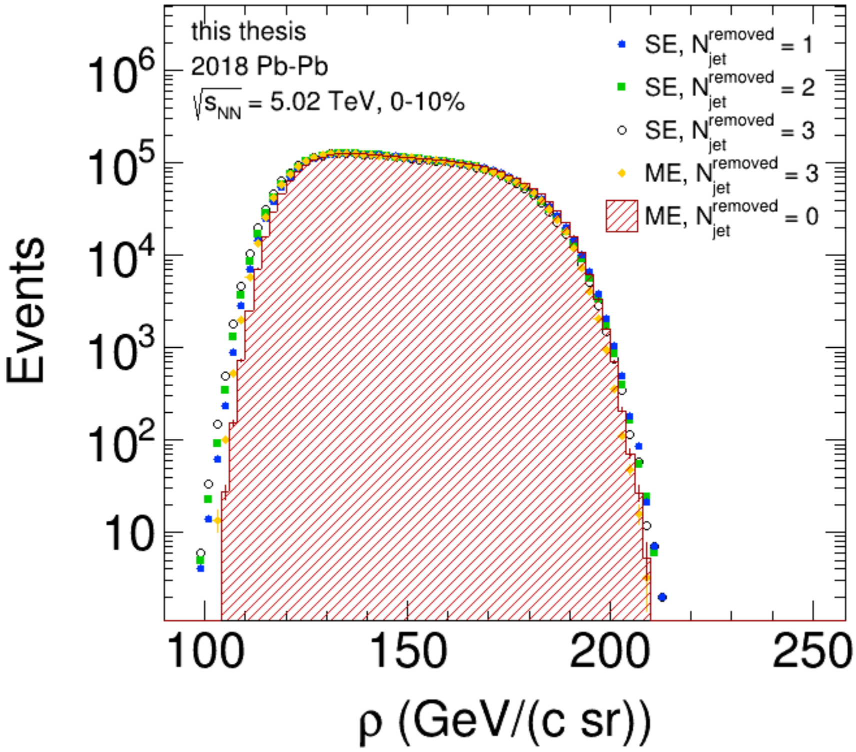

Figure 6.9.: Distribution of the background energy density ρ calculated with the k_{T} algorithm with $R_{\mathrm{bckg}} = 0.3$ for SE with 1 (blue), 2 (green) and 3 (black) hardest jets removed and ME with 0 (red) and 3 (orange) jets removed in the calculation.

ME where zero jets are removed.

For additional studies the ρ distributions of different multiplicity and event plane bins are compared. The shape of the distributions and the deviations between SE and ME are visible within all bins. Just the amount of the overall ρ is shifted between the different multiplicity bins. As expected the largest values are obtained for the largest multiplicity bin, as shown in figure 6.7.

By construction no jet correlations are expected in the ME and thus it should not be necessary to remove jets in the ρ calculation. But it is possible that the ρ of the SE and ME are not aligned due to other effects as the particle flow. As already described in [45] the ME and SE ρ distributions can be aligned by an additional shift since the choice of the reconstruction algorithm and its setup are not unique. However, the width of the SE and ME ρ distribution is expected to be equal. It turns out that the deviation in the width of the two distributions arises due to p_{T} fluctuations within the events. This was found at a later stage of the studies and is described in section 6.6.

In the following the effect of the ρ variations on the jet distributions are presented. For this, the raw correlated jet distributions are compared, as shown in figure 6.10.

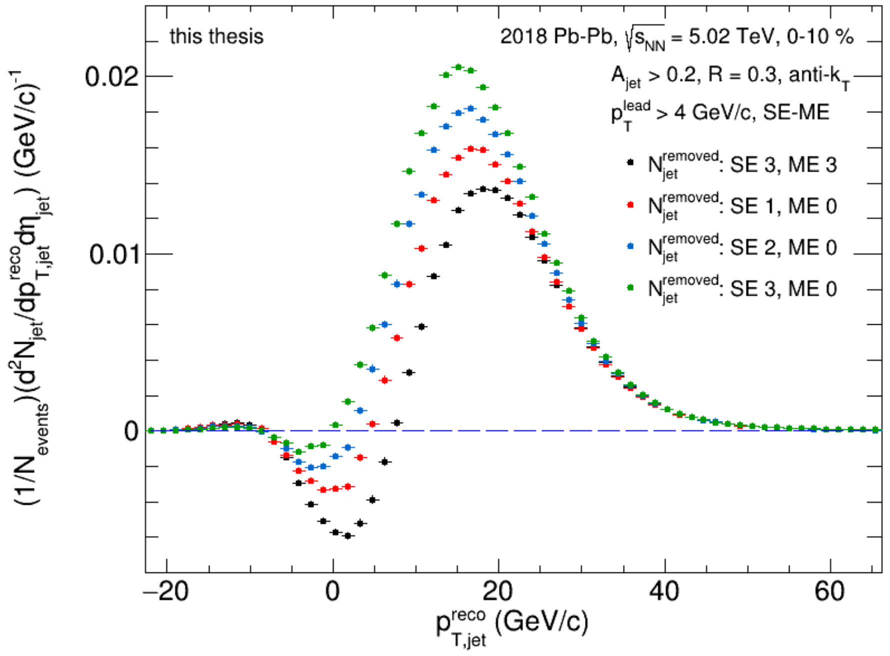

Figure 6.10.: Raw correlated quasi-inclusive jet distribution (SE-ME) with a bias of $p_{\mathrm{T}}^{\mathrm{lead}} > 4$ GeV/c. For the ρ calculation three jets are removed in the SE and ME (black), one (red), two (blue) and three (green) in the SE and zero in the ME. The distributions are normalized to the number of events N_{events}.

The calculated signal of the SE, where the contribution from uncorrelated background is subtracted by the ME, as function of $p_{\mathrm{T,jet}}^{\mathrm{reco}}$ are depicted. A small bias of 4 GeV/c was applied to the leading tracks for the jet selection in the SE and ME jet distributions.

The best alignment between the ρ distributions of SE and ME was found by removing three jets for both ρ calculations. This shifts the ME jet distribution of $p_{\mathrm{T,jet}}^{\mathrm{reco}}$ towards larger values which results in a larger difference between SE and ME at $p_{\mathrm{T,jet}}^{\mathrm{reco}} < 0$ GeV/c. This larger difference is observed in figure 6.10 too, where a deviation from zero of about 25% of the signal is observed around $p_{\mathrm{T,jet}}^{\mathrm{reco}} = 1$ GeV/c. As soon as zero jets are removed in the ME ρ calculation the description of the uncorrelated background in the SE gets better. The more jets are removed in the SE calculation the closer the difference SE-ME gets to zero at $p_{\mathrm{T,jet}}^{\mathrm{reco}} < 0$ GeV/c. The best result is obtained by removing three jets in the SE and zero in the ME (green). The mean value of the signal is shifted towards lower values if more jets are removed in the SE as expected. By removing one, two and three jets in the SE the peak of the $p_{\mathrm{T,jet}}^{\mathrm{reco}}$ distribution is shifted by steps of 1 GeV/c from 18 to 16 GeV/c.

However, the alignment between the ρ distributions of SE and ME becomes worse as more jets are removed in the SE and less in the ME. As the shift is explained by the number of removed jets, this does not explain the difference in the width of the distribution. As already mentioned above, the solution was found in section 6.6, where p_{T} fluctuations are studied.

In addition, the background is dominated by particles from the bulk which are influenced by the collective flow. The anisotropic track distribution due to the elliptic flow component leads to differences in the track density in and out of the reaction plane. This could influence the ρ distributions for SE and ME too, if the correlations due to flow are not exactly reproduced in the ME. The event plane dependence of the ME is studied in detail in the next section.

In the following a value of three removed jets in the SE is applied as default value and zero in the ME because the best description of the uncorrelated background in the SE by the ME could be obtained with this setup.

6.4. Systematic study of different event categories

In this section the mixed event distributions are studied in dependence of different event categories. As described in 5.3.1 the data set is split into 400 different categories in order to do the mixing only among events with equal centrality, event plane angle and z-vertex position. Without using the different categories for the mixing the description of the uncorrelated background in the SE becomes worse, as observed in figure 5.7.

In the following, the dependence of the ME on the event plane, the multiplicity and the z-vertex is studied in more detail. Different categories are studied and in addition smaller event plane and z-vertex bins are used for the mixing. The aim is to further improve the uncorrelated background description by the ME by dividing the events into more categories for the mixing. Because of different amounts of events within the categories, all raw jet distributions are normalized to the number of events used in the jet reconstruction. In addition, the ratio of produced mixed events to the same events used for the jet analysis might be different. In order to avoid deviations in the final jet distribution where the SE and ME from different categories are merged, each individual ME distribution is normalized to the corresponding SE distribution before the merging is done. The distributions are normalized by their integrals over the full range.

6.4.1. Event plane dependence of the mixed event

In this section the dependence of the uncorrelated background on the event plane is studied. Correlations of particles due to flow are of great significance, as the background particles in jet measurements are mainly particles from the bulk. The largest contribution arises due to the elliptic flow and will be studied in the following. Due to the elliptic flow, the particles are not distributed uniformly over the full $\eta-\phi$ range because the elliptic flow induces an anisotropic distribution as described in section 1.3.1. In order to describe the uncorrelated background with the mixed events, these anisotropies have to be taken into account in the ME production which was realized by the binning of the events according to the different event plane angles.

In order to study the effect of the flow on the reconstructed jet p_{T}, its dependence is studied in the SE first, followed by the dependence of the ME on the event plane angle.

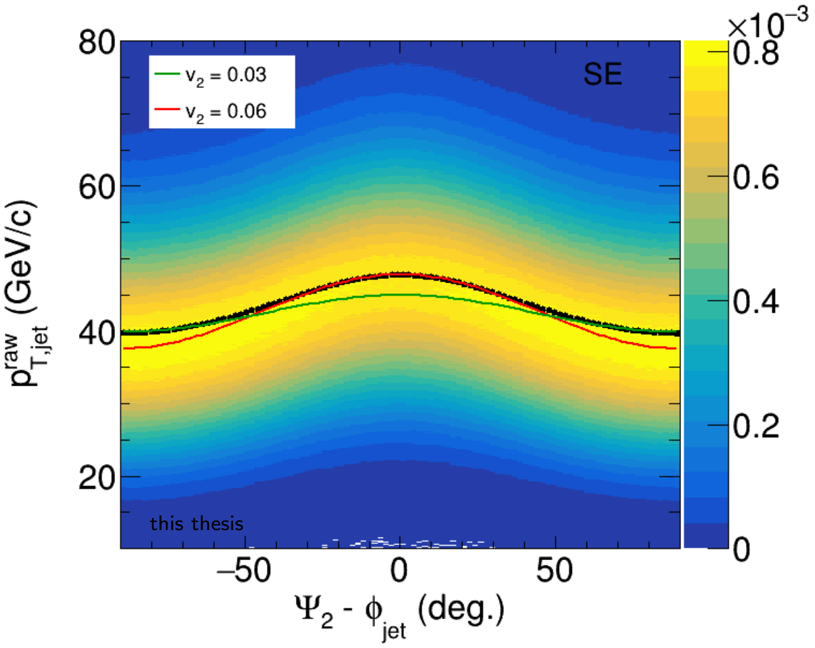

Figure 6.11.: Raw inclusive jet p_{T} of all reconstructed jets in the SE (y-axis) in dependence of the event plane angle minus the jet angle $\Psi_2 - \phi_{\mathrm{jet}}$ (x-axis). The mean jet energy $p^{\mathrm{raw}}_{\mathrm{T,jet}}$ calculated from the data is shown in black and the estimations with $v_2 = 0.03$ and 0.06 in green and red. Details of the calculation are described in the text.

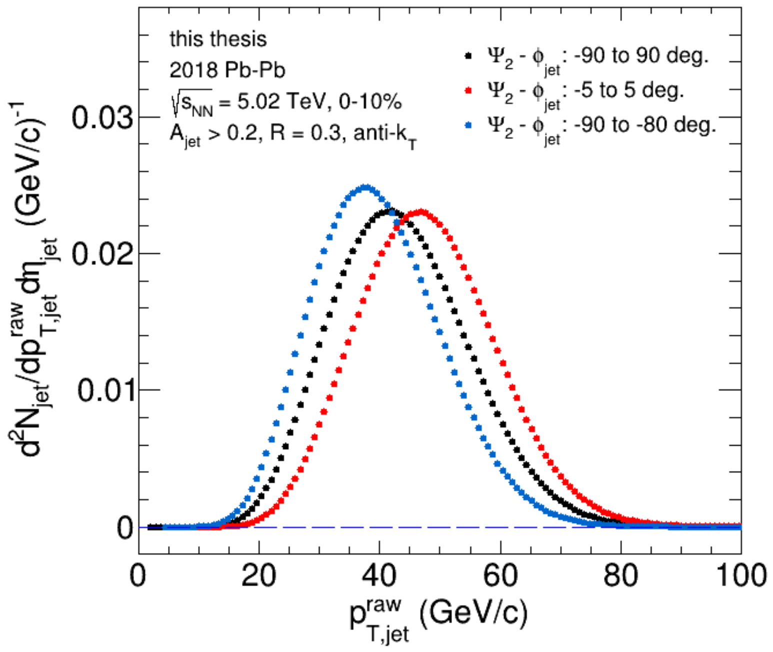

Figure 6.12.: Projection of figure 6.11 to the y-axis for different angles of $\Psi_2 - \phi_{\mathrm{jet}}$: $-90°$ to $90°$ (black), $-5°$ to $5°$ (red) and $-90°$ to $-80°$ (blue). The distributions are normalized by their integrals over the full $p^{\mathrm{raw}}_{\mathrm{T,jet}}$ range.

Figure 6.11 depicts the raw reconstructed jet $p_{\mathrm{T,jet}}^{\mathrm{raw}}$ of real events, before the subtraction of the background ρ is done, in dependence of the difference between the event plane angle and the jet angle $\Psi_2 - \phi_{\mathrm{jet}}$. For the jet reconstruction the default setup with a jet radius of $R = 0.3$ was used. A strong correlation between the jet energy and the event plane is observed. A maximum of the jet energy is reached if the jet was measured in the direction of the event plane and a minimum if the jet goes out of the event plane at $\Psi_2 - \phi_{\mathrm{jet}} = \pm 90^\circ$. A difference of about $p_{\mathrm{T,jet}}^{\mathrm{raw}} = 10$ GeV/c is observed between 0 and 90°.

For an estimation of the background energy density in dependence of the flow the formula for the particle yield as given by equation 6.2 can be exploited.

$$\frac{dN}{d\phi} \propto \left(1 + 2v_2 \cos(2(\Psi_2 - \phi))\right) \tag{6.2}$$

As approximation for the elliptic flow a value measured for the pions in Pb+Pb collisions at $\sqrt{s_{\mathrm{NN}}} = 5.02$ TeV is used. At a transverse momentum of 1 GeV/c and a centrality of 5-10% a v_2 of about 0.06 was measured in [81]. After the calculation of $dN/d\phi$ according to equation 6.2, the result is scaled by the mean background energy density ρ times the jet area $A_{\mathrm{jet}} = \pi R^2$, where R is the jet radius. An approximation of the mean background energy density in dependence of $\Psi_2 - \phi_{\mathrm{jet}}$ is obtained. A mean value of $\rho = 150$ GeV/(c sr) and a jet radius of $R = 0.3$ are used.

The result is shown in figure 6.11 depicted in red. A very good approximation of the mean jet energy $p_{\mathrm{T,jet}}^{\mathrm{raw}}$, which is represented by the black curve, is obtained. In addition, a smaller v_2 value of 0.03 was used (green) which results in a more precise description at larger $\Psi_2 - \phi_{\mathrm{jet}}$. In general it becomes clear that the elliptic flow has a large impact on the uncorrelated background in jet measurements. This event plane dependence has to be considered in the ME.

The projections for different bins of $\Psi_2 - \phi_{\mathrm{jet}}$ to the y-axis ($p_{\mathrm{T,jet}}^{\mathrm{raw}}$) are shown in figure 6.12. The raw jet p_{T} distributions are compared for angles of $\Psi_2 - \phi_{\mathrm{jet}}$ from -90° to 90° (black), -5° to 5° (red) and -90° to -80° (blue). The distributions are normalized by their integrals. In addition to the shift of the mean jet p_{T} the distribution for the -90° to -80° bin is narrower in comparison to the central bin from -5° to 5°. The reason for this is the larger variation of the raw jet p_{T} in the central bin in comparison to the outer $\Psi_2 - \phi_{\mathrm{jet}}$ bin. This strong dependence of the jet energy on the event plane angle could have a large influence on the produced mixed events which is studied in the following.

Because it is not possible to reconstruct the event plane and the track distribution of the SE by the ME on an event-by-event basis, as already discussed in 5.3.2, small differences in the event plane could lead to differences in the reconstructed jet energy. For the mixing it is possible that events which differ 18° in the event plane are used because the events are separated into 10 event plane bins. Within one event plane bin, for example between 0° and 18°, is still a difference of about 2 GeV/c in the reconstructed jet p_{T} in the SE.

For the verification of the need of the event plane bins as described above, the difference in the reconstructed jet distribution of the ME without event plane bins and with 18° bins is shown in figure 6.13. For the jet reconstruction only a small subset of the data is used with one multiplicity (bin 4, 2210-2297) and one z-vertex (bin 2, 0-4 cm) bin. In the upper panel of figure 6.13 the inclusive jet distributions of SE and ME are depicted. The inclusive jet distribution is used because the effect of the event plane is more clearly visible due to the larger statistics. The same behavior as described below is observed for the biased jet distribution. The spectra are again normalized to the number of events and the ME distributions are normalized to the SE in the region up to -5 GeV/c. The SE distribution is depicted in black and the ME distributions with 18° bins in blue and without event plane bins in red. Only one SE jet distribution is shown because it does not depend on the number of used event plane bins for the mixing.

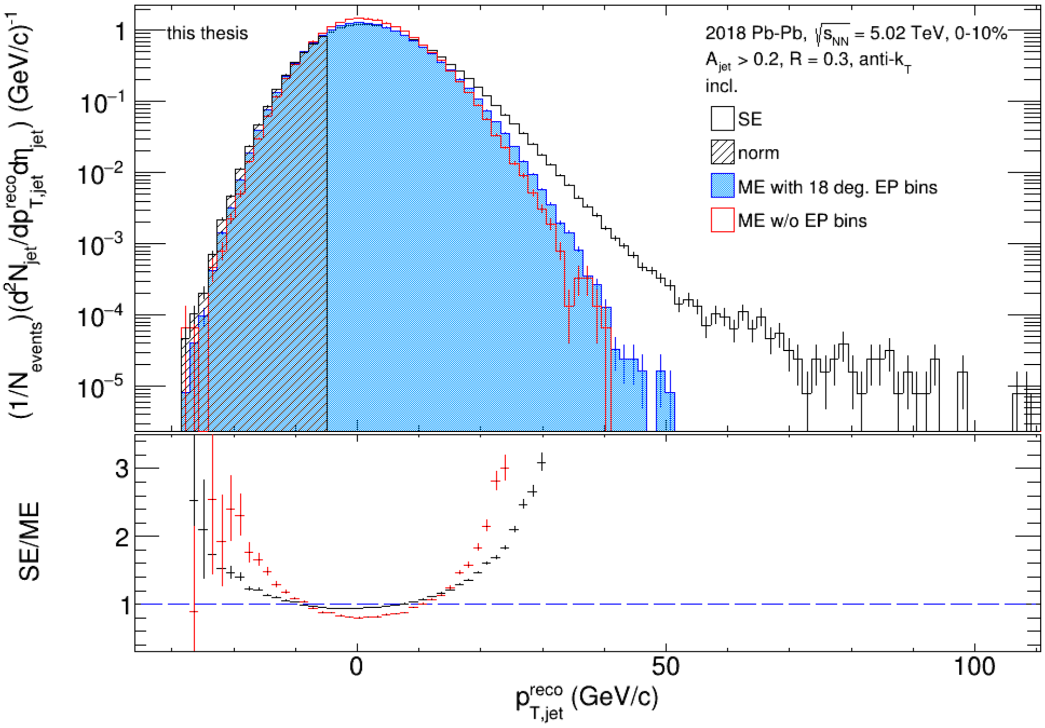

Figure 6.13.: Raw inclusive jet distribution of all reconstructed jets of the SE (black) and ME with 18° EP bins (blue) and ME without EP bins (red). The range for the normalization of ME to SE is indicated by the shaded region. Lower panel: Ratios SE/ME with 18° bins (black) and without EP bins (red). A subset of the data with one multiplicity bin (bin 4, 2210-2297) and z-vertex bin (bin 2, 0-4 cm) was used.

A large impact of the event plane bins on the ME jet population is visible. The uncorrelated background in the SE is not described very well if the mixing is done without the separation of the events into event plane bins. A large improvement of the description is observed if the 18° bins are used for the mixing. The effect of the large impact of the event plane bins is clearly visible in the ratio SE/ME in the lower panel of figure 6.13 too. Without event plane bins the SE/ME ratio deviates strongly from one. Around 0 GeV/c the ME exceeds the SE distribution. A deviation of 20% from one is observed if no event plane bins are used. This is reduced to about 7% if the event plane bins are used in the mixing. A similar behavior is observed between -10 and -20 Gev/c where the deviation is about twice as large if no event plane bins are used in comparison to the 18° bins.

The reason is the effect of the flow on the reconstructed jet energy as described above. Without event plane bins in the mixing procedure, tracks from events of all event plane angles are used. This results in a uniformly distribution of the tracks over the full acceptance. As consequence only some mean p_{T} for the jets is calculated in the jet reconstruction because the in and out of plane structure of the events with large and small track densities is lost. The result is a narrower ME distribution without the small and large jet p_{T} as it is observed for the SE.

Since there is still a small difference between the SE and ME on the left side tail if 18° bins are used it is obvious to try smaller event plane bins which should broaden the ME even more. As a solution one could use a finer binning of the event plane angle in the splitting of the events as described in 5.3. In practice this is not useful because the number of categories would become too large. Instead of changing the splitting procedure, an internal separation into smaller bins is done. In order to do this a sub event plane bin is calculated for every event plane bin of the events and the mixing is done only among events of the same sub bin. However, more events are required in order to produce mixed events. The minimum number of the upper edge of the multiplicity bins of the categories is now also required for each sub event plane bin in order to start the mixing and produce mixed events. The further splitting into three degree bins is possible with the available statistics. The result of the reconstructed jet distributions with 3° event plane bins is shown in the appendix A.3.

However, it turns out that no further improvement of the description of the uncorrelated background in the SE by the ME could be obtained by smaller event plane bins. The reason is the limited event plane resolution of about 13° as described in section 5.2. If more event plane bins are used for the mixing the description of the SE by the ME is limited by the event plane resolution.

In order to find this limit in the ME the dependence of the mixed events on the number of event plane bins is studied in more detail. From this study a correction for the ME could be estimated. This is done by analyzing the width of the ME distribution in dependence of the number of event plane bins. As a saturation of this distribution is expected around 15°, a correction could be estimated by predicting the width of the ME if infinitely small event plane bins could be used without a limiting resolution.

The inclusive jet distributions for SE and ME are determined, where 0, 2, 4, 6, 10, 20 and 60 event plane bins are used for the mixing. Again a subset of the full data set with one multiplicity (bin 4, 2210-2297) and z-vertex (bin 2, 0-4 cm) bin is used. The resulting ratios of the SE and ME jet distributions are depicted in figure 6.14. As already observed in figure 6.13 the ME distribution becomes smaller if the flow is not considered in the mixing. This results in a larger offset in the negative direction around $p_{\mathrm{T,jet}}^{\mathrm{reco}} = 0$ GeV/c and a larger offset from one in positive direction for higher and lower jet $p_{\mathrm{T,jet}}^{\mathrm{reco}}$. A clear improvement is observed if the event plane is divided in two bins of 90° and the description gets even better if four 45° bins are used in the mixing. By further splitting the event plane into 6 or 10 or even more bins only smaller differences are visible.

Due to the event plane resolution $\Delta\Psi_2 \approx 13°$, which was calculated in section

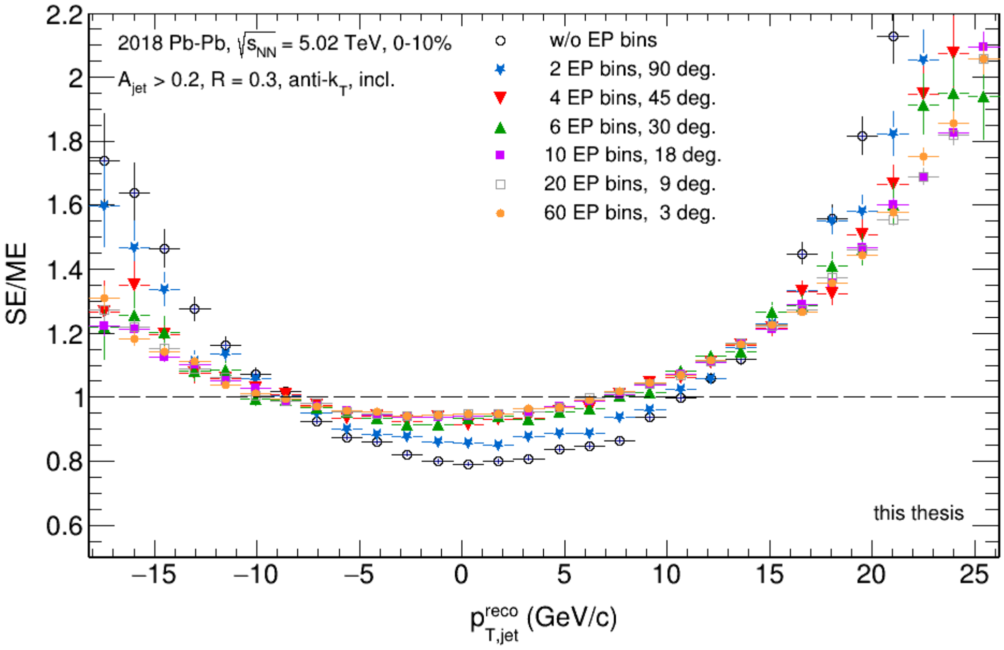

Figure 6.14.: Ratio of the raw inclusive jet distributions of SE and ME in dependence of $p_{\mathrm{T,jet}}^{\mathrm{reco}}$. For the mixed event various number of event plane bins are used. The same setup for the reconstruction and normalization as in figure 6.13 is used.

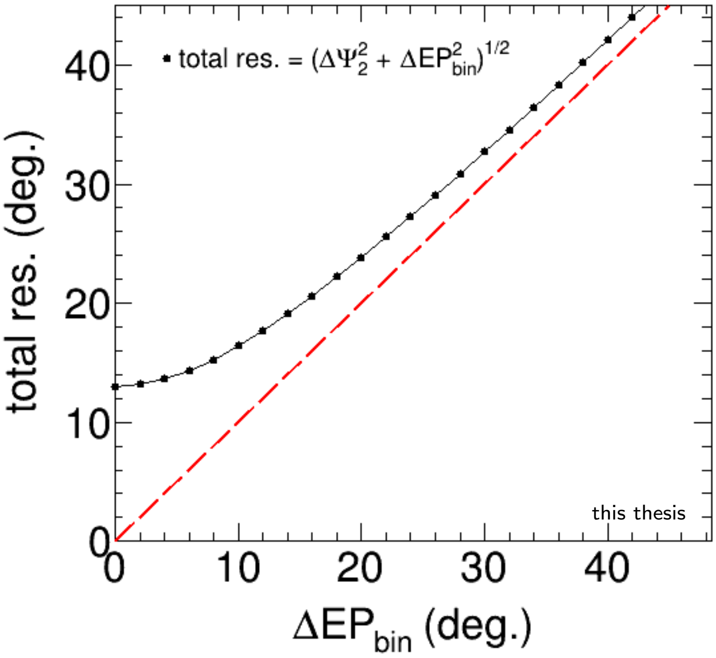

Figure 6.15.: Total resolution in dependence of the event plane bin size $\Delta\mathrm{EP}_{\mathrm{bin}}$ (black). The red dashed line indicates the case where the contribution of $\Delta\Psi_2$ to the total resolution is negligible.

5.2, a limit of the broadening of the ME distribution is expected at the latest at 10 event plane bins of 18°.

In figure 6.15 the total resolution in dependence of the angle of one event plane bin $\Delta\mathrm{EP}_{\mathrm{bin}}$ is shown. The total resolution is calculated as the square root of the sum of the event plane resolution $(\Delta\Psi_2)^2$ and event plane bin angle $(\Delta\mathrm{EP}_{\mathrm{bin}})^2$. While for $20° < \Delta\mathrm{EP}_{\mathrm{bin}} < 45°$ an almost linear improvement in the total resolution is observed, the improvement gets smaller for smaller $\Delta\mathrm{EP}_{\mathrm{bin}}$. The difference in the total resolution is only 4°, if 1° event plane bins are used instead of 15° bins. Due to the limiting event plane resolution, no further broadening of the ME distribution is observed if more than 10 event plane bins are used in the mixing. In this range, where the contribution from the event plane resolution is dominating the total resolution, the ratios SE/ME become equal, as observed in figure 6.14. As already mentioned above, the width of the ME distribution in dependence of the used event plane bins can be estimated. This can be used to predict the width at very small $\Delta\mathrm{EP}_{\mathrm{bin}}$ for the case, where no limiting event plane resolution exists. In further studies this can be implemented as an analytical correction to the ME distribution.

6.4.2. Multiplicity dependence

In this section the multiplicity dependence of the reconstructed jet distribution is studied. Figure 6.16 shows the raw jet $p_{\mathrm{T,jet}}^{\mathrm{raw}}$ in dependence of the track multiplicity N_{track} of the same events. No cuts on the raw jet p_{T} are applied and the inclusive jet distribution is used with the same setup for the jet reconstruction as in the previous section. The mean $p_{\mathrm{T,jet}}^{\mathrm{raw}}$ is indicated by the black line. It depends on the multiplicity and gets larger with increasing multiplicity. At the smallest multiplicity a mean value of $p_{\mathrm{T,jet}}^{\mathrm{raw}} = 34$ GeV/c is reconstructed which increases up to $p_{\mathrm{T,jet}}^{\mathrm{raw}} = 56$ GeV/c for the largest multiplicity. This dependence is expected as the track density gets larger with increasing multiplicity and more background tracks are within the jet radius in the clustering.

The projection of figure 6.16 to the y-axis for different bins of the multiplicity is shown in figure 6.17. The projection for the full multiplicity range is shown in black, the red curve represents the projection for the smallest multiplicity bin (1800-1962) and the blue curve for the largest multiplicity bin (2722-2986). The distributions are normalized by the number of events of the different multiplicity bins. As described above, the dependence of the mean value of $p_{\mathrm{T,jet}}^{\mathrm{raw}}$ on the multiplicity is observed. In addition the width of the distributions depend on the track multiplicity. For smaller multiplicities the width gets smaller and it increases for larger multiplicities. The broadest distribution is obtained for the full range of N_{track}.

In figure 6.18 the jet distributions of SE and ME are shown for two different multiplicity bins. The reconstructed jet $p_{\mathrm{T,jet}}^{\mathrm{reco}} = p_{\mathrm{T,jet}}^{\mathrm{raw}} - \rho A_{\mathrm{jet}}$ distributions are shown where a 4 GeV/c bias on the leading tracks was applied. In both cases only one z-vertex bin (bin 2, 0-4 cm) and one event plane bin (bin 5, 0-18°) are used. In the upper plot the data from the smallest multiplicity bin was used while in comparison to that the largest multiplicity bin was used in the lower plot.

By subtracting the event-to-event background energy density ρ, the mean p_{T} of the jet distributions is shifted to the same value. Independent of the multiplicity

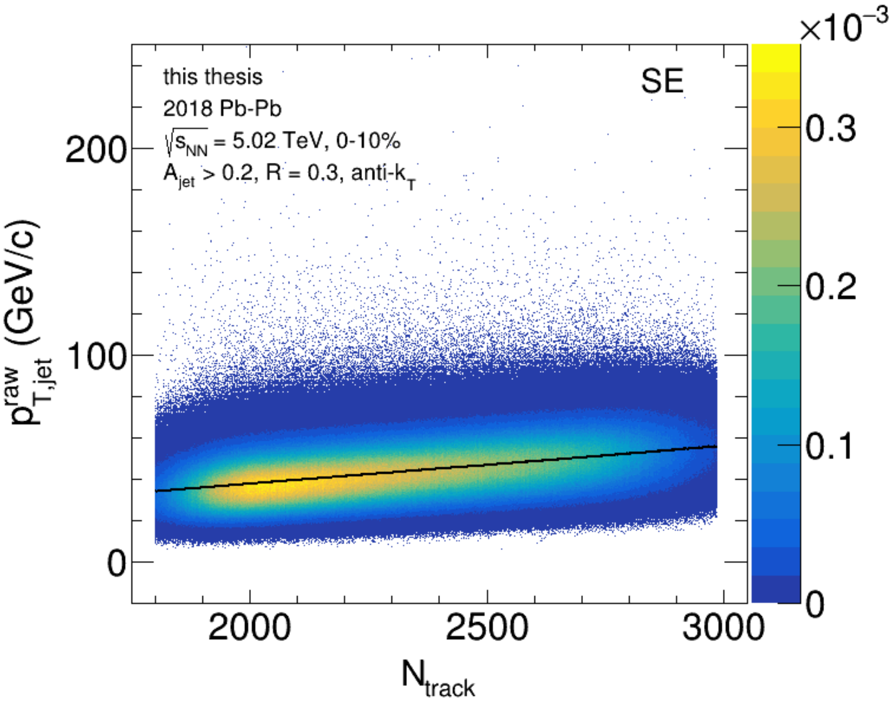

Figure 6.16.: Raw jet p_T ($p^{\text{raw}}_{\text{T,jet}}$) distribution in dependence of the track multiplicity N_{track} in the SE.

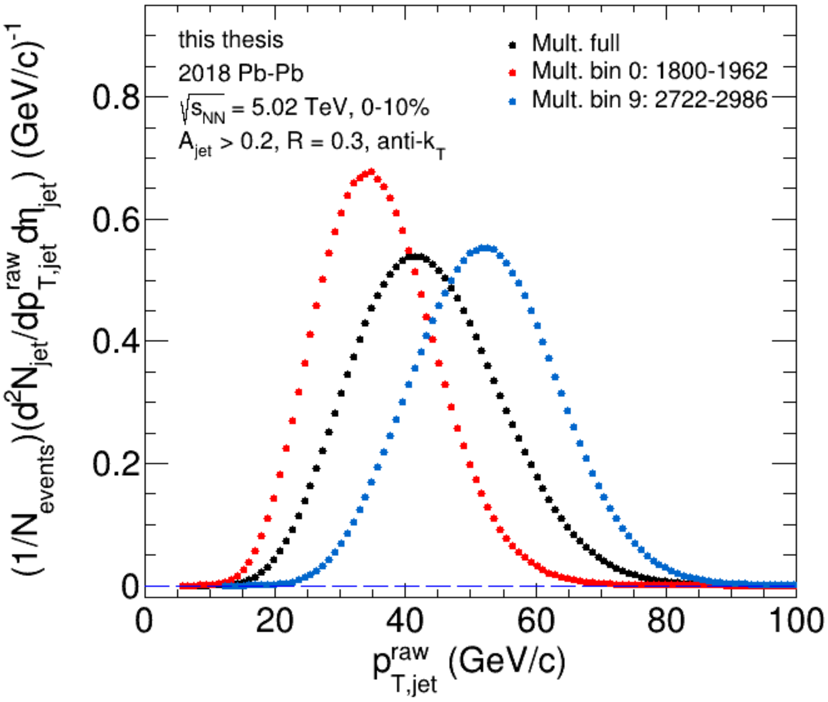

Figure 6.17.: Projection of figure 6.16 to the y-axis for different multiplicities: Full range (black), lowest multiplicity bin 1800-1962 (red) highest multiplicity bin 2722-2986 (blue). The distributions are normalized by the number of events of the different multiplicity bins.

bin they are centered around 4 GeV/c. This follows from the ρ dependence on the multiplicity as observed in 6.3.

In addition, the larger multiplicity leads again to a broader $p_{\mathrm{T,jet}}^{\mathrm{reco}}$ distribution of the jets. More jets are observed in the low $p_{\mathrm{T,jet}}^{\mathrm{reco}}$ region down to -30 GeV/c, while almost no entries are observed below -20 GeV/c for the smaller multiplicity. This was expected from the distribution shown above. In addition more jets are reconstructed at large $p_{\mathrm{T,jet}}^{\mathrm{reco}}$ as more high p_{T} particles are expected in an event with a larger multiplicity.

From this observation it becomes clear that a sampling from the SE multiplicity distribution for the ME is necessary. The SE distribution can not be described with a ME of only one multiplicity.

In the lower panels of figure 6.18, the ratios SE/ME for the two different multiplicity bins is shown. The ratio SE/ME is very close to one at $p_{\mathrm{T,jet}}^{\mathrm{reco}} < 0$ GeV/c, where only uncorrelated background is expected. Only small deviations of 1-2 sigma are observed in both distributions. By using the same multiplicities as in the SE and the event categorization a good description of the uncorrelated background in the SE by the ME can be obtained for all multiplicity bins. It is not necessary to split the events into smaller multiplicity bins, as the ME multiplicity is sampled from real data in any case.

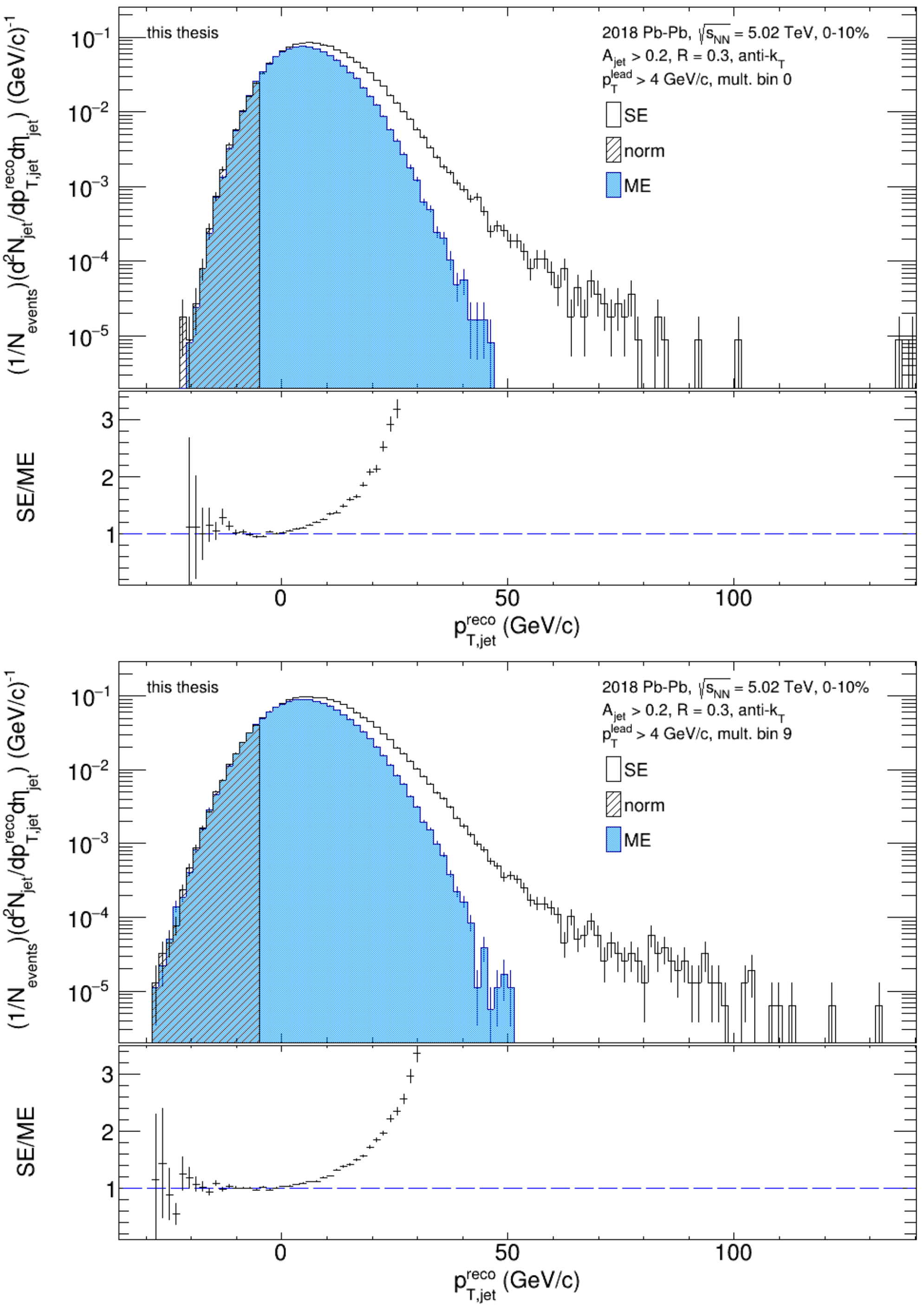

Figure 6.18.: Raw SE (black) and ME (blue) jet p_{T} distributions with a 4 GeV/c bias as function of $p_{\mathrm{T,jet}}^{\mathrm{reco}}$. The range for the normalization of ME to SE is indicated by the shaded region. The ratio SE/ME is depicted in the lower panel. For the ME production only events within one multiplicity bin are used. Upper plot: Mult. bin 0 (1800-1962). Lower plot: Mult. bin 9 (2722-2986). In both cases one z-vertex (bin 2, 0-4 cm) and one event plane bin (bin 5, 0-18°) is used.

6.4.3. Dependence of the mixing on the z-vertex

In section 4.2 the strong z-vertex dependence of the multiplicity was described. In order to test how this influences the production of the mixed events, different z-vertex bins and different bin sizes for the mixing are used.

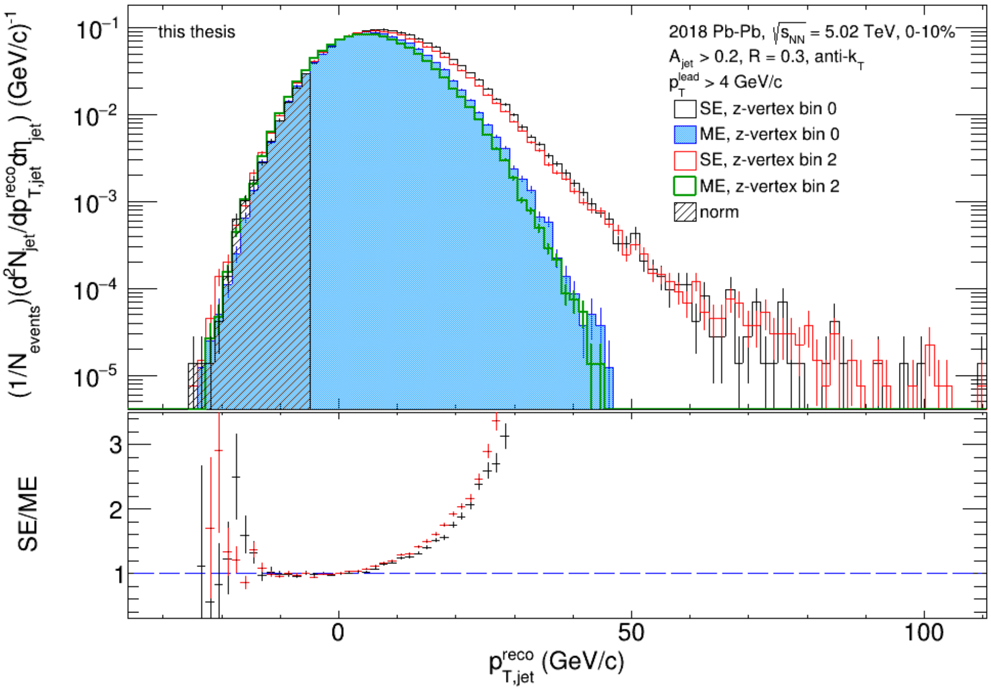

Figure 6.19.: Raw jet $p_{\mathrm{T,jet}}^{\mathrm{reco}}$ distributions with a 4 GeV/c cut on the leading track for SE (black) and ME (blue) with z-vertex bin 0 (-8 - -4 cm) and SE (red) and ME (green) with z-vertex bin 2 (0 - 4 cm). The range for the normalization of ME to SE is indicated by the shaded region. The ratio SE/ME is depicted in the lower panel for z-vertex bin 0 (black) and z-vertex bin 2 (red).

The jet distributions with different z-vertex bins are presented first. For this the multiplicity bin 4 (2210-2297) and the event plane bin 4 (-18-0°) are used. The results for the z-vertex bin 0 (-8 - -4 cm) and bin 2 (0 - 4 cm) are depicted in figure 6.19. The jet distributions of the SE for z-vertex bin 0 (black) and 2 (red) and the corresponding ME in blue (bin 0) and green (bin 2) with a 4 GeV/c cut on the leading tracks are shown. The setup for the jet reconstruction as described in previous sections is used.

At the right tail a shift of 1.5 GeV/c is observed between the two SE distributions. The distribution of z-vertex bin 2 is shifted to lower values. The same shift is observed between the ME distributions. However, the uncorrelated background in the SE is described very well by the ME in both cases. Only small deviations of 1-2 sigma are visible at the left side at $p_{\mathrm{T,jet}}^{\mathrm{reco}} < -12$ GeV/c in the lower panel, where the ratios SE/ME are depicted. At $p_{\mathrm{T,jet}}^{\mathrm{reco}} > 0$ GeV/c the ratio gets larger for the z-vertex bin 2 in comparison to z-vertex bin 0. Due to the deviations between the jet distributions of events with different z-vertices, the separation of the events into different z-vertex bins was necessary in order to obtain a reasonable ME. The description of the uncorrelated background of the SE by the ME works very well independent of the z-vertex.

As described in section 5.3, 4 z-vertex bins each of 4 cm are used in the splitting of the TTrees as default value. In the following smaller z-vertex bins of 1 cm are tried for the mixing. This is done by an internal separation of the events into sub z-vertex bins as it is done for smaller event plane bins, which was described in the previous section. In total 16 z-vertex bins are used, each of 1 cm. For this study the whole data set was used.

In figure 6.20 the obtained raw correlated jet distributions where the uncorrelated background was removed by subtracting the ME are presented. The corresponding raw uncorrelated jet distributions of SE and ME are shown in the appendix A.4. In particular the same setup for the jet reconstruction and the 4 GeV/c bias as described in previous sections was applied. The distributions are shown with two different setups for the mixing. The standard 4 cm (black) z-vertex bins and the smaller 1 cm (red) z-vertex bins are used. In general no large differences between both distributions are visible. A small improvement of the description of the SE background by the ME is observed with the smaller z-vertex bins. Between -10 and 0 GeV/c the correlated jet distribution is slightly closer to zero if the 1 cm z-vertex bins are used. Around the maximum at $p_{\mathrm{T,jet}}^{\mathrm{reco}} = 15$ GeV/c the signal is about 10% larger for the 1 cm z-vertex bins in comparison to the 4 cm z-vertex bins. At larger jet p_{T} no differences are observed. Further studies can be done by using different bin sizes of the z-vertex. With the available statistics and the standard event plane bins of 18 degrees, z-vertex bins down to 0.25 cm can be used.

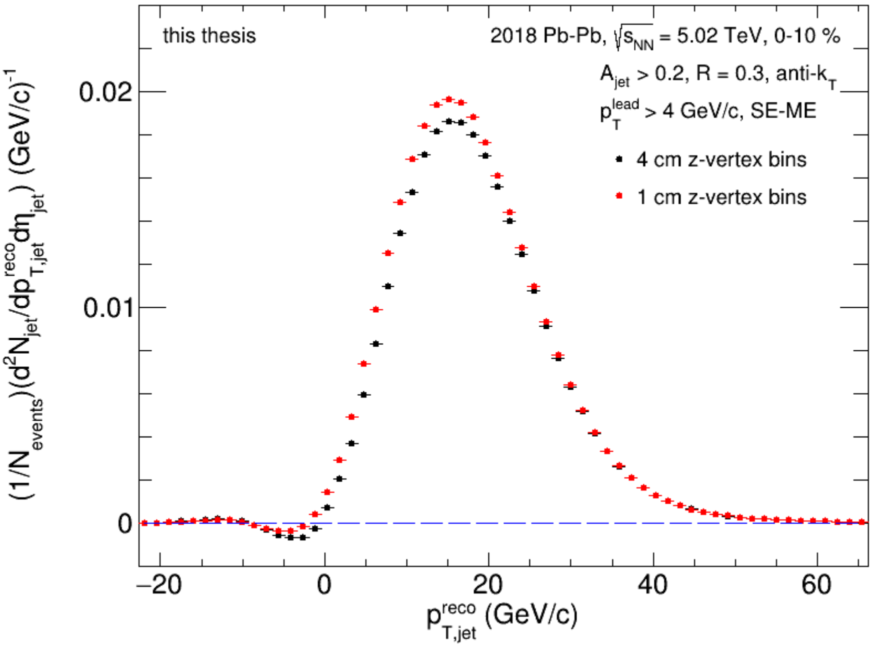

Figure 6.20.: Raw correlated quasi-inclusive jet distribution (SE-ME) with a bias of $p_{\mathrm{T}}^{\mathrm{lead}} > 4$ GeV/ where 4 cm z-vertex bins (black) and 1 cm z-vertex bins (red) are used for the mixing. The full data set was used and the distributions are normalized to the number of events N_{events}.

6.5. Run dependent observation

In this section a run dependent observation in the inclusive jet distribution is reported. Figure 6.21 depicts the SE and ME inclusive jet distributions for the full data set, normalized to the number of events N_{events}. All jet candidates which are reconstructed with the anti-k_{T} algorithm with a jet radius of $R = 0.3$ and with $A_{\text{jet}} > 0.2$ are accepted. In particular the whole data set with the first 90 runs from the LHC18q run list is used with the applied track selection as described in section 4.2. The SE jet distribution is depicted in black and the ME distribution in blue. The shaded region is the normalization region. In the lower panel the ratio SE/ME is presented. While the SE and ME are in good agreement between $-15 < p_{\text{T,jet}}^{\text{reco}} < 0$ GeV/c some objects at lower $p_{\text{T,jet}}^{\text{reco}}$ are reconstructed in the SE which are missing in the ME distribution.

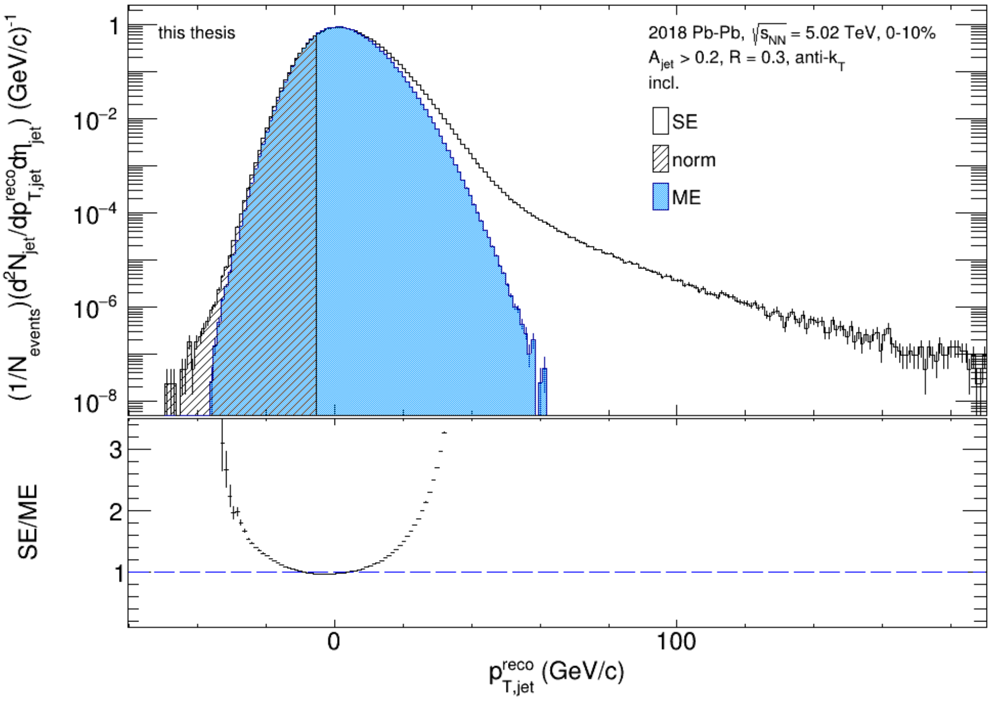

Figure 6.21.: Raw inclusive SE (black) and ME (blue) jet $p_{\text{T,jet}}^{\text{reco}}$ distributions for the full data set. The range for the normalization of ME to SE is indicated by the shaded region. The ratio SE/ME is depicted in the lower panel.

Although these are very few entries in the SE they are studied in more detail by investigating different properties of the jets with $p_{\text{T,jet}}^{\text{reco}} < -35$ GeV/c.

No abnormalities could be found in the area distributions of the jets or in the ρ distributions of the events. In addition other properties of the events as the TOF hits, TRD tracklets or multiplicities were checked. No difference in comparison to events without the low $p_{\text{T,jet}}^{\text{reco}}$ jets could be found. However, the jets with $p_{\text{T,jet}}^{\text{reco}} < -35$ GeV/c are found mainly at the positive η acceptance. The distribution of the jets with $p_{\text{T,jet}}^{\text{reco}} < -35$ GeV/c in η and ϕ is shown in the appendix A.2.

In figure 6.22 the jet distributions for positive (upper) and negative (lower) η are presented. Exactly the same setup and data is used as for figure 6.21 only the

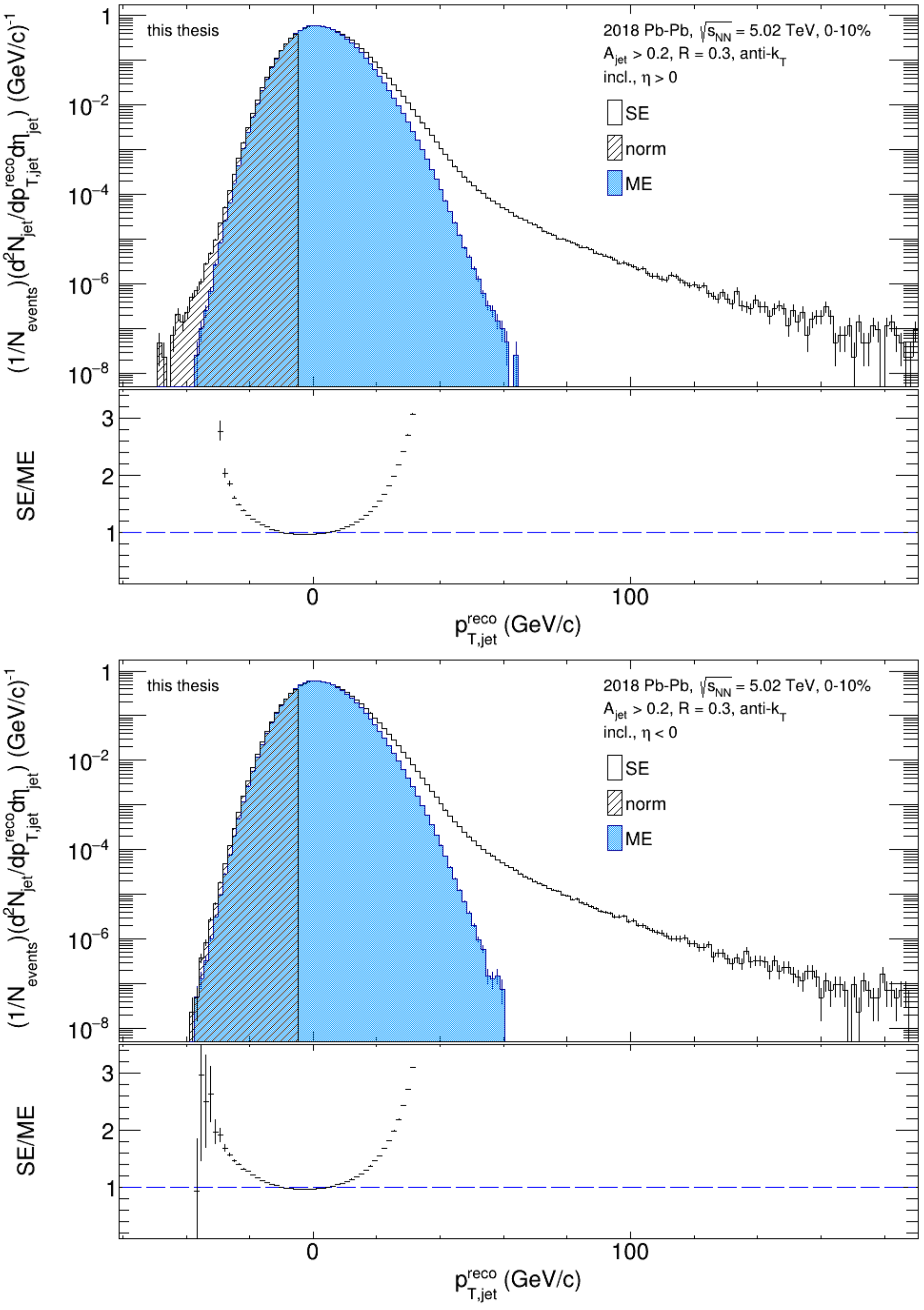

Figure 6.22.: Raw inclusive SE (black) and ME (blue) jet $p^{\mathrm{reco}}_{\mathrm{T,jet}}$ distributions with the same setup as used for figure 6.21, for positive η (upper plot) and negative η (lower plot). The range for the normalization of ME to SE is indicated by the shaded region. The ratio SE/ME is depicted in the lower panels.

splitting in the positive and negative η acceptance was added. All entries in the SE at low $p_{\mathrm{T,jet}}^{\mathrm{reco}}$, which were not described by the ME, are in the jet distribution with $\eta > 0$. They disappeared if only the negative η acceptance is used. This results in a good description of the SE by the ME at the left side tail.

In order to prevent the full exclusion of the positive η acceptance another possibility to reject the entries at the left side for the SE was searched. It turned out that the jets with $p_{\mathrm{T,jet}}^{\mathrm{reco}} < -35$ GeV/c are mainly within three particular runs. Figure 6.23 depicts the run IDs of the runs which contain the jets with $p_{\mathrm{T,jet}}^{\mathrm{reco}} < -35$ GeV/c labeled with $N_{\mathrm{jets,p_{T,jet}^{reco}<-35GeV/c}}$. The number of those jets are normalized by all jets which are reconstructed in the events of the particular run IDs. Three runs with the run IDs 296414, 296509 and 296621 could be identified and excluded from the analysis.

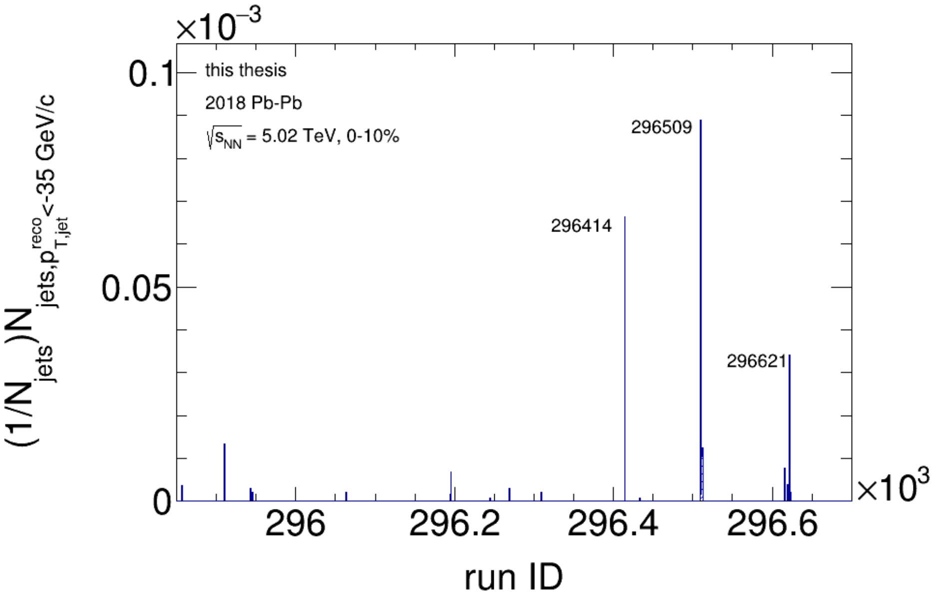

Figure 6.23.: Run IDs of the runs which contain the jets with $p_{\mathrm{T,jet}}^{\mathrm{reco}} < -35$ GeV/c ($N_{\mathrm{jets,p_{T,jet}^{reco}<-35GeV/c}}$). They are normalized by all jets which are reconstructed within the events of the particular run.

The resulting jet distribution where the three runs are excluded is shown in figure 6.24. Most of the entries in the SE at $p_{\mathrm{T,jet}}^{\mathrm{reco}} < -35$ GeV/c which were not described by the ME are rejected. Only very few entries around -40 GeV/c are left in the SE. The uncorrelated background in the SE is also well described now by the ME distribution but some deviations are still visible at the left side tail.

For the following analysis and results, in particular for the results presented in section 7, the three runs as described above are excluded. This results in a loss of 4% of the events.

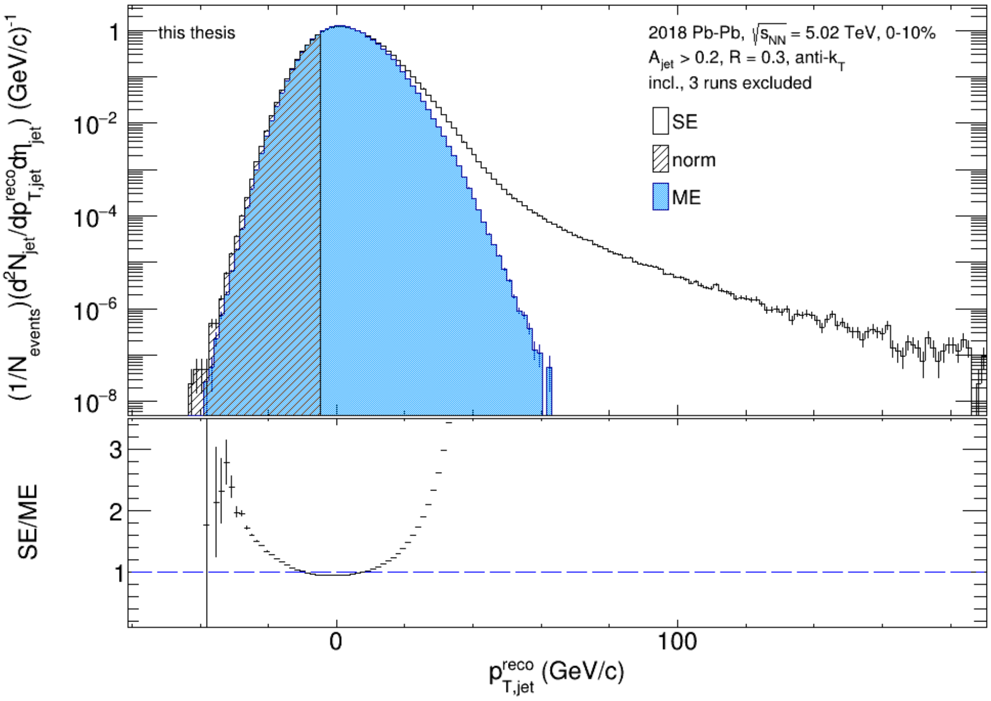

Figure 6.24.: Raw inclusive SE (black) and ME (blue) jet $p^{\mathrm{reco}}_{\mathrm{T,jet}}$ distributions with the same setup as used for figure 6.21, but the three identified runs, as described in the text, are excluded. The range for the normalization of ME to SE is indicated by the shaded region. The ratio SE/ME is depicted in the lower panel.

6.6. Event-by-event p_{T} fluctuations

Since a small difference between SE and ME is still observed in the jet distributions at the left side tail, where the ME should reproduce the uncorrelated background in the SE, further studies are carried out. Small deviations are observed in particular in the inclusive jet distribution and in addition differences in the ρ distributions of SE and ME were observed. In this section the event-by-event fluctuations of the transverse momentum of all particles generated in an event are studied.

In order to do this the sum of all transverse momenta of the particles within one event, which are used for the jet reconstruction in the SE and ME, is calculated. Before the data is shown, the expected distributions are studied in a simulation. It is expected that the ME $p_{\mathrm{T}}^{\mathrm{sum}}$ distribution is narrower than the SE distribution as the mixing procedure tends towards some mean value. In the mixing procedure only one random track is used from each SE. The fluctuations within the SE are therefore not considered and tracks from events with different $p_{\mathrm{T}}^{\mathrm{sum}}$ values are used. This results in a mean $p_{\mathrm{T}}^{\mathrm{sum}}$ for the ME and thus large fluctuations as present in the SE are not reproduced in the mixed events.

This follows from the central limit theorem. It states that the distribution of the sum X of N independent variables $X = \sum_{i=1}^{N} x_{\mathrm{i}}$ tends towards a Gaussian function if all x_{i} are independent and equally distributed [82]. The mean value and variance of X is given by the sum of the means and variances of the distributions of x_{i}. In the situation of the SE and ME, the sum X is the sum of all transverse momenta x_i of the particles within one event. While in the SE the variances of all x_i are equal within one event, events with large fluctuations appear. For the ME it is $\sigma_X^2 = \sum_{i=1}^{N} \sigma_i^2$ and thus large fluctuations are not reproduced because in the sum all variances σ_i^2 of the different events are summed for all ME. Only some mean value is obtained. The situation, as described above, is verified with a simulation in the following.

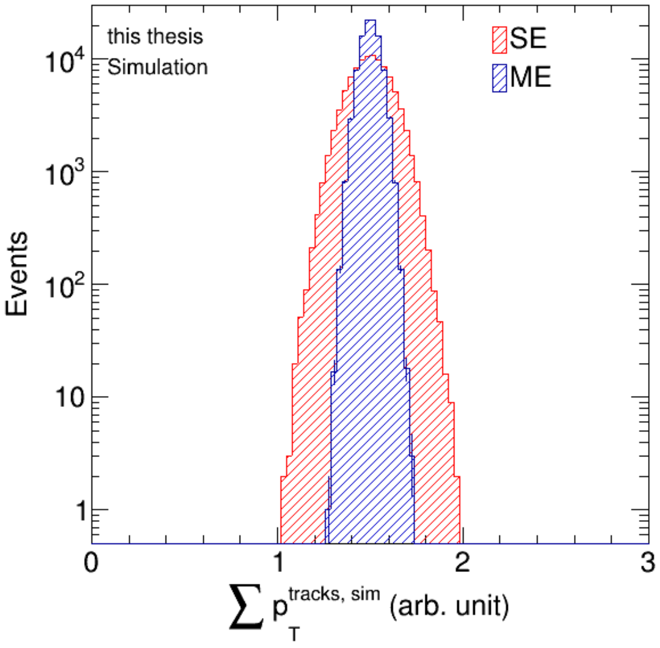

Figure 6.25.: Simulation of the SE and ME $p_\mathrm{T}^\mathrm{sum}$ distribution for 100000 events. The units on the x-axis are arbitrary.

In figure 6.25 fast Monte Carlo simulations of the SE and ME $p_\mathrm{T}^\mathrm{sum}$ distributions are depicted. The $p_\mathrm{T}^\mathrm{sum}$ for the SE is simulated by sampling track p_T values from a Gaussian function with a mean value of 1.5 and a width of 0.5. These values are arbitrary and are not related to the data. In order to simulate the event-by-event fluctuations an additional fluctuation value is added to the mean p_T which was sampled from a Gaussian function too. A mean value of 0 and a width of 0.1 was used to obtain the fluctuation. This fluctuation is fixed for one particular SE.

For the simulation of the ME the same setup was used but now the fluctuation of the mean $p_\mathrm{T}^\mathrm{sum}$ of the event is calculated for each track individually and not only for each event. This simulates the real setup where N tracks from N events with different fluctuations are used for the mixing.

The result of this simulation is shown in the figure 6.25. A smaller distribution for the ME (blue) than for the SE (red) is obtained. This confirms the assumption that the ME mixing procedure leads to a mean $p_\mathrm{T}^\mathrm{sum}$ of the events and the extremes are lost.

The resulting distributions of the real SE and ME for one event category with multiplicity bin three (2126-2209), z-vertex bin two (0-4 cm) and event plane bin zero (-90 - $-72°$) is shown in the left plot of figure 6.26. The $p_{\mathrm{T}}^{\mathrm{sum}}$ distribution of the ME (blue) is significantly smaller than the $p_{\mathrm{T}}^{\mathrm{sum}}$ distribution for the SE (red). Events with very low or large $p_{\mathrm{T}}^{\mathrm{sum}}$ are not reproduced in the mixing, in agreement with the Monte Carlo simulation. The differences in the $p_{\mathrm{T}}^{\mathrm{sum}}$ distributions of the SE and ME might lead to differences in the ρ and jet distributions which is studied in the following.

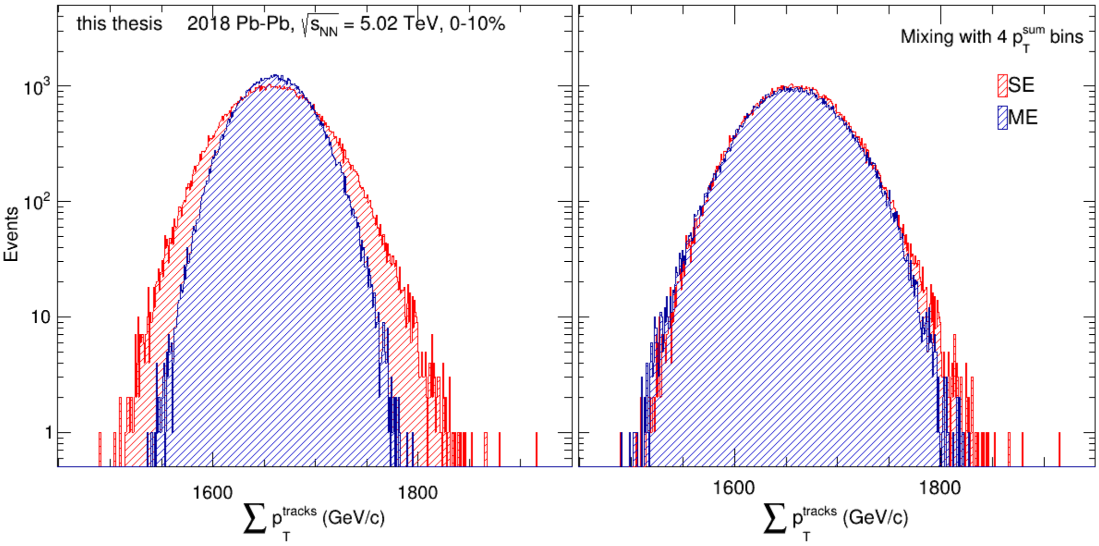

Figure 6.26.: Sum of all transverse momenta of the tracks ($\sum p_{\mathrm{T}}^{\mathrm{track}}$) of the SE (red) and ME (blue) which are used for the jet reconstruction. Left: The mixing was done with multiplicity, event plane and z-vertex bins. Right: An additional splitting of the events into 4 $p_{\mathrm{T}}^{\mathrm{sum}}$ bins for the mixing was used.

In order to test the impact on the ρ and jet distributions, the events are classified into $p_{\mathrm{T}}^{\mathrm{sum}}$ bins for the mixing. Four additional $p_{\mathrm{T}}^{\mathrm{sum}}$ bins are used in the same way as the additional event plane bins introduced in section 6.4.1. Only events with similar $p_{\mathrm{T}}^{\mathrm{sum}}$ values can be used for the mixing. The binning is done by dividing the distribution of the SE shown in the left plot of figure 6.26 into four equal bins. The resulting distributions for the SE and ME with the four additional $p_{\mathrm{T}}^{\mathrm{sum}}$ bins are shown in figure 6.26 in the right plot. The SE and ME $p_{\mathrm{T}}^{\mathrm{sum}}$ distributions are in good agreement as the ME distribution could be broadened by the additional binning.

In addition, the splitting into $p_{\mathrm{T}}^{\mathrm{sum}}$ bins for the mixing solves the deviation between the SE and ME ρ distribution which was observed in 6.3.1 where the ME ρ distribution was always narrower than the SE ρ distribution. In figure 6.27 the SE ρ distribution where one (blue points) and three (black circles) jets are removed for the calculation are depicted. The same category of events as described above was used. In addition, the pileup events are rejected for this study, as described in 4.3.

As already observed in section 6.3.1 ρ becomes smaller if more jets are removed. The ME ρ distribution, where only event plane, multiplicity and z-vertex bins are used for the mixing, is depicted in green. No jets are removed because no real jets are expected in the ME. This distribution is narrower than the SE ρ distribution. As already observed in section 6.3.1 this could not be improved by removing jets in the ME. The distributions are only shifted by varying the number of removed jets.

The resulting ρ distribution where in addition four $p_{\mathrm{T}}^{\mathrm{sum}}$ bins are used is shown in red. By applying this additional binning as described above the ME ρ distribution is broadened and the difference in the shapes between SE and ME ρ vanished. This is also observed in the lower panel, where the rations of the SE (blue), where one jet is removed, and ME ρ distributions are depicted. A large improvement is observed between the ratio SE/ME where the new $p_{\mathrm{T}}^{\mathrm{sum}}$ bins are used (red) and without the new bins (greens).

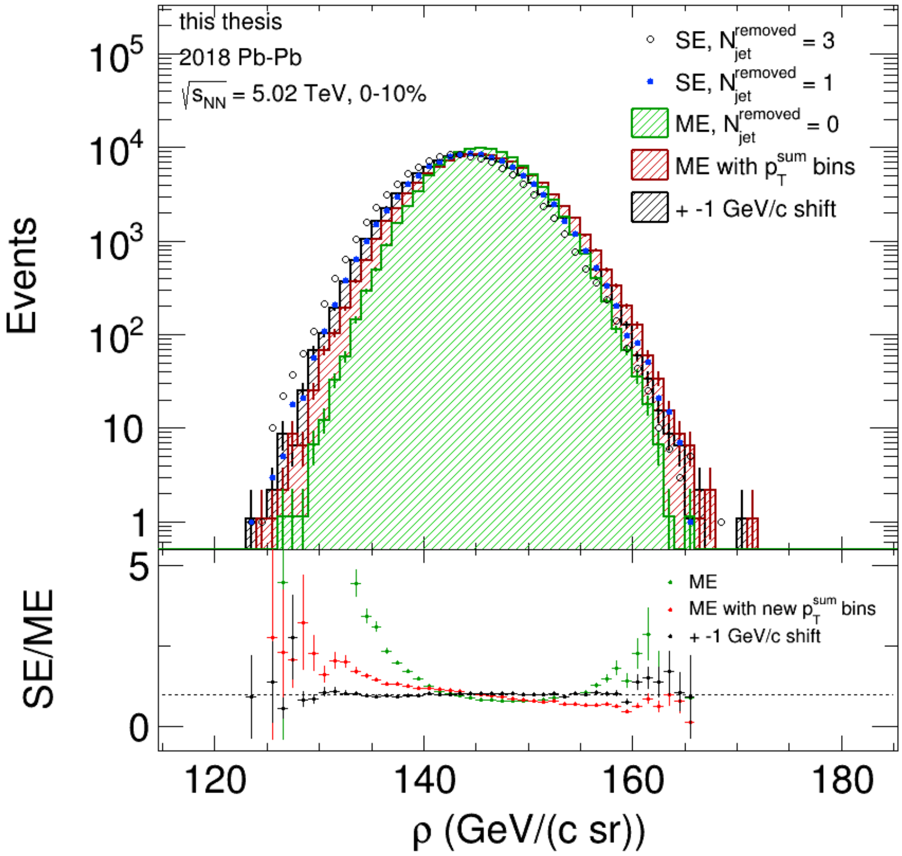

Figure 6.27.: Event-to-event background energy density ρ for the SE, where three (black circles) and one (blue points) jets are removed and for the ME, where zero jets are removed, before (green) and after (red) the additional $p_{\mathrm{T}}^{\mathrm{sum}}$ bins are used. In addition the ME, where zero jets are removed, the $p_{\mathrm{T}}^{\mathrm{sum}}$ bins are used and a shift of -1 GeV/c was used, is depicted (black). In the lower panels the ratios SE/ME are shown between the SE where 1 jet is removed (blue) and the ME without the new bins (green) with the new $p_{\mathrm{T}}^{\mathrm{sum}}$ bins (red) and with the additional shift (black).

Only a remaining shift between the SE and ME ρ distribution is observed. This shift depends on the number of removed jets in the ρ calculation. By comparing the new ρ distribution (red) and the SE where only one jet is removed (blue), only a small deviation of 1 GeV/c is left. To account for this difference, the ME distribution (red) is shifted by -1 GeV/c. The resulting ME distribution is depicted in black. If this additional shift is applied, the ratio, shown in black in the lower panel, is almost equal to one.

As already discussed in section 6.3.1 the procedure of calculating ρ is not unique. Different jet algorithms, jet radii and removed jets can be used. As described in [45] a 60 MeV/c shift was applied to align the ρ distributions of SE and ME. For further studies the 1 GeV/c shift, as described above, should be applied.

In the following only one jet is removed in the SE ρ calculation because this leads to the best agreement between SE and ME ρ without removing jets in the ME.

Due to the broadening of the ρ distribution by the introduction of the $p_{\mathrm{T}}^{\mathrm{sum}}$ bins a broadening of the ME distribution of reconstructed jets is expected. Figure 6.28 depicts the inclusive SE and ME jet $p_{\mathrm{T,jet}}^{\mathrm{reco}}$ distributions. The anti-k_{T} algorithm with a jet radius of $R = 0.3$ and an area cut of $A_{\mathrm{jet}} > 0.2$ was used. The SE jet population is depicted in black and the ME distribution with and without the new $p_{\mathrm{T}}^{\mathrm{sum}}$ bins in red and blue. The normalization of the ME to the SE is done within the shaded region up to -5 GeV/c. The same data set as described above with one multiplicity, z-vertex and event plane bin was used. The ME jet populations with and without the new $p_{\mathrm{T}}^{\mathrm{sum}}$ bins are very similar. Between -22 and -15 GeV/c the ratio in the lower panel is slightly closer to one if the additional bins are used but all points are within their statistical uncertainties. At larger $p_{\mathrm{T,jet}}^{\mathrm{reco}}$ almost no differences between the two ME distributions are observed. Since ρ and $p_{\mathrm{T,jet}}^{\mathrm{raw}}$ should change for the ME at the same time by the mixing with the additional $p_{\mathrm{T}}^{\mathrm{sum}}$ bins, it might be that both effects cancel each other in the $p_{\mathrm{T,jet}}^{\mathrm{reco}}$ distribution. However, in the study of the ME in dependence of the event plane bins, a broadening of the $p_{\mathrm{T,jet}}^{\mathrm{reco}}$ distribution was observed, by including the additional correlations to the ME. Therefore, further studies are necessary in order to get a full picture of the ME jet distribution in dependence of the $p_{\mathrm{T}}^{\mathrm{sum}}$ binning.

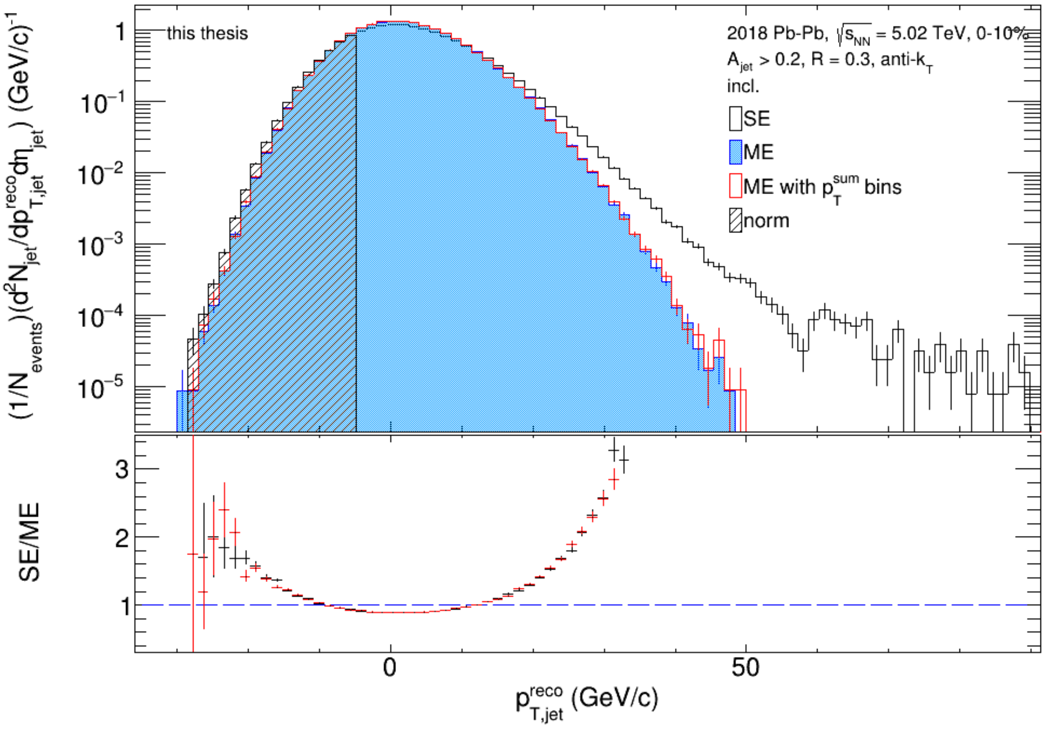

Figure 6.28.: Raw inclusive SE (black) and ME jet $p_{\mathrm{T,jet}}^{\mathrm{reco}}$ distribution for a subset of the data with multiplicity bin three (2126-2209), z-vertex bin two (0-4 cm) and event plane bin zero (-90 - $-72°$). The ME is depicted with the new $p_{\mathrm{T}}^{\mathrm{sum}}$ bins (red) and without the new bins for the mixing (blue). The shaded region indicates the normalization region. The corresponding ratios SE/ME in red (new bins) and black (without new bins) are shown in the lower panel.

7. Raw jet distributions

In this section the SE and ME distributions of reconstructed jets are presented with the full statistics. In addition, raw correlated jet distributions, where the uncorrelated background is subtracted by the ME, are shown. As already mentioned in section 4, the 2018 Pb+Pb data set with a centrality of 0-10% is used with the first 90 runs of the LHC18q run list. The full statistics is used where only the three runs as described in 6.5 are excluded. In addition, the pileup events are rejected as described in 4.3.

For the jet reconstruction the setup, as described in 5.1, is applied and in addition the splitting of the high momentum tracks in the ME, as introduced in 6.1, is used with a 10 GeV/c threshold. One jet is removed in the SE and zero in the ME ρ calculation. The standard bin size of the event plane bins with 18° and the z-vertex bins of 4 cm are used.

In section 7.1 the unbiased inclusive jet distribution is presented 7.1 where no additional cuts are applied. In section 7.2 the quasi-inclusive jet distributions are shown where a small bias of 2-5 GeV/c on the leading tracks of the reconstructed jets are used. For the 4 GeV/c bias different jet radii are compared. In addition, the semi-inclusive hadron-jet (h-jet) spectrum is presented in 7.3 where jets recoiling from a trigger hadron are measured.

7.1. Inclusive jets

In this section the inclusive jet distribution is presented. The inclusive distribution is unbiased and no cuts on the reconstructed jet p_{T} or the jet constituents are applied. Only an area cut, as described in 6.3, is used. From the previous studies the splitting of the high momentum tracks in the ME is used with a threshold of 10 GeV/c.

The resulting jet distribution is presented in figure 7.1. In the upper panel the jet distribution of the SE (black) and the reconstructed jets in the ME (blue) are depicted as function of $p_{\mathrm{T,jet}}^{\mathrm{reco}} = p_{\mathrm{T,jet}}^{\mathrm{raw}} - \rho A$. The jet distributions are normalized to the number of events, used for the jet reconstruction. In addition the ME is normalized to the SE within an interval of -55 to -5 GeV/c, indicated by the shaded region. The reconstructed jet candidates, which are expected to arise from the uncorrelated background at low jet p_{T}, are well described by the ME. Large differences between the SE and ME jet distributions are observed at large positive $p_{\mathrm{T,jet}}^{\mathrm{reco}}$ where the reconstructed objects in the SE are expected to be true correlated jets. Due to the destruction of the jet correlations in the ME and the high momentum splitting no entries are observed in the high p_{T} region for the ME. Only small deviations are visible at the left side tail between SE and ME which are discussed later.

The description of the uncorrelated background with the ME offers the possibility for an inclusive jet measurement down to $p_{\mathrm{T,jet}}^{\mathrm{reco}} = 0$ GeV/c for the first time. As already mentioned, in previous analyses cuts on the reconstructed jet p_{T} where applied to reject uncorrelated background. This is no longer necessary with the application of the ME technique. All true correlated jets which underwent lots of scattering and lose a huge amount of energy within the QGP can be measured as well, by subtracting the uncorrelated background described by the reconstructed jet population of the ME.

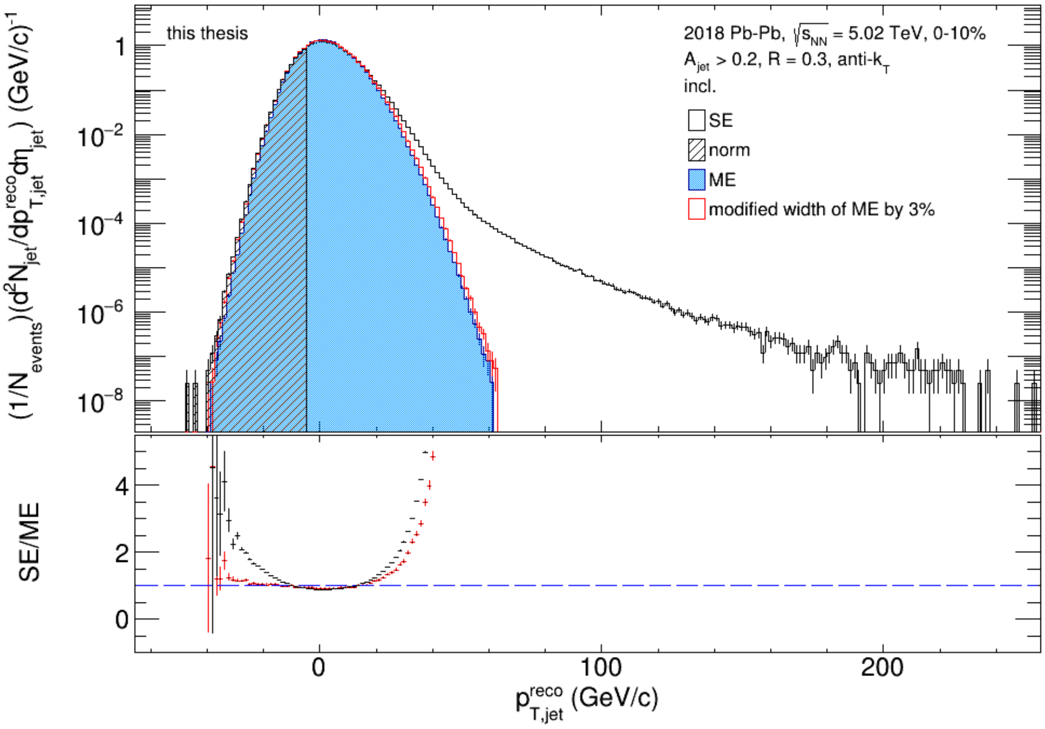

Figure 7.1.: Raw inclusive jet distribution of the SE (black) and ME (blue) in dependence of $p^{\mathrm{reco}}_{\mathrm{T,jet}}$. The ME is normalized to the SE within the shaded region. The ME with a modified width of 3% is shown in red. Lower panel: Ratio SE and ME, without modification (black) and with modified width (red).

The ratio SE/ME is depicted in the lower panel of figure 7.1. Between −10 and 10 GeV/c the ratio is almost equal to one. Around 0 GeV/c the ME is slightly larger than the SE which results in a ratio of SE/ME = 0.9. Below $p^{\mathrm{reco}}_{\mathrm{T,jet}} = -10$ GeV/c a small increase is observed due to a small difference between the ME and SE distributions. The ratio increases up to a value of 2 at −30 GeV/c and then fluctuates around 3 for lower jet $p^{\mathrm{reco}}_{\mathrm{T,jet}}$. The deviation is small because the jet yield has already fallen by 6 orders of magnitude in comparison to the peak.

The remaining difference at $p^{\mathrm{reco}}_{\mathrm{T,jet}} < -10$ GeV/c is investigated in figure 7.1 too. The red distribution depicts the ME population with a modified width of 3%. As it is shown in the lower panel the ratio SE/ME becomes almost one if the ME distribution is broadened by 3%. The effect of the broadening of the ME distribution at larger jet p_{T} with $p^{\mathrm{reco}}_{\mathrm{T,jet}} > 10$ GeV/c is small.

Reasons for the remaining difference might be the limited event plane resolution. As shown in the previous section the reconstructed jet distribution in the ME depends strongly on the event plane. Studies as presented in 6.4.1 could give a dependence of the width of the ME distribution on the number of the event plane bins, used for the mixing. This allows an estimation of the width of the ME distribution if no limiting event plane resolution is present. This can be implemented in further studies as an analytical correction of the ME width.

In addition more run dependent studies could be performed where the SE description by the ME is studied in dependence of the run ID. Possibly additional effects, as observed in 6.5, could lead to a remaining difference between SE and ME at low $p_{\mathrm{T,jet}}^{\mathrm{reco}}$.

In section 6.6 the ρ distribution of the ME could be broadened by the introduction of additional $p_{\mathrm{T}}^{\mathrm{sum}}$ bins. However, the reconstructed jet distribution of the ME did not change by using the additional bins. A reason might be that the modification of the $p_{\mathrm{T,jet}}^{\mathrm{raw}}$ and ρ distributions cancel each other, but further studies are necessary to test this behavior. In order to study the impact of the $p_{\mathrm{T}}^{\mathrm{sum}}$ binning for the full statistics additional $p_{\mathrm{T}}^{\mathrm{sum}}$ bins have to be estimated first for all multiplicity classes. Because a small difference of 1 GeV/c between the SE and ME ρ distributions was still observed an additional shift of the ME ρ should be performed before it is subtracted from the raw jet p_{T}.

In addition, other correlations in the SE which are not present in the ME could lead to a remaining deviation between the SE and ME jet distribution. It is also possible that the jet correlations which are destroyed in the ME lead to a difference in the shapes of the reconstructed jet distributions. The missing high p_{T} jets in the ME lead to an increase in the jet distribution at low jet p_{T} because more objects are reconstructed at lower momenta. This might be the reason for the larger ME jet distribution around 0 GeV/c. In order to confirm this a fast simulation of the ME jet distribution will be performed to obtain the expected ME distribution.

7.2. Quasi-inclusive jet distribution

In the previous section the unbiased inclusive jet distribution without any constraints on the jet population, except the area cut, was presented. A good description of the uncorrelated background in the SE by the ME was obtained. However, difficulties appear in the context of an inclusive distribution. With the anti-k_{T} algorithm jets are reconstructed with a finite area. As the cross-section grows towards low p_{T} the reconstructed jets overlap and the meaning of an inclusive jet distribution gets lost. In order to make the reconstructed objects countable and to deal with overlapping objects a small bias can be introduced. The bias should fulfill the condition that it appears with a probability smaller than one in the events i.e. it should be rare. A small bias on the leading tracks of the reconstructed jets is applied in order to get a unique separation between physical jets and background. The bias which is applied to the jet population is varied to measure its effect on the jet distribution. In addition, it is assumed that the bias affects only the low p_{T} region of the jet distribution. This can be estimated by using different biases and determine a region of the corrected jet distribution where the bias is negligible.

In the following the resulting jet distributions are presented. The p_{T} of the leading track of the reconstructed jets in the SE and ME is required with $p_{\mathrm{T}}^{\mathrm{lead}} > p_{\mathrm{T}}^{\mathrm{min}}$. Values

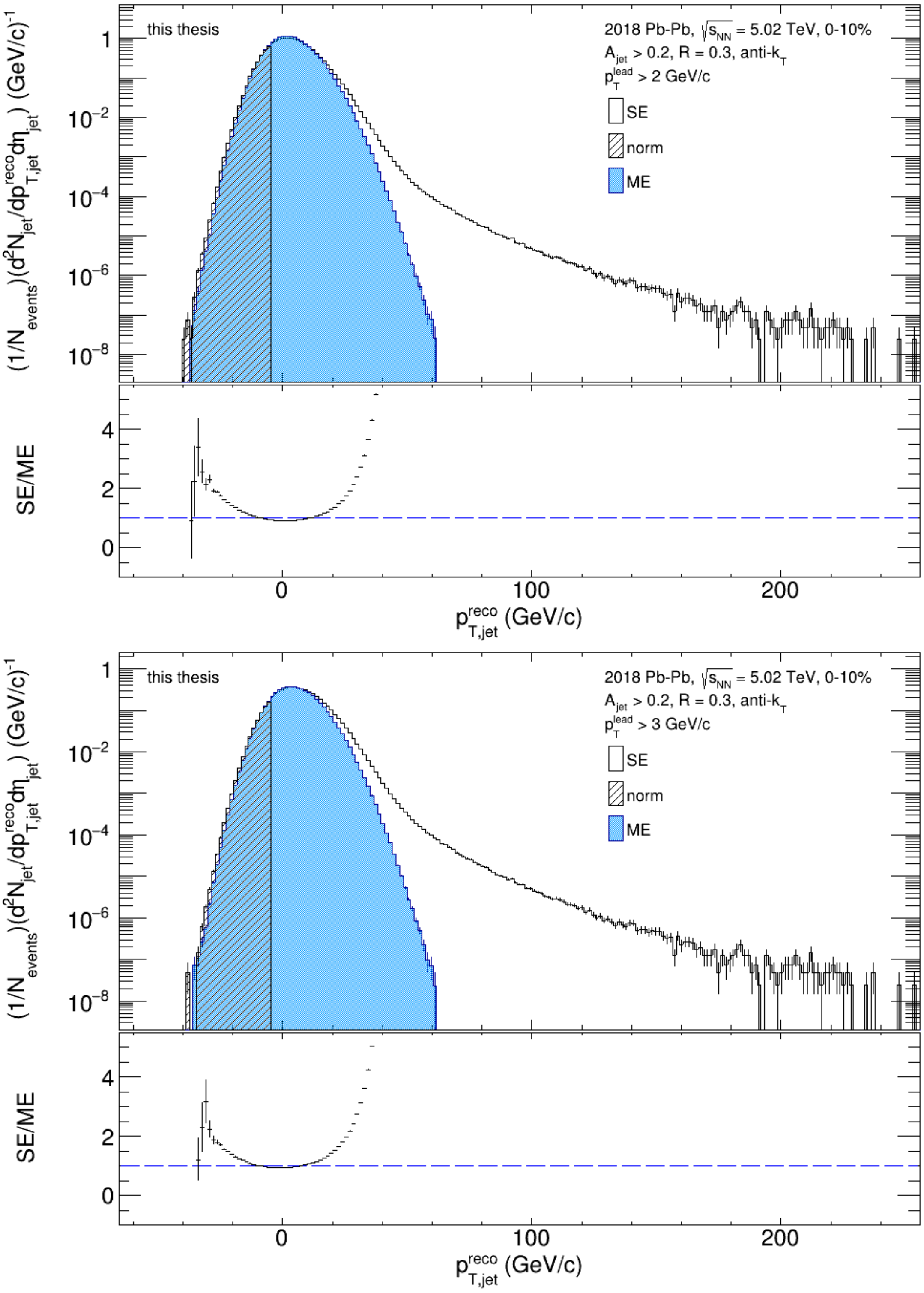

Figure 7.2.: Raw quasi-inclusive SE (black) and ME (blue) jet distributions with a bias of $p_{\mathrm{T}}^{\mathrm{lead}} > 2$ GeV/c (upper) and $p_{\mathrm{T}}^{\mathrm{lead}} > 3$ GeV/c (lower) as function of $p_{\mathrm{T,jet}}^{\mathrm{reco}}$. The ME is normalized to the SE within the shaded region. The ratios SE/ME are shown in the lower panels. The same jet reconstruction setup as in 7.1 is used.

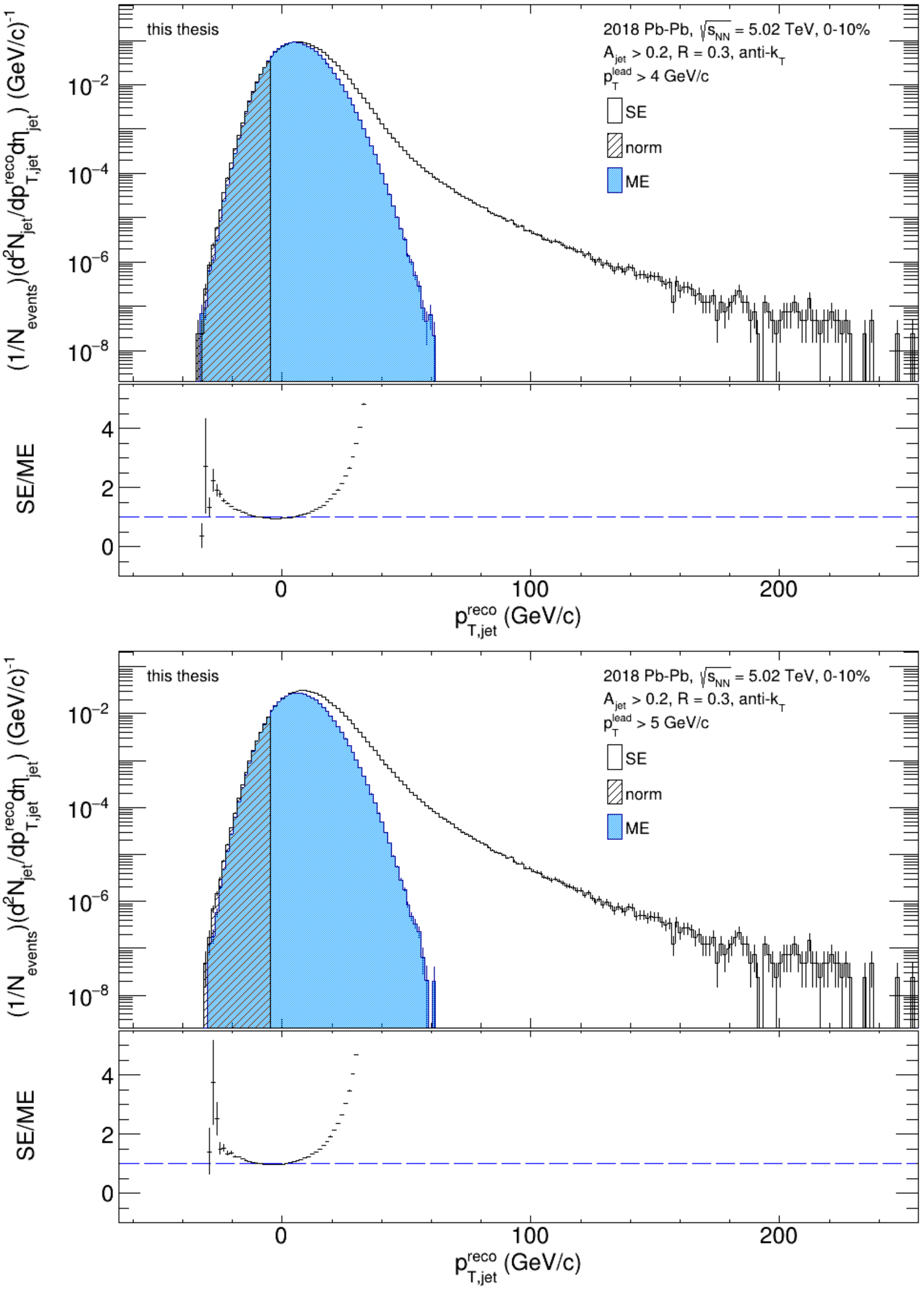

Figure 7.3.: Raw quasi-inclusive SE (black) and ME (blue) jet distributions with a bias of $p_T^{\text{lead}} > 4$ GeV/c (upper) and $p_T^{\text{lead}} > 5$ GeV/c (lower) as function of $p_{\text{T,jet}}^{\text{reco}}$. The ME is normalized to the SE within the shaded region. The ratios SE/ME are shown in the lower panels. The same jet reconstruction setup as in 7.1 is used.

of $p_{\mathrm{T}}^{\mathrm{min}} = 2, 3, 4$ and 5 GeV/c are used and the resulting jet distributions are shown in figures 7.2 and 7.3.

According to the threshold the jet distribution is shifted towards higher jet p_{T} because the requirement of a constituent of the jet with $p_{\mathrm{T}} > p_{\mathrm{T}}^{\mathrm{min}}$ results in jets with $p_{\mathrm{T,jet}}^{\mathrm{raw}} > p_{\mathrm{T}}^{\mathrm{lead}}$. However jets with smaller momenta are observed due to background fluctuations.

The jet distributions with a bias of $p_{\mathrm{T}}^{\mathrm{lead}} > 2$ GeV/c (upper plot) and $p_{\mathrm{T}}^{\mathrm{lead}} > 3$ GeV/c (lower plot) are shown in figure 7.2. In comparison to the unbiased inclusive jet distribution, as depicted in figure 6.21, before the three runs where excluded, the entries on the left side tail of the SE distribution disappeared even without excluding the three runs. Some uncorrelated background jets could be rejected by the bias. Similar to the inclusive spectrum a small difference between SE and ME at low jet $p_{\mathrm{T,jet}}^{\mathrm{reco}} < -10$ GeV/c is observed which is visible in the ratio SE/ME. For the 2 GeV/c bias the ratio grows to SE/ME = 2 at $p_{\mathrm{T,jet}}^{\mathrm{reco}} = -30$ GeV/c. However the jet yield has already fallen by five orders of magnitude where this difference of a factor two is observed. In addition the ME distribution is slightly larger than the SE distribution around 0 GeV/c, where a ratio of SE/ME = 0.92 is observed for the spectra with $p_{\mathrm{T}}^{\mathrm{lead}} > 2$ GeV/c. Similar results with a small improvement are obtained for the 3 GeV/c bias.

Figure 7.3 shows the jet yields for the 4 GeV/c (upper plot) and 5 GeV/c (lower plot) bias. A further improvement of the SE description at the left side by the ME is observed for larger thresholds. Only a very small deviation from one of 0.04 is visible in the ratio of the SE and ME around 0 GeV/c with a 4 GeV/c bias and 0.03 for the 5 GeV/c bias. For the 5 GeV/c bias the ratio grows up to 1.5 at $p_{\mathrm{T,jet}}^{\mathrm{reco}} = -25$ GeV/c. Large fluctuations are observed at lower jet $p_{\mathrm{T,jet}}^{\mathrm{reco}}$ due to the decreasing statistics. In general the description of the uncorrelated background by the ME can be further improved if a small bias is applied to the jets. As already described above some low $p_{\mathrm{T,jet}}^{\mathrm{reco}}$ background jets are rejected if a cut on the leading track of the jets is applied. The distribution is cleaned up and the description of the uncorrelated background by the ME becomes more precise.

Figure 7.4 depicts the correlated jet distribution, where the uncorrelated background in the SE was subtracted by the ME. The results are shown for the 4 GeV/c (black) and 5 GeV/c (red) bias. As expected a larger signal is obtained if a smaller bias is used as less jets with lower p_{T} are rejected. The better description of the uncorrelated background by the ME in the SE for a larger threshold of the leading track, as already observed in figure 7.3, is visible too. Between -9 GeV/c and 4 GeV/c the lowest dip of -0.003 is observed for the jet distribution with a 4 GeV/c bias. This corresponds to 18 % of the signal peak. For the 5 GeV/c bias a smaller dip of only 5% of the signal peak is observed. For both jet distributions the difference below -10 GeV/c is very small, as already shown in the uncorrelated jet distributions, since the statistics already decreases significantly.

The correction of this correlated jet distribution is presented in section 8. In the next section different jet radii are studied for the quasi-inclusive jet distribution with a 4 GeV/c bias.

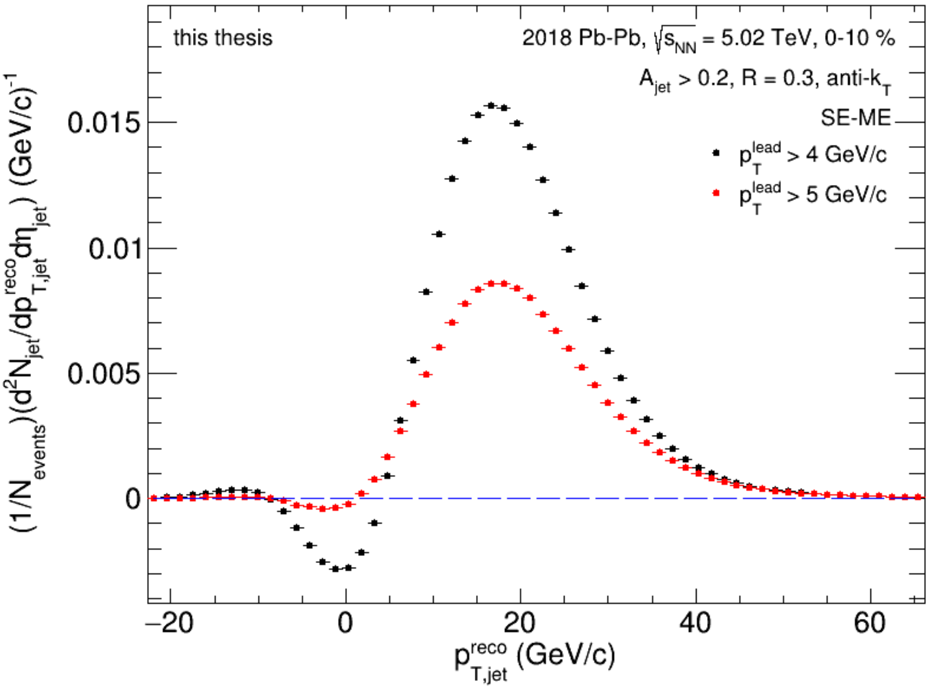

Figure 7.4.: Raw correlated quasi-inclusive jet distribution with a bias of $p_{\mathrm{T}}^{\mathrm{lead}} > 4$ GeV/c (black) and $p_{\mathrm{T}}^{\mathrm{lead}} > 5$ GeV/c (red) as function of $p_{\mathrm{T,jet}}^{\mathrm{reco}}$. The uncorrelated background was subtracted by the ME.

7.2.1. Variations of the jet radius

In this section variations of the jet radius are presented. The jet radius is a central parameter in the definition of the setup for the jet reconstruction. It determines how many particles of a jet are collected. While for smaller jet radii the probability increases that particles of the jet are missed in the reconstruction, the signal-to-background ratio gets worse if a larger radius is used. In p+p collisions the comparison of jets, reconstructed with different jet radii, measures the distribution of the jet energy transverse to the jet axis. Possible modifications of the jet shape can be measured by comparing different jet radii in heavy-ion collisions. For example in [45] the ratios of the jet distributions, reconstructed with different R, in central and peripheral collisions are compared in order to search for medium induced broadening of the jet.

In this section the quasi-inclusive jet distribution with a 4 GeV/c bias is used with the same setup for the jet reconstruction as used for the jet distribution shown in the previous section in figure 7.3. The results for the different jet radii of $R = 0.2$ (upper plot) and $R = 0.4$ (lower plot) are shown in figure 7.5. The area cut is adapted to the respective jet radii. A cut of $A_{\mathrm{jet}} > 0.05$ is used for $R = 0.2$ and $A_{\mathrm{jet}} > 0.35$ is used for $R = 0.4$. For both jet radii the SE jet yield is presented in black and the ME distribution in blue. The shaded region is the normalization region which is the same as used in previous sections. In addition the distributions are normalized to the number of used events N_{events}. The ratios SE/ME are shown in the lower panels.

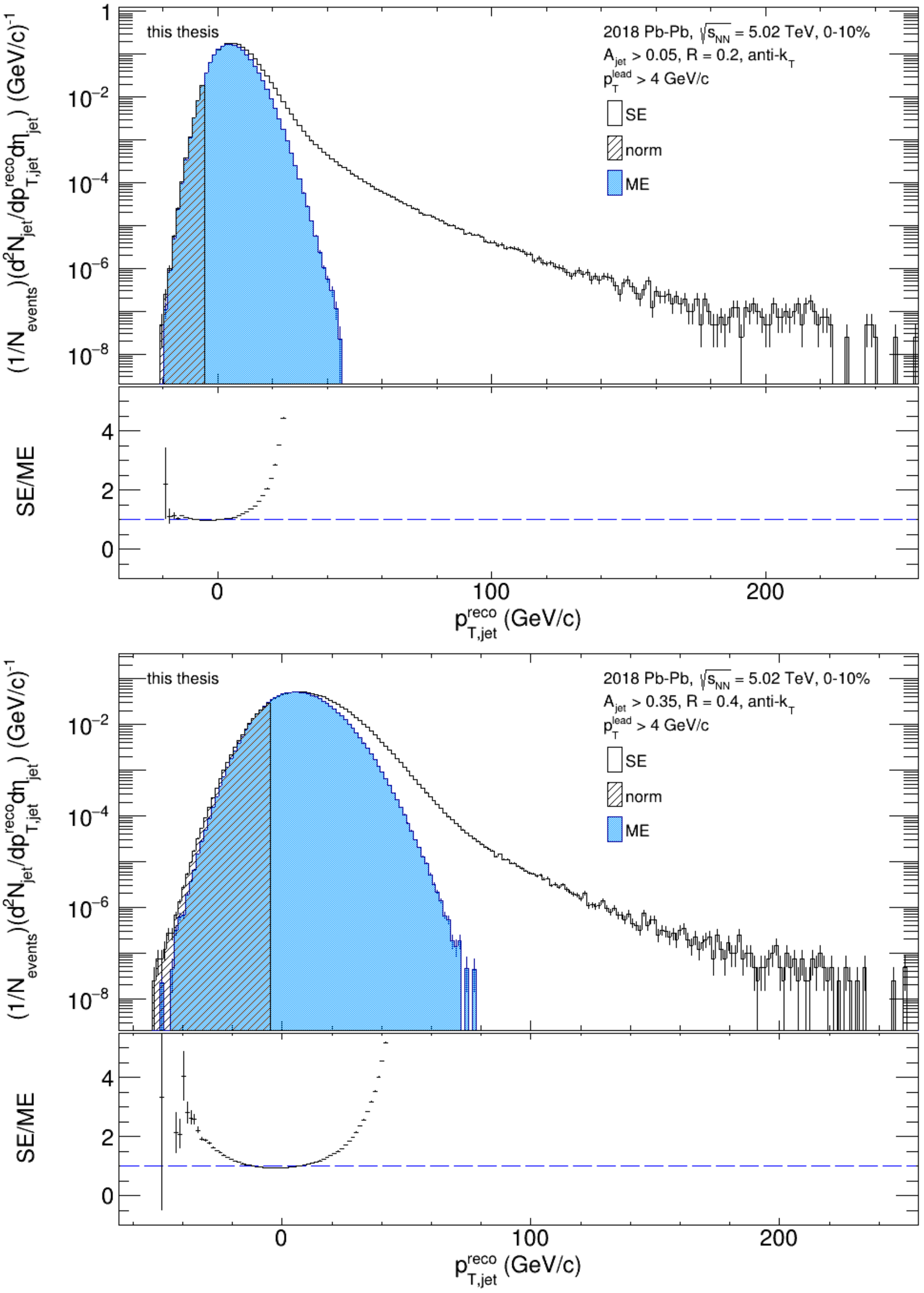

Figure 7.5.: Raw quasi-inclusive SE (black) and ME (blue) jet distribution with a bias of $p_T^{lead} > 4$ GeV/c as function of $p^{reco}_{T,jet}$. The anti-k_T algorithm with $R = 0.2$ and $A_{jet} > 0.05$ (upper plot) and with $R = 0.4$ and $A_{jet} > 0.35$ (lower plot) was used for the jet reconstruction. The ME is normalized to the SE within the shaded region. The ratios are shown in the lower panels.

The peak of both jet distributions is shifted to positive $p_{\mathrm{T,jet}}^{\mathrm{reco}}$ because a 4 GeV/c bias on the leading track was applied. The reconstructed jet yield is larger for the smaller jet radius of $R = 0.2$. This is expected as more jet candidates are reconstructed if a smaller radius and thus a smaller jet area is used. The number of reconstructed jet candidates per event can be calculated by integrating the SE jet distribution over the full $p_{\mathrm{T,jet}}^{\mathrm{reco}}$ range. As expected the integral decreases with increasing jet radius. For a jet radius of $R = 0.2$ an integral of 1.88 is obtained, while the number of reconstructed jets decreases to 1.46 for $R = 0.3$ and 1.12 for $R = 0.4$. The result for $R = 0.3$ is obtained from the previous section.

The description of the uncorrelated background in the SE by the ME distribution is improved if the jet radius is reduced from $R = 0.3$ to $R = 0.2$. Almost no deviations between the SE and ME distribution for $R = 0.2$ below $p_{\mathrm{T,jet}}^{\mathrm{reco}} < 0$ GeV/c are observed. Between -10 and -18 GeV/c very small deviations of about 10 % are observed where the jet distribution is already reduced by three orders of magnitude.

In comparison to the reconstructed jet distribution with $R = 0.3$ the description of the uncorrelated background by the ME becomes worse if the radius is increased to $R = 0.4$. The deviation between SE and ME at the left side at $p_{\mathrm{T,jet}}^{\mathrm{reco}} < -10$ GeV/c increases where the SE distribution is larger than the ME distribution while around 0 GeV/c the ME distribution is slightly larger than the SE distribution. The same behavior as observed before, for example for the inclusive jets, with a narrower ME distribution is shown. In particular entries at $p_{\mathrm{T,jet}}^{\mathrm{reco}} < -45$ GeV/c are visible in the SE which are not described by the ME. However the jet distribution is already fallen by five orders of magnitude.

Figure 7.6 depicts the raw correlated jet distributions with $p_{\mathrm{T}}^{\mathrm{lead}} > 4$ GeV/c for various jet radii. The ME distributions are subtracted from the SE distributions, presented in figure 7.5 and in the upper plot of figure 7.3. The results are shown again for $R = 0.2$ (black), $R = 0.3$ (red) and $R = 0.4$ (blue). The widths of the distributions increase with increasing R as already observed for the uncorrelated jet distribution. In addition the peak is shifted to larger $p_{\mathrm{T,jet}}^{\mathrm{reco}}$ for larger jet radii. The signal is centered around 12 GeV/c for $R = 0.2$, 17 GeV/c for $R = 0.3$ and 23 GeV/c for the largest jet radius of $R = 0.4$. This is expected as the reconstructed jet energy increases with increasing jet radius. Negative values are observed around 0 GeV/c in all cases due to the difference between SE and ME distribution, as described above. The region and the magnitude of those entries decreases with decreasing R. For $R = 0.2$ negative entries are observed between -7 and 1 GeV/c while the region extends to -11 to -6 GeV/c for $R = 0.4$. This was expected from the observed differences described above. In general small deviations from 0 at $p_{\mathrm{T,jet}}^{\mathrm{reco}} < 0$ GeV/c are possible due to statistical fluctuations.

The quasi-inclusive raw correlated jet distribution with $p_{\mathrm{T}}^{\mathrm{lead}} > 5$ GeV/c are shown in the appendix in figure A.6. With the 5 GeV/c bias almost no deviations from 0 are observed below $p_{\mathrm{T,jet}}^{\mathrm{reco}} = 0$ GeV/c for all jet radii. The larger bias leads to a cleaner jet distribution where more background jets are rejected which results in a better description by the ME.

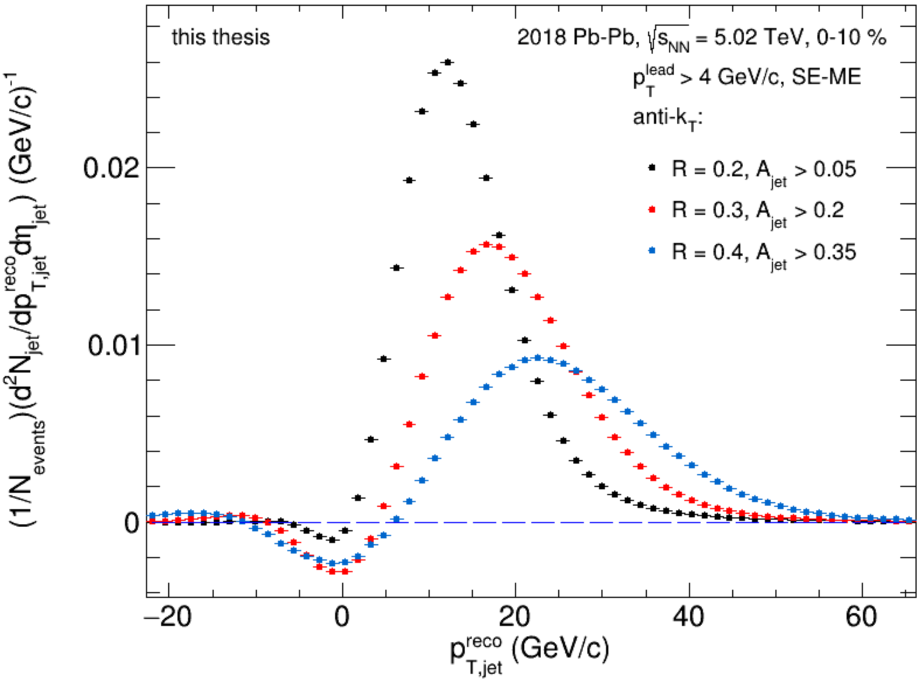

Figure 7.6.: Raw correlated quasi-inclusive jet distribution with a bias of $p_{\mathrm{T}}^{\mathrm{lead}} >$ 4 GeV/c as function of $p_{\mathrm{T,jet}}^{\mathrm{reco}}$. For the jet reconstruction the anti-k_{T} algorithm was used with a jet radius of $R = 0.2$ (black), $R = 0.3$ (red), $R = 0.4$ (blue).

7.3. Hadron-jet distribution

In this section the semi-inclusive hadron-jet (h-jet) distribution is presented. For the h-jet distribution, the recoiling jets from a high p_{T} trigger hadron are used as described in [45, 48] and introduced in section 2.3.2. Within an event a hadron is used as trigger particle if it is within some certain trigger p_{T} interval. In the case that there are several trigger candidates, one particle is picked randomly. The azimuthal angle ϕ_{trigger} of the trigger particle defines the jet axis and all recoiling jets which are within the interval $\phi_{\mathrm{trigger}} + \frac{3}{4}\pi$ up to $\phi_{\mathrm{trigger}} + \frac{5}{4}\pi$ are accepted. The studied observable corresponds to $Y(p_{\mathrm{T,jet}})$, the jet yield integrated over the recoil region $\phi = 3\pi/4$ to $\phi = 5\pi/4$ as described in [45] and shown in equation 7.1. The jet yield in the equation is normalized to the number of trigger hadrons $N_{\mathrm{trig}}^{\mathrm{AA}}$, where AA refers to the collision system. The transverse momentum and the pseudo-rapidity of the jet are represented by $p_{\mathrm{T,jet}}$ and η_{jet} while $\Delta\phi$ is the angle of the jet relative to the trigger hadron in azimuth.

$$Y(p_{\mathrm{T,jet}}) = \int_{\frac{3\pi}{4}}^{\frac{5\pi}{4}} d\Delta\phi \left(\frac{1}{N_{\mathrm{trig}}^{\mathrm{AA}}} \cdot \frac{d^3 N_{\mathrm{jet}}^{\mathrm{AA}}}{dp_{\mathrm{T,jet}} d\Delta\phi d\eta_{\mathrm{jet}}} \bigg|_{p_{\mathrm{T,trig}}^{\mathrm{min}} < p_{\mathrm{T,trig}} < p_{\mathrm{T,trig}}^{\mathrm{max}}} \right) \tag{7.1}$$

The selection of the recoiling jets from a high p_{T} trigger hadron represents a clean probe of jets because only high p_{T} processes are used. However, the recoiling jets can lose lots of energy within the medium if the jet production happened at the edge of the interaction region.

The resulting raw recoil jet distribution is presented in figure 7.7. The upper panel shows the SE jet distribution recoiling from a trigger hadron with $20 < p_{\mathrm{T,trig}} < 100$ GeV/c (black) and with $3 < p_{\mathrm{T,trig}} < 5$ GeV/c (red). The high p_{T} trigger region is used to select a high p_{T} process, where the recoiling jet candidate is expected to be a true jet. For comparison the small trigger p_{T} region of $3 < p_{\mathrm{T,trig}} < 5$ GeV/c is used, where the recoiling jet candidates are expected to be uncorrelated background. Variations of the trigger p_{T} interval can be done in further studies.

In addition the ME jet distribution is shown (blue) in figure 7.7 where all reconstructed objects recoiling from a hadron with $p_{\mathrm{T}} > 2$ GeV/c are used. This value is arbitrary because no high p_{T} processes where jets are produced exist in the ME. The shaded region is again the normalization region of the ME. The ME distribution normalized to the SE distribution with $20 < p_{\mathrm{T,trig}} < 100$ GeV/c (black) is shown in the figure. However, for the calculation of the ratio in the lower panel, the ME distribution is normalized separately to both SE distributions. All jet yields are normalized to the number of trigger hadrons N_{trig}.

For both SE distributions a good description of the uncorrelated background at the left side tail is obtained by the ME. Between -10 and 10 GeV/c a ratio almost equal to one is observed. It slightly increases at $p_{\mathrm{T,jet}}^{\mathrm{reco}} < -10$ GeV/c as observed for the inclusive and quasi-inclusive distributions. Possible reasons for this deviation are already discussed in 7.1. The difference between the two trigger p_{T} values at low $p_{\mathrm{T,jet}}^{\mathrm{reco}}$ is small. In the region where only uncorrelated background is expected the reconstructed jet distribution does not depend on the selected trigger hadron. At $p_{\mathrm{T,jet}}^{\mathrm{reco}} > 20$ GeV/c the behavior of the two SE distributions with different trigger intervals becomes different. As expected the difference to the ME distribution is larger for higher trigger p_{T}. In addition the energy of the jets becomes larger for larger trigger p_{T} values because the overall energy of the selected process is larger. The smaller the selected trigger p_{T}, the more background objects are reconstructed as expected. Therefore the SE jet distribution gets closer to the ME distribution. As already observed in [45] the number of uncorrelated recoil jets is independent of the selected trigger p_{T} and only the number of true correlated jets is varied.

Variations of the trigger p_{T} as well as different jet radii can be used in further studies. In addition, studies of the small remaining difference in the SE and ME at low jet p_{T}, as observed in the previous sections, are necessary.

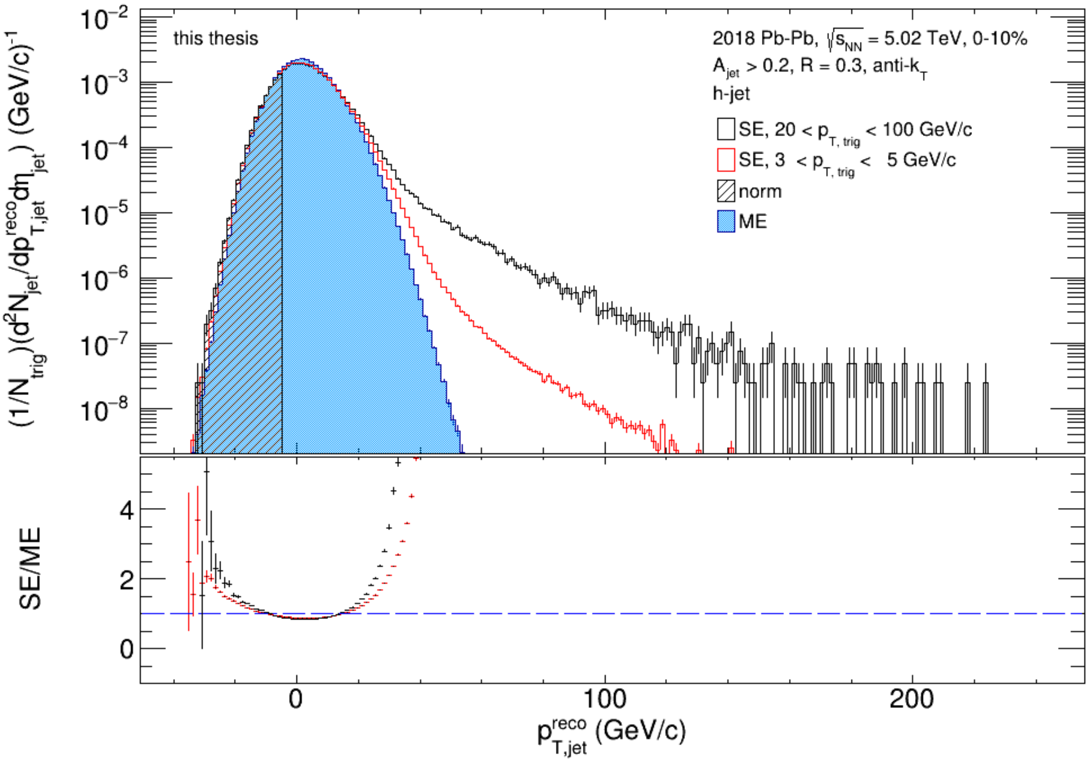

Figure 7.7.: Hadron-jet distributions of the SE with a trigger hadron of $20 < p_{\mathrm{T,trig}} < 100$ GeV/c (black) and $3 < p_{\mathrm{T,trig}} < 5$ GeV/c (red) and the ME jet distribution (blue). The ME is normalized to the SE within the shaded region. The corresponding ratios SE/ME are shown in the lower panel.

8. Corrections

The raw correlated quasi-inclusive jet distributions were presented in the previous section 7 with a 4 and 5 GeV/c leading track cut. It is necessary to correct them for detector effects as the reconstruction efficiency and background fluctuations which result in p_{T}-smearing. The corrections of the raw distributions are done by using an unfolding method. The general unfolding procedure follows the description in [45].

The aim of the unfolding is the calculation of the true jet distribution out of the measured signal. The response matrices R_{bkg} and R_{det}, which take care of the background and instrumental effects, relate the true and measured jet distributions T and M as shown in equation 8.1 [45]. The reconstructed jet $p_{\mathrm{T,jet}}^{\mathrm{reco}}$ was already introduced in equation 2.11. It is affected by the detector effects and the p_{T}-smearing which results from background fluctuations. The particle-level jet p_{T}, which is the true jet p_{T} without detector and background effects, is described by $p_{\mathrm{T,jet}}^{\mathrm{part}}$. For the detector-level jet p_{T} ($p_{\mathrm{T,jet}}^{\mathrm{det}}$) instrumental effects are applied to the particle-level jets. The inversion of equation 8.1 reproduces the true jet distribution out of the measured jet distribution.

$$M(p_{\mathrm{T,jet}}^{\mathrm{reco}}) = \left[R_{\mathrm{bkg}}(p_{\mathrm{T,jet}}^{\mathrm{reco}}, p_{\mathrm{T,jet}}^{\mathrm{det}}) \times R_{\mathrm{det}}(p_{\mathrm{T,jet}}^{\mathrm{det}}, p_{\mathrm{T,jet}}^{\mathrm{part}})\right] \times T(p_{\mathrm{T,jet}}^{\mathrm{part}}) \tag{8.1}$$

Several steps are necessary in order to perform the unfolding which are described in the next sections. The true particle-level jet generation by using the PYTHIA event generator [83, 84] is described in section 8.1. The efficiency and a p_{T}-smearing are applied in order to obtain the detector-level jets out of the particle-level jets. The used efficiencies are described in section 8.2. The embedding of PYTHIA jets into real data, to calculate the response matrix, follows in section 8.3. In the last section 8.4 the unfolding procedure is described and first results of the corrected jet distribution are presented.

8.1. Particle-level jet generation with PYTHIA

The particle-level jets, which are necessary for the calculation of the response matrix are generated by using the PYTHIA event generator.

PYTHIA is a very common tool used for the event generation in high-energy collisions, as performed at the LHC, based on Monte-Carlo methods [83, 84].

Different physics processes are included in PYTHIA for the particle production. For example the parton distribution functions of the two incoming particles are considered as well as the initial state radiation. Hard scatterings, typically $2 \rightarrow 2$ processes as $q\bar{q} \rightarrow gg$ and soft processes as elastic scatterings are calculated. Resonance decays and final state parton showers are included too. As last state of the collision the fragmentation process and secondary decays are described. All these processes are included in the event generation based on theory and model description of data. Center-of-mass energies between 10 GeV and 100 TeV can be used for the simulation as well as different colliding particles [85].

The output of the simulation contains event information and properties of the particles as their momenta and masses which can be used for different purposes. Simulations are important tools for the search of new processes. Predictions can be used as input for the design of the detectors or the searching strategy. In addition they are used for the comparison with results obtained from real data where for example model predictions can be tested. Background and uncertainties as the detector efficiency can be estimated with simulated events.

For our purpose PYTHIA is used to generate p+p particle-level jets. For the production of the jets a collision energy of $\sqrt{s_{\mathrm{NN}}} = 5.02$ TeV was used. The jets are produced for different phase space intervals. A minimum and maximum value for $\hat{p}_{\mathrm{T}}$, the scale of the hard-scattering [84], is set, in order to obtain defined phase space intervals. They are weighted later with the appropriate cross-sections. In total 7 phase space bins are used and 500000 events are generated for each bin. Only charged tracks are used which are within the acceptance of $|\eta| < 0.9$.

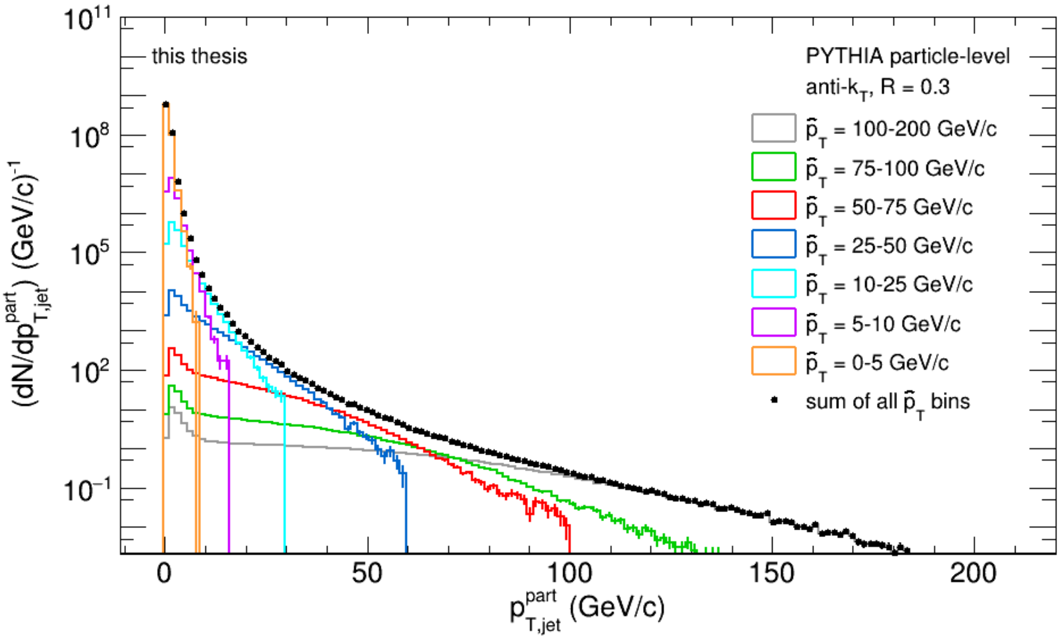

Figure 8.1.: PYTHIA generated p+p particle-level jet distributions at $\sqrt{s_{\mathrm{NN}}} = 5.02$ TeV for different $\hat{p}_{\mathrm{T}}$ bins: 100-200 GeV/c (gray), 75-100 GeV/c (green), 50-75 GeV/c (red), 25-50 GeV/c (blue), 10-25 GeV/c (cyan), 5-10 GeV/c (pink), 0-5 GeV/c (orange). The distributions are scaled with their cross-sections. The same setup for the jet reconstruction as for real data (see section 5.1), except the area cut, is used. Only the reconstructed jet with the largest energy is accepted. The sum of all individual scaled distributions is depicted in black.

The generated PYTHIA events are included into the main program where the jet analysis is performed. Figure 8.1 shows the reconstructed PYTHIA particle-level jets for different $\hat{p}_{\mathrm{T}}$ bins. For the reconstruction the anti-k_{T} algorithm is used with the same setup as for real data which was described in section 5.1. In particular a jet radius of $R = 0.3$ is used because the raw correlated jet distribution with $R = 0.3$ is used for the unfolding first. If more jets are reconstructed which fulfill this requirement, the jet with the largest energy is used.

In comparison to the real data no area cut is applied. The general concept of the jet area is only defined in heavy-ion collisions or in processes, where the fragmentation of the initially produced high p_{T} parton is large. However, the definition of a jet radius is not possible if the fragmentation is too low, as it can happen for the p+p PYTHIA generated jets. In some events only a few particles are generated and jets with very small areas are reconstructed with the anti-k_{T} algorithm. To avoid the rejection of those jets, no area cut is applied.

The individual jet distributions are scaled with the different production cross-sections from the PYTHIA generator. The cross-sections σ in mb for the different phase space intervals are listed in table 8.1. The sum of all scaled distributions for the different $\hat{p}_{\mathrm{T}}$ bins is depicted in black in figure 8.1.

Table 8.1.: Cross-sections σ for the different phase space intervals of $\hat{p}_{\mathrm{T}}$.

$\hat{\boldsymbol{p}}_{\mathbf{T}}$(GeV/c)	100-200	75-100	50-75	25-50	10-25	5-10	0-5
$\boldsymbol{\sigma}$(mb)	$1.653 \cdot 10^{-4}$	$5.035 \cdot 10^{-4}$	$3.608 \cdot 10^{-3}$	0.078	2.768	28.62	1621

To obtain the response matrices, the particle-level jets have to be matched with the detector-level jets. In order to get the detector-level jets instrumental effects are applied to the particle-level jets. In the next section the efficiency and the p_{T} resolution is introduced.

8.2. Instrumental effects

The measured jet p_{T} ($p_{\mathrm{T,jet}}^{\mathrm{reco}}$) which is reconstructed with the jet algorithm is influenced by several detector effects due to technical limitations as a limited acceptance, efficiency or resolution. The main contributions are described in the following.

The tracking efficiency of single particles represents the largest contribution of the instrumental response. It describes the fraction of all generated tracks which could be measured and reconstructed with procedures as described in 3.3. This leads to a shift of the true jet energy towards lower reconstructed jet energies because some particles are missing. To account for this in the unfolding procedure, the efficiency is estimated and applied for the calculation of the detector-level jets.

The efficiencies can be estimated by using Monte-Carlo simulated events. They contain the simulated true physical tracks and tracks where the predicted detector effects are applied. A matching between the true tracks and the simulated reconstructed tracks has to be done in order to estimate the efficiency. Because the estimation of the efficiency was beyond the scope of this thesis, the results from [86] are used. The tracking efficiency in dependence of the track p_{T} are shown in figure 8.2. It was calculated using the MC data set of LHC17c5a,b for an interaction rate of 0 to 2 kHz. The estimated value for the efficiency is between 0.78 and 0.83 in the considered $p_{\mathrm{T,track}}$ range.

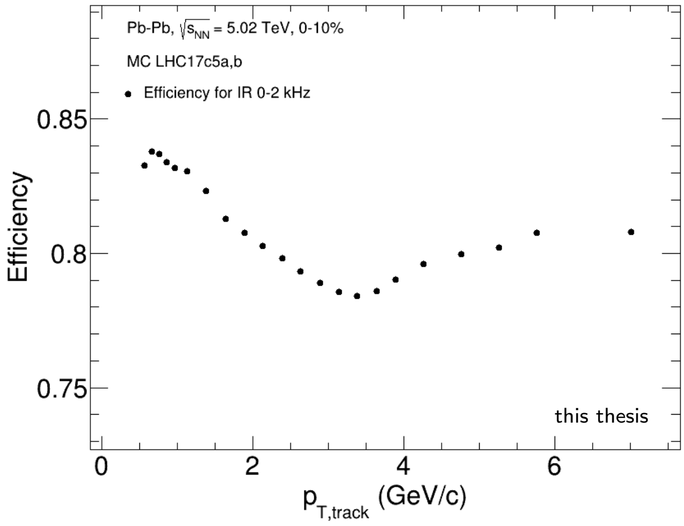

Figure 8.2.: Tracking efficiency in dependence of $p_{\mathrm{T,track}}$ obtained from Pb-Pb MC simulation at $\sqrt{s_{\mathrm{NN}}} = 5.02$ TeV. Results are taken from [86].

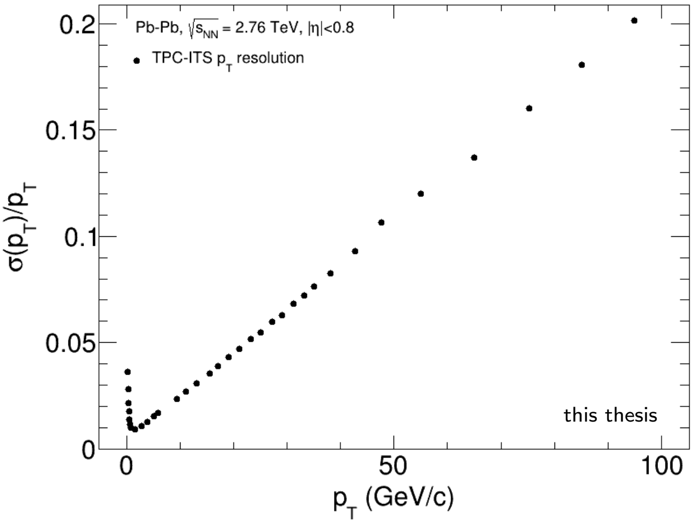

Figure 8.3.: TPC-ITS p_{T}-resolution for Pb-Pb at $\sqrt{s_{\mathrm{NN}}} = 2.76$ TeV. Results are taken from [87].

In addition a limited track momentum resolution leads to a p_{T}-smearing of the reconstructed jets. The p_{T}-resolution for TPC and ITS reconstructed tracks is taken from [87]. The resulting p_{T} resolution $\sigma(p_{\mathrm{T}})/p_{\mathrm{T}}$ is shown in figure 8.3. In order to obtain the absolute resolution the y-values are multiplied with the corresponding p_{T} values.

The detector-level jets can be obtained by applying the p_{T}-resolution to the PYTHIA particle-level tracks. This is done by selecting a random p_{T} from a Gaussian distribution with the original $p_{\mathrm{T,track}}^{\mathrm{part}}$ as mean value and $\sigma(p_{\mathrm{T,track}}^{\mathrm{part}})$ as width. After that the efficiency is used where a random value between 0 and 1 is selected. If this value is smaller than the efficiency obtained from figure 8.2 the track is accepted otherwise it is discarded. This results in a rejection of about 20% of the tracks. The obtained detector-level tracks are used for the jet reconstruction where the same setup for the clustering is used as for the particle-level tracks in the described in the previous section.

The instrumental response matrix is obtained by matching the detector-level and particle-level jets. This is described in more detail in the next section as well as the calculation of the full response matrix by embedding the detector-level jets into real data.

8.3. Response matrix

In the previous sections the determination of the true particle-level jets and the detector-level jets were described. In this section the calculation of the response matrix by using the PYTHIA generated jets and an embedding method is presented.

In equation 8.1 the full response matrix is given as a convolution of the instrumental response matrix R_{det} and the background response matrix R_{bkg}. In the following the calculation of both individual response matrices is described briefly. However, the full response matrix is calculated as it is necessary in order to do the unfolding.

The instrumental response matrix R_{det} to correct the detector effects can be obtained by matching the particle-level and detector-level jets. For the matching the jets which share most of their energy are used. The individual tracks of the jets can be identified by η and ϕ as the position was not changed during the application of the detector effects. An example of an instrumental response matrix is shown in the upper plot of figure 8.4. The particle-level jets generated with PYTHIA with a phase space interval of $\hat{p}_{\mathrm{T}} = 75 - 100$ GeV/c are matched to the detector-level jets. For the jet reconstruction of particle and detector-level jets the anti-k_{T} algorithm with $R = 0.3$ and the same setup as used for the real data, except the area cut, was applied. The strong effect of the efficiency is visible as most of the detector-level jets have smaller energies than the corresponding particle-level jets. The smaller effect of the p_{T}-smearing is observed too, since some particle-level jet energies are smeared to higher values in $p_{\mathrm{T,jet}}^{\mathrm{det}}$.

Fluctuations in the background energy density of a single event are not described by ρ, which only accounts for the event-to-event fluctuations. In order to correct local fluctuations the uncorrelated background response matrix R_{bkg} is used. To calculate the background fluctuations an embedding method of PYTHIA jets into real data can be used. The response matrix is obtained by the embedding of reconstructed PYTHIA detector-level jets into the SE. The detector-level jets are obtained as described above. The jet with the largest energy is used for the embedding. The tracks of this jet are simply added to the PseudoJet vector where the tracks of the real data (same event) are stored. After the embedding the jet reconstruction is carried out. This results again in the reconstruction of the PYTHIA detector-level jet but now additional particles from the underlying event are within the jet area. This reconstructed jet is matched to the detector-level jet which was reconstructed

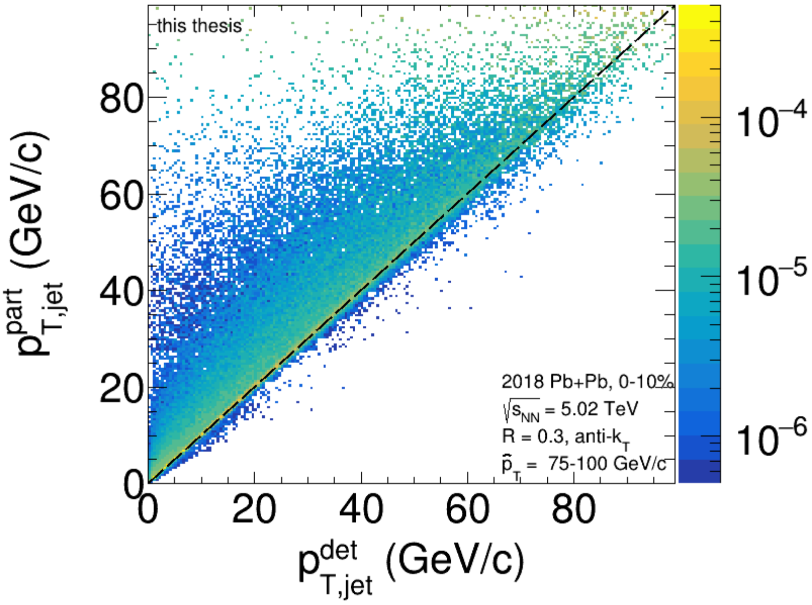

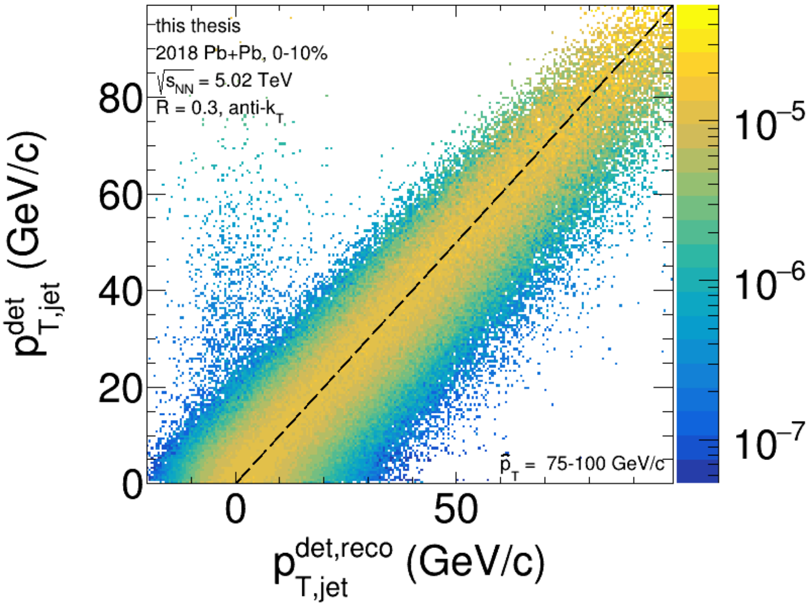

Figure 8.4.: Response matrices where PYTHIA generated particle-level jets with $\hat{p}_{\mathrm{T}} = 75 - 100$ GeV/c are used and the jets which share the largest energy fraction are matched. Upper: Instrumental response matrix with particle-level jet $p_{\mathrm{T,jet}}^{\mathrm{part}}$ on the y-axis and the detector-level jet $p_{\mathrm{T,jet}}^{\mathrm{det}}$ where the p_{T}-smearing and the efficiency was applied on the x-axis. Lower: Background response matrix. Detector-level jets with $p_{\mathrm{T,jet}}^{\mathrm{det}}$ are embedded into the SE and the reconstructed jets are matched to $p_{\mathrm{T,jet}}^{\mathrm{det}}$.

before the embedding. The matching is done by searching the jet which has the largest energy fraction of the original detector-level jet. One example of a background response matrix with $\hat{p}_{\mathrm{T}} = 75 - 100$ GeV/c is shown in the lower plot of figure 8.4. The diagonal is represented again by the black line. A smearing of the detector-level p_{T} to lower and higher values reconstructed with the anti-k_{T} in the event is observed.

The difference of the reconstructed and embedded jet p_{T} is described by δp_{T} as given in equation 8.2. It describes the fluctuation in the background energy density.

$$\delta p_{\mathrm{T}} = p_{\mathrm{T,jet}}^{\mathrm{reco}} - p_{\mathrm{T}}^{\mathrm{embed}} \tag{8.2}$$

The probability distribution of δp_{T}, corresponding to the response matrix shown in the lower plot of figure 8.4, is depicted in figure 8.5. Again the PYTHIA jets which are generated with the phase space interval $\hat{p}_{\mathrm{T}} = 75 - 100$ GeV/c are used as an example. The distribution is basically centered around zero. It is not fully symmetric as an increase is observed at $\delta p_{\mathrm{T}} > 0$ GeV/c in comparison to a Gaussian fit. This was already observed in section 5.1 where a single 10 GeV/c track was embedded into the SE. In addition, some entries are visible at $\delta p_{\mathrm{T}} < -30$ GeV/c. These are the same entries as observed in the background response matrix where only a small fraction of the embedded jet was reconstructed. This could be prevented by requiring that the fraction of the embedded jet energy in the matched jet should be at least 25%. Other thresholds are possible too.

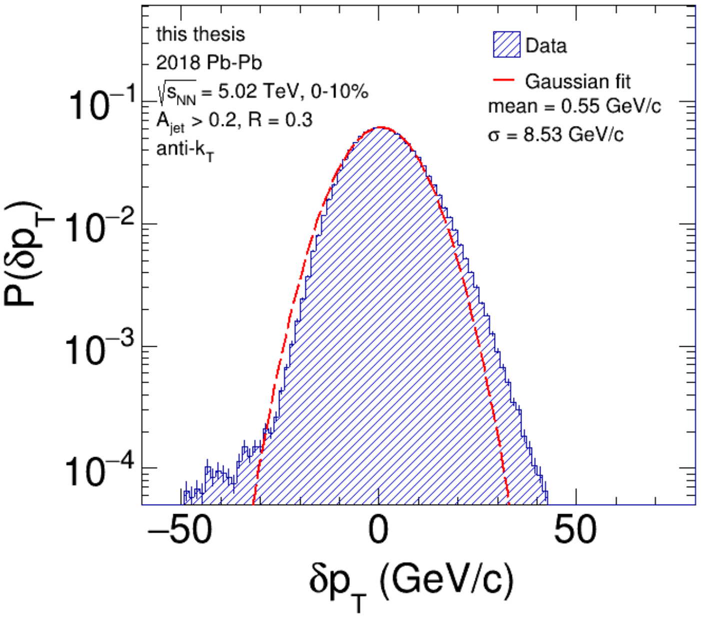

Figure 8.5.: Probability distribution of δp_{T} where reconstructed PYTHIA detector-level jets, obtained from particle-level jets generated with $\hat{p}_{\mathrm{T}} = 75$ - 100 GeV/c, are embedded into the SE. The matching to the reconstructed jets is done with the largest energy fraction.

For the unfolding the combination of the two response matrices described above is used. For the estimation of this full response matrix detector-level jets are embedded into the SE and matched with the PYTHIA particle-level jets. Again the jets which share the largest fraction of energy are matched as it is done for the background response matrix. There are different other approaches how the matching could be done. For example the jets which have the greatest agreement in the number of PYTHIA tracks could be matched. Another approach is the matching of jets by their areas. However it is possible that a jet has a large area and is still a low p_{T} jet because it contains mainly low p_{T} background particles.

The calculation of the response matrix is done for each $\hat{p}_{\mathrm{T}}$ bin separately. After the scaling with the cross-sections the matrices are added to obtain the full response matrix. The final response matrix is shown in figure 8.6 with the particle-level jet p_{T} on the y-axis and the embedded detector-level jet into the SE $p_{\mathrm{T,jet}}^{\mathrm{det,reco}}$ on the x-axis. The matrix is normalized to one within each y-bin. Therefore, each particle-level jet p_{T} appears with the same probability. The effect of the efficiency is clearly visible as lots of particle-level jets end up at lower measured $p_{\mathrm{T,jet}}^{\mathrm{det,reco}}$.

This response matrix is used in the next section where the unfolding procedure is described.

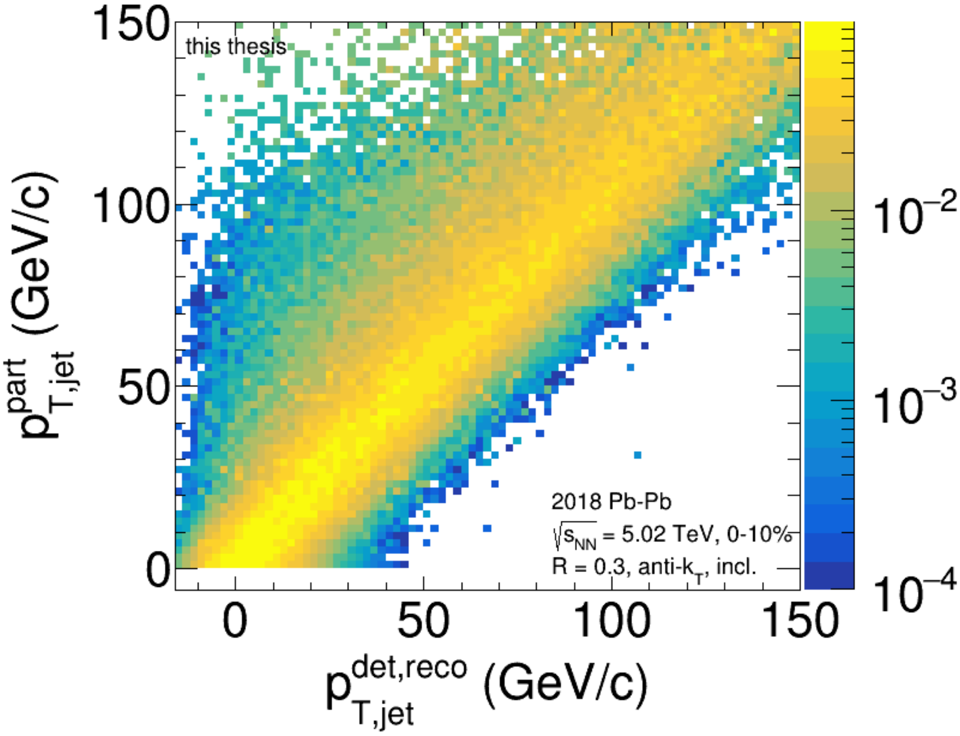

Figure 8.6.: Full response matrix for inclusive jets reconstructed with the anti-k_{T} algorithm with $R = 0.3$. Particle-level jets on the y-axis and embedded detector-level jets in SE on the x-axis. The matching is done for jets which share the largest energy fraction.

8.4. Unfolding

The unfolding of the raw correlated jet distribution is done in order to obtain the true jet distribution. In the previous sections the calculation of the response matrix was described which is a necessary input for the unfolding. As shown in equation 8.1 the true and measured jet distributions are connected by the response matrix. If the detector and background response is known the true distribution can be calculated from the observed distribution by the inversion of equation 8.1. However, it is not straightforward to solve this problem as the matrix does not need to be invertible.

There is no guarantee that the mapping of the measured signal to the true distribution is bijective and a unique solution can be found. Small variations in terms of statistical fluctuations in the measured signal can lead to completely different resulting true distributions [88]. In addition by refolding the obtained true distribution it is possible that the result is not the same as the original measured signal. One may have to accept a loss of information. This depends on the precision up to which the response matrix is known and the available statistics. To take care of this, additional constraints are necessary which can bias the results. In regularized unfolding methods an additional smoothness constrain is applied to suppress large fluctuations [88].

One regularized unfolding method is the Bayesian unfolding. It is based on Bayes' Theorem [89] as given in equation 8.3. In this approach different independent causes C_i $(C_1, C_2, ..., C_{\mathrm{n_C}})$, which correspond to the true events, can lead to an effect E, the measured signal. The probability that an effect E was produced due to cause C_i is given by $P(C_\mathrm{i}|E)$. It is the product of the probability of a cause $P(C_\mathrm{i})$ and the probability that this cause lead to the effect E $P(E|C_\mathrm{i})$. The product is normalized by the sum of all probabilities of the causes C_l times their probabilities to produce the effect.

$$P(C_\mathrm{i}|E) = \frac{P(E|C_\mathrm{i})P(C_\mathrm{i})}{\sum_{l=1}^{n_\mathrm{C}} P(E|C_\mathrm{l})P(C_\mathrm{l})} \tag{8.3}$$

In this approach an additional assumptions of the true probabilities of the causes $P(C_\mathrm{i})$ are necessary. This input is called a prior function and is an additional choice which can be made. By measuring $n(E)$ events with effects E one can calculate the assigned number of events with cause C_i which lead to the measured number of effects by using equation 8.4. In this equation ϵ_i is the efficiency of measuring an effect which is caused by cause C_i. For an efficiency of zero no events are observed from the cause because the experiment is not sensitive to them.

$$n(C_\mathrm{i}) = \frac{1}{\epsilon_\mathrm{i}} \sum_{j=1}^{n_\mathrm{E}} n(E_\mathrm{j})P(C_\mathrm{i}|E_\mathrm{j}) \tag{8.4}$$

From this the total number of true events N_true can be calculated as the sum of all $n(C_\mathrm{i})$ and thus the probabilities $P(C_\mathrm{i}) = n(C_\mathrm{i})/N_\mathrm{true}$ of the causes which can be used as new prior function. In order to obtain the final unfolded distribution this procedure is repeated several times in order to update the initially guessed probability. A limited number of iterations ensures regularization.

An other approach of regularized unfolding is the Singular Value Decomposition

(SVD) as described in [90].

The unfolding of the correlated jet distribution is done with the ROOT unfolding framework RooUnfold [91]. The package provides several unfolding methods as the Bayesian or SVD unfolding. The Bayesian unfolding method is used in the following. The regularization parameter is set to three or four. In addition the prior function is varied. As described in section 8.1 the PYTHIA particle-level jet distributions are used in order to obtain the response matrix. The response matrix shown in figure 8.6 is normalized such that all particle-level jet p_{T} have the same probability. This corresponds to a flat prior function.

In addition, a Levy function, as already used in section 6.1, is introduced as a prior function which modifies the probability of the particle-level jets. The function is given in equation 6.1 and different distributions are shown in figure 8.7. The two parameters $B = 10$ and $m_0 = 0.3$ are fixed. The other parameters T and n are varied between 2 and 2.9 in steps of 0.1 (T) and 5 to 9.5 in steps of 0.5 (n). An additional shift of the mean value is applied between 5 and 9.5 GeV/c in steps of 0.5 GeV/c. In total 1000 different combinations of parameters for the prior function are used for the unfolding and in addition the regularization parameter is set to three and four which results in 2000 different setups. It is possible to submit the calculation to the batch farm, in order to perform an efficient calculation of the corrected jet distributions for the 2000 different parameter setups. The calculations are split into 100 jobs which can be submitted. This allows a large number of systematic variations of the parameters within a short time.

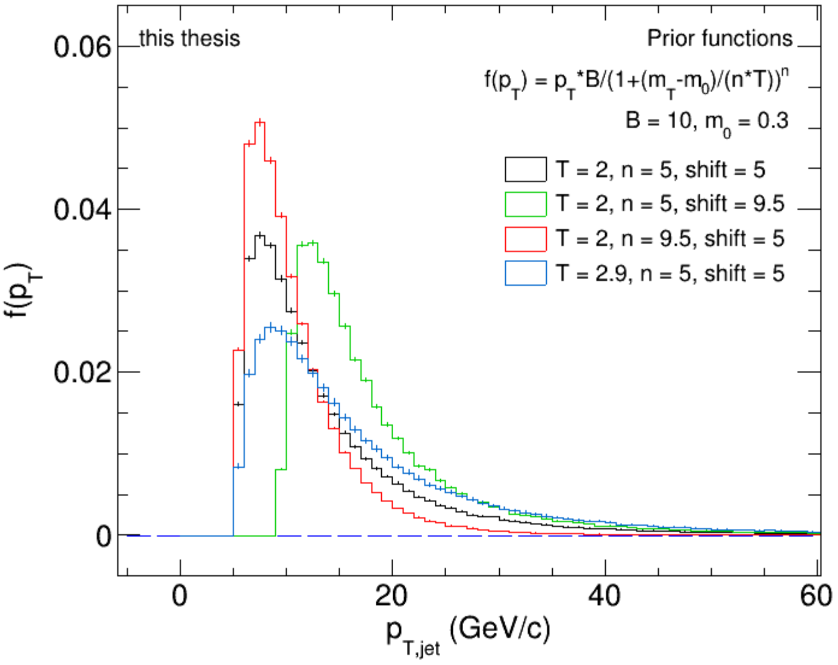

Figure 8.7.: Example of four different prior functions used for the unfolding.

In figure 8.7 four examples of the prior function are shown. For the black and green distribution it is $T = 2$ and $n = 5$ and a shift of 5 GeV/c (black) and 9.5 GeV/c was applied. For the red distribution the same parameter $T = 2$ and a shift of

5 GeV/c was used, as for the black distribution, but the parameter n was increased to $n = 9.5$. For larger n the function drops faster at higher p_{T}. In comparison to that the slope of the distribution can be varied by using different values for T. The distribution gets broader if T is increased as observed for the blue distribution in figure 8.7.

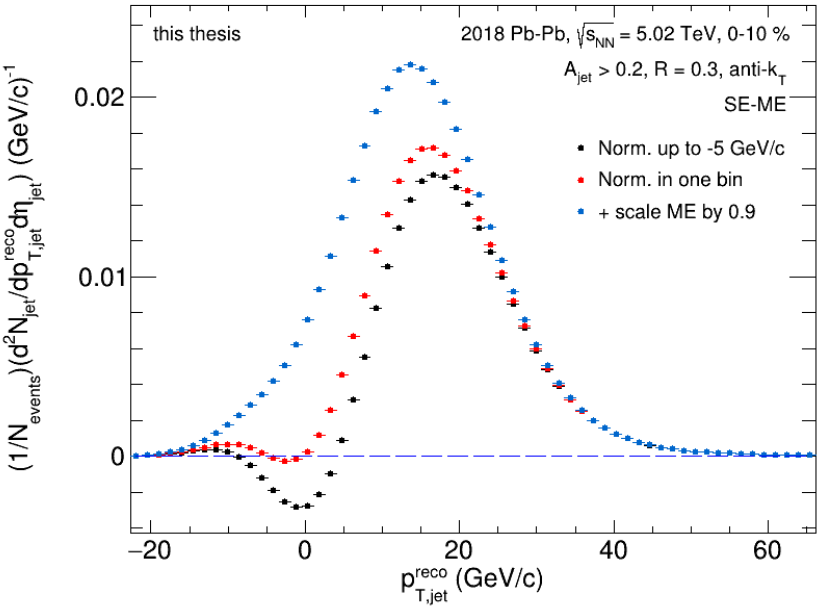

Figure 8.8.: Raw correlated quasi-inclusive jet distribution with a 4 GeV/c leading track cut. The black distribution is the same as shown in figure 7.4, where the ME was normalized to the SE up −5 GeV/c. For the red distribution a normalization within only one bin (bin with −5 GeV/c) was used. The same normalization was applied for the blue distribution and in addition the ME was scaled down by a factor 0.9.

The unfolding is done for the raw correlated quasi-inclusive jet distribution with a 4 GeV/c bias as shown in figure 7.4. Because a small difference between the SE and ME jet distribution around 0 GeV/c was observed the correlated jet distribution is negative in this $p^{\mathrm{reco}}_{\mathrm{T,jet}}$ region. The reason for this is the narrower ME distribution.

In section 6.2 the normalization of the ME to the SE was described and a range up to −5 GeV/c was found to result in the best description of the SE by the ME at $p^{\mathrm{reco}}_{\mathrm{T,jet}} < 0$ GeV/c. A flat SE/ME ratio was required at $p^{\mathrm{reco}}_{\mathrm{T,jet}} < 0$ GeV/c because the SE consists mainly of uncorrelated background in this region. However negative $p^{\mathrm{reco}}_{\mathrm{T,jet}}$ values are possible due to background fluctuations. True jets with very small energies of only a few GeV/c, might be at large negative $p^{\mathrm{reco}}_{\mathrm{T,jet}}$ due to large background fluctuations. In this sense a normalization of the ME to the SE only at the lowest $p^{\mathrm{reco}}_{\mathrm{T,jet}}$ values at the left side is possible, where one can assume that correlations in the SE are negligible. Because this is not practicable due to the low statistics at the left side of the jet distributions another normalization is applied.

Before the ME is subtracted from the SE it is normalized only within one bin around −5 GeV/c to the SE distribution. Thus the resulting difference SE-ME is zero within this bin. After that the ME is scaled down until a smooth transition to the peak is obtained. The bin which is used for the normalization is an arbitrary selection and other bins where the statistics is not too low at $p_{\mathrm{T,jet}}^{\mathrm{reco}} < 0$ GeV/c are also possible. With this normalization negative entries in the SE-ME distributions are avoided. Further studies will be carried out with a simulation, in order to study the behavior of the ME and the region where only uncorrelated background is expected.

The correlated jet distributions with the 4 GeV/c leading track cut with the different normalization of the ME to the SE, as described above are shown in figure 8.8. The normalization is done before the ME is subtracted from the SE. For the black distribution the ME was normalized to the SE distribution up to -5 GeV/c as it was done in previous sections. For the calculation of the red distribution only one bin, which contains -5 GeV/c was used for the normalization. The same bin and an additional scaling factor of 0.9 was used for the ME shown in blue, before it was subtracted from the SE distribution.

In particular a smooth distribution which can be used for the unfolding is obtained by using this different normalization. The resulting raw correlated jet distribution with the new normalization as described above is shown in black in figure 8.9. In addition, the corrected, unfolded jet distribution (red) is depicted. The corrected jet distributions are folded back to the measured signal with the response matrix in order to get a comparison to the original measured signal. These distributions (refolded) are depicted in blue.

The χ^2 is calculated between the measured signal and the refolded distributions. Only 20% of the results with the smallest χ^2 values are shown in the figure. This corresponds to 400 different unfolded and refolded distributions. The ranges between these distributions are depicted by the red (unfolded) and blue (refolded) shaded regions. The result with the smallest χ^2 is obtained with the Levy function as a prior with $T = 2$, $n = 9.5$ and a shift of 8.5 GeV/c. The regularization parameter was set to three. On the x-axis the jet $p_{\mathrm{T,jet}}$ is shown which corresponds to the reconstructed jet $p_{\mathrm{T,jet}}^{\mathrm{reco}}$ in the case of the measured and refolded signal and the true $p_{\mathrm{T,jet}}$ in the case of the unfolded distribution.

A reasonable result for the corrected jet distribution is obtained. The unfolded jet distribution starts just above the bias of 4 GeV/c, which was applied in the jet reconstruction. Due to this applied bias, values below 4 GeV/c in the true distribution are not possible. The bias was not used as an input for the unfolding and is a result from the procedure. The maximum of the distribution is reached at 12 GeV/c. The systematic uncertainty can be estimated from the range of the different unfolded results. In addition, a reasonable agreement between the measured data and the refolded distributions is obtained which confirms the obtained unfolded jet distribution. Some deviations between the data and the refolded distribution are visible between -10 and -20 GeV/c. It is possible that some information get lost in the refolding procedure because of the few bins in the unfolded distribution at the left side tail. A smaller binning could be used to further improve the refolded distribution.

For further studies several adjustments of the parameters for the unfolding can be done. Different prior functions can be used as well as additional regularization parameters and unfolding methods. The whole chain to perform the unfolding is set up, just some more variations are necessary which are beyond the scope of this thesis. In addition the PYTHIA particle-level distribution folded with the response matrix can be used for a comparison to the real data in order to verify the unfolding procedure.

According to figure 15 in [45], the jet reconstruction efficiency has to be applied to the unfolded jet distribution, as an additional small correction. It can be easily obtained by calculating the number of particle-level jets without a matching detector-level jet. The detector-level jet might be lost mainly due to the tracking efficiency.

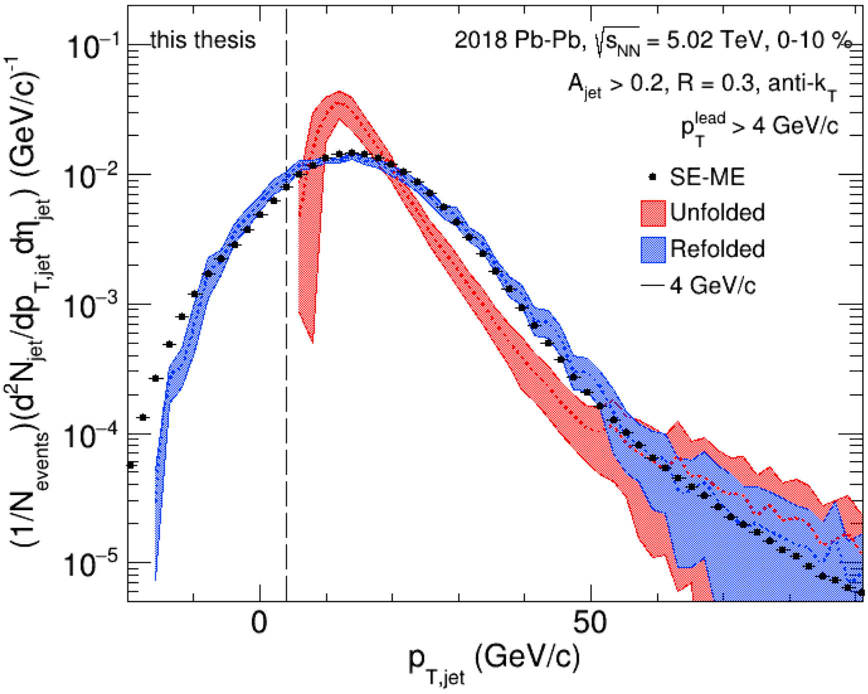

Figure 8.9.: Correlated jet distribution SE-ME with a 4 GeV/c leading track cut before (black) and after (red) the correction by unfolding is applied. The corrected distribution is refolded (blue) in order to verify the unfolding procedure. The $p_{\mathrm{T,jet}}$ on the x-axis corresponds to $p_{\mathrm{T,jet}}^{\mathrm{reco}}$ for the measured and refolded distribution and the true $p_{\mathrm{T,jet}}$ in the case of the unfolded distribution. For the unfolded and refolded distributions the best 20% of the results with the smallest χ^2 are shown. The Levy function was used as a prior, details are described in the text.

8.5. Systematic uncertainties

In the next step the statistic and especially the systematic uncertainties have to be determined. Because this is out of the scope of this thesis, only a brief description of the next steps follows in this section. In section 6 lots of variations of the ME were done which can be used for the estimation of the systematic uncertainties.

For the high momentum splitting in the ME, as introduced in section 6.1, only small differences between the different thresholds for the splitting were observed. In section 6.2 different normalization regions are used. Uncertainties of about 15% are expected from figure 6.5. An additional systematic uncertainty arises due to the definition of the reconstruction of the event-to-event background energy density. In section 6.3.1 different numbers of jets are removed for the calculation of the SE and ME ρ, which had a relatively large impact on the resulting correlated jet distributions. In addition variations of the area cut should be performed, to study its impact on the reconstructed jet population. As shown in figure 6.6, lots of jets are discarded by the used area cut. Additional systematic uncertainties can be estimated for the dependence of the ME on the used categorization into event-plane, multiplicity and z-vertex bins, as presented in section 6.4.

The determination of the tracking efficiency is a necessary next step. The efficiency as well as other instrumental effects, generate an additional systematic uncertainty. By comparing the δp_{T} distributions shown in figure 5.3 and 8.5, where one 10 GeV/c track and PYTHIA generated jets are embedded, one could estimate the systematic uncertainty of δp_{T}.

As already observed in [45], a large component of the systematic uncertainty arises due to the unfolding procedure. The variation of the setup used for the unfolding, as presented in section 8.4, can be used for the estimation of this systematic uncertainty.

In addition variations of the track selection cuts are performed in section 4.2. In order to obtain a systematic uncertainty the different sets of cuts have to be used for the jet reconstruction. So far only the hybrid tracks are used. Variations of these cuts on the tracks can be easily performed before the jet reconstruction is done, as described in section 4.2. For example variations of the DCA cut might lead to a different behavior of the pileup events as described in section 4.3.

9. Summary and Outlook

A novel approach for the estimation of the uncorrelated background in heavy-ion jet measurements at LHC energies was presented in this thesis. Mixed events were introduced as a possible solution to perform jet measurements down to very low p_{T}, where a large population of uncorrelated background jets disturbs the measurement. The mixed events were used successfully for the first time in a semi-inclusive h-jet measurement at STAR [45]. In this thesis they are used for a charged jet measurement at ALICE for the first time. The most central events (0-10%) of the 2018 Pb+Pb data set measured with ALICE at $\sqrt{s_{\mathrm{NN}}} = 5.02$ TeV are analysed. Different track cuts were studied and finally the hybrid tracks with some additional basic quality cuts on the tracks were used. The anti-k_{T} algorithm provided by the FastJet package [44] is used for the jet reconstruction with a default radius of $R = 0.3$. The k_{T} algorithm with $R_{\mathrm{bckg}} = 0.3$ was used for the background estimation, which is described by the event-to-event background energy density ρ.

The procedure to obtain a reasonable description of the uncorrelated background in jet measurements was described. Only one track of each real event is used for the creation of a ME. This ensures the destruction of all jet like correlations and by applying the same jet reconstruction only uncorrelated background jets are found. This ME jet distribution is normalized to the SE distribution within an interval at negative $p_{\mathrm{T,jet}}^{\mathrm{reco}}$ where mainly uncorrelated background jets are expected.

Different aspects in the mixing procedure had to be considered to obtain a good description of the uncorrelated background by the ME. The multiplicities of the ME are sampled from real data, thus the same distribution is obtained. In addition all acceptance effects that are present in the real events are reproduced by the ME.

The event categorization is introduced which guarantees that only events which have similar event plane angles, z-vertex positions and multiplicities are used for the mixing. This categorization results in a very good description of the uncorrelated background in the same events. The ME jet population is studied in dependence of the event plane, the multiplicity and z-vertex. As expected, the uncorrelated background, which consists mainly of particles from the bulk, depends strongly on the event plane. In addition a high momentum splitting for the particles in the ME was introduced to ensure no high p_{T} objects from real jets are within the ME. It turned out that event-by-event p_{T} fluctuations are also important for the production of the ME. They have to be considered by mixing only events with similar $p_{\mathrm{T}}^{\mathrm{sum}}$ values of all tracks. Otherwise only ME with some mean $p_{\mathrm{T}}^{\mathrm{sum}}$ values were created. The additional binning was only used for a subset of the data and should be extended to the whole data set in the future. The remaining difference in the SE and ME ρ distributions could be accounted for by an additional ρ shift of 1 GeV/c.

With the mixed events a reasonable description of the uncorrelated background in the inclusive jet distribution is obtained which enables inclusive jet measurements down to very low p_{T} for the first time at LHC energies. Cuts on the reconstructed jet p_{T} are no longer necessary. However, some small deviations between the SE and ME jet distributions are still observed which should be further investigated. By a broadening of the ME jet distribution by 3% a perfect description of the SE jet distribution is obtained. A general dependence of the ME on correlations was observed. By including correlations the ME was always broadened. Further studies of the ME in dependence of the $p_{\mathrm{T}}^{\mathrm{sum}}$ or the flow could be carried out to possibly further broaden the ME distribution.

Similar results were obtained for the h-jet distribution where different trigger p_{T} intervals where used. For a trigger p_{T} between 3 and 5 GeV/c a jet distribution closer to the ME distribution is obtained as less real jets are reconstructed as expected. More jets are reconstructed if a larger trigger p_{T} is selected between 20 and 100 GeV/c where the overall energy of the selected process is higher.

In addition, the quasi-inclusive jet distributions with different biases were studied. A leading track cut of $p_{\mathrm{T}}^{\mathrm{lead}} > 2, 3, 4$ and 5 GeV/c was applied. While the results for the 2 and 3 GeV/c bias are similar to the inclusive distributions, an almost perfect description of the SE by the ME at $p_{\mathrm{T,jet}}^{\mathrm{reco}} < 0$ GeV/c was obtained with the 4 and 5 GeV/c leading track cuts. Different jet radii of $R = 0.2, 0.3$ and 0.4 were compared for the quasi-inclusive distribution with $p_{\mathrm{T}}^{\mathrm{lead}} > 4$ GeV/c. As expected, the overall jet yield gets larger if a smaller jet radius and thus a smaller jet area was used in the jet reconstruction. This results in a narrower distribution. The description of the uncorrelated background by the ME gets better if a smaller jet radius was used.

The raw correlated jet distribution is obtained by subtracting the uncorrelated background, the ME jet population, from the SE jet distribution. In the last section the unfolding procedure was described which is applied to correct the raw correlated jet distributions for background and detector effects. The response matrix was obtained by using PYTHIA generated p+p particle-level jets. The p_{T} resolution and the efficiency was used to get the detector-level jets which were embedded into the SE in order to obtain the response matrix. For the unfolding the ROOT unfolding framework RooUnfold with the Bayesian unfolding method is used. A reasonable result was obtained for the quasi-inclusive jet distribution with a 4 GeV/c leading track cut. As expected, the distribution starts just above 4 GeV/c and no entries are observed at smaller $p_{\mathrm{T,jet}}$.

However, further studies are necessary as the remaining difference between the SE and ME at low $p_{\mathrm{T,jet}}^{\mathrm{reco}}$ had to be compensated by the normalization in order to get a smooth distribution for the unfolding procedure. As a next step a fast simulation of the ME jet distribution is carried out in order to simulate the description of the uncorrelated background. In addition, the real tracking efficiency has to be calculated. With the variations of the parameters for the ME, presented in this thesis, the systematic uncertainties can be estimated in the next step.

The presented mixed-event technique provides an unique and universal tool to perform inclusive jet measurements down to very low p_{T}, where the jets are expected to lose most of their energy within the QGP. Due to the limiting background in heavy-ion collisions a huge amount of jets were ignored in previous jet measurements. This limiting factor of the uncorrelated background in heavy-ion jet measurements is removed by the purely statistical approach of the mixed events. Therefore, this method represents an essential part in the jet reconstruction in heavy-ion collisions. Once the procedure presented in this thesis is finalized it offers a full new regime of possible jet measurements. Measurements of heavy-flavor jets or γ-jet correlations, which could be performed by including the information from the EMCal, are possible down to low p_{T}. In addition it is possible to search for large-angle Molière scattering, which can be used to probe the quasi-particle nature of the QGP, since a sensitivity only for low p_{T} jets is expected.

A. Appendix

A.1. Event plane

Event plane correction with recentering

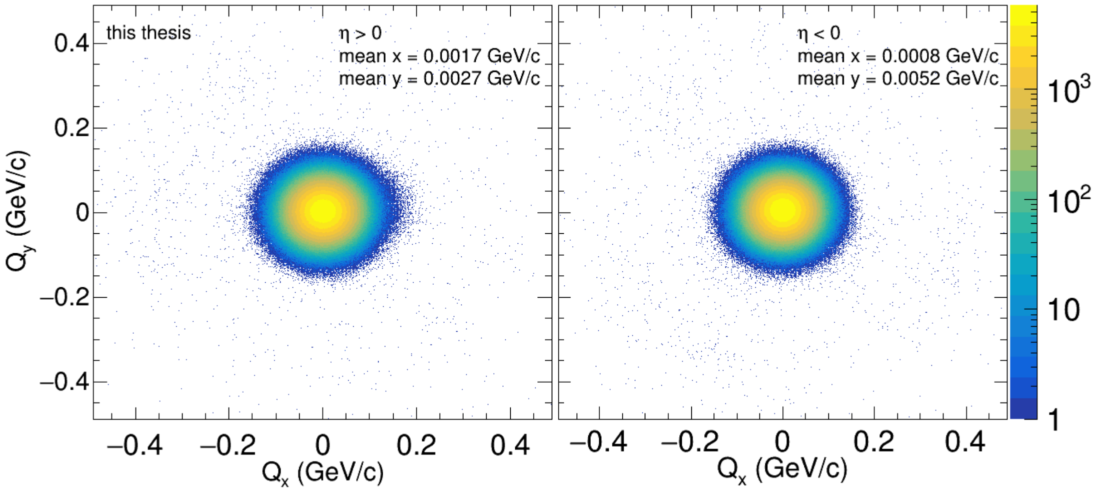

Figure A.1.: Q_x and Q_y for positive (left) and negative (right) η. The offset from zero of the mean values are subtracted in order to correct the event plane as described in section 5.2.

Event plane correction with inverse ϕ weight

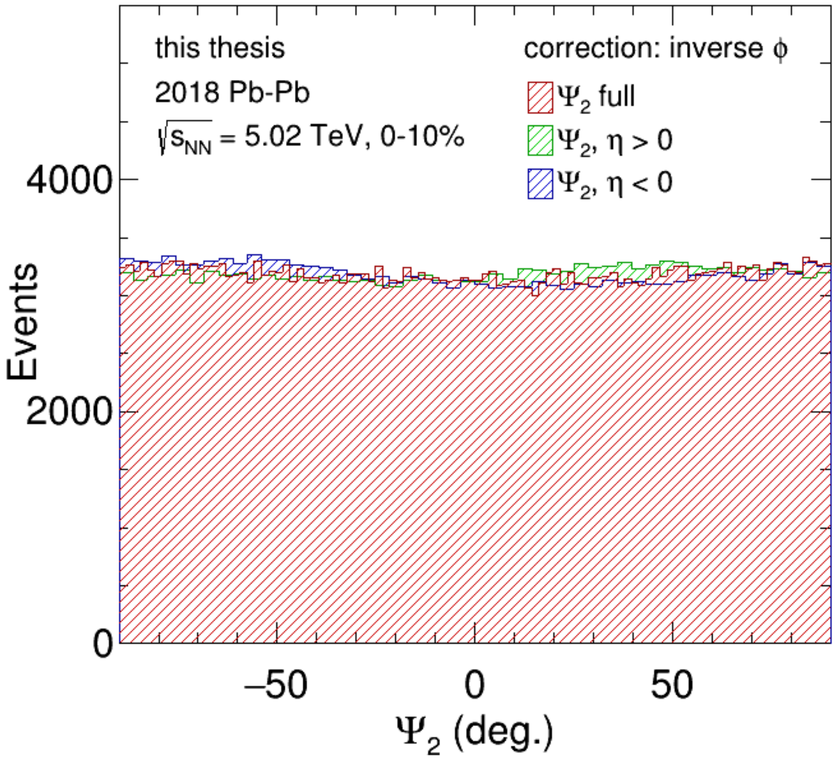

Figure A.2.: Event plane angle Ψ_2 over the full acceptance (red) and for positive (green) and negative (blue) η after the correction with inverse ϕ was applied. Only a subset of the data was used.

A.2. Mixed event studies

Event plane dependence of ME

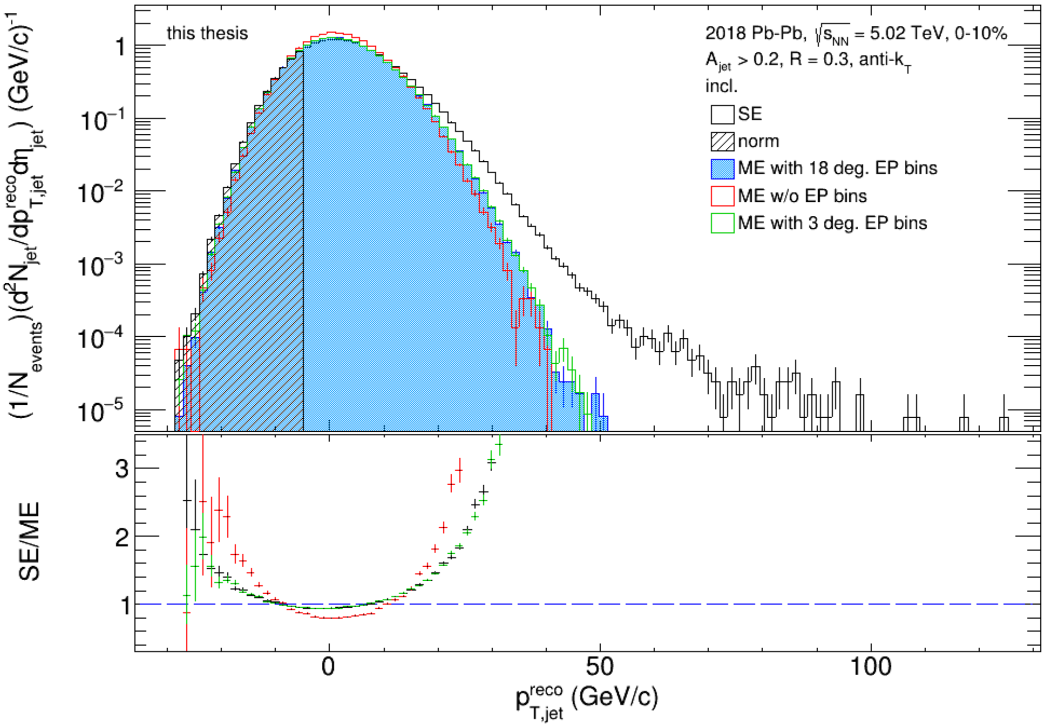

Figure A.3.: Raw inclusive jet distribution of all reconstructed jets with R = 0.3 of the SE (black) and ME with 18° event plane bins (blue), ME with 3° event plane bins (green) and ME without event plane bins (red). Lower panel: Ratios SE/ME with 18° bins (black), 3° bins (green) and without event plane bins (red). A subset of the data with one multiplicity and z-vertex bin was used.

Dependence of the ME on the z-vertex

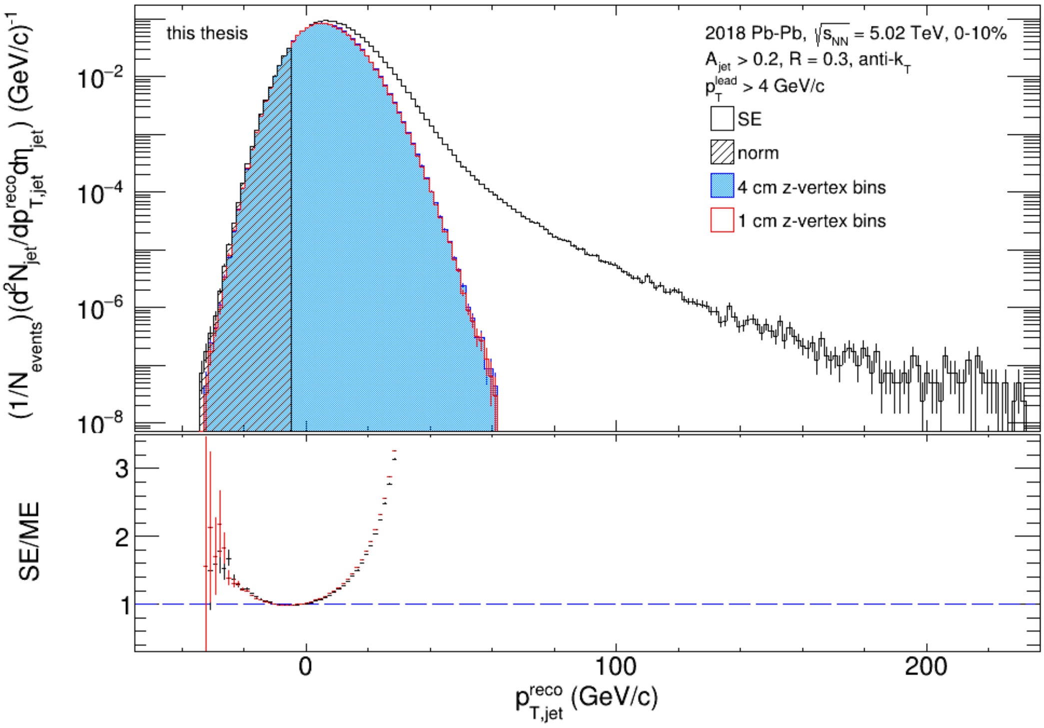

Figure A.4.: Raw quasi-inclusive jet distribution of all reconstructed jets with a leading track of 4 GeV/c with R = 0.3 of the SE (black) and ME with 4 cm z-vertex bins bins (blue) and ME with 1 cm z-vertex bins (red). Lower panel: Ratios SE/ME with 4 cm z-vertex bins bins (black) and with 1 cm z-vertex bins (red). The full data set was used.

Run dependent observation

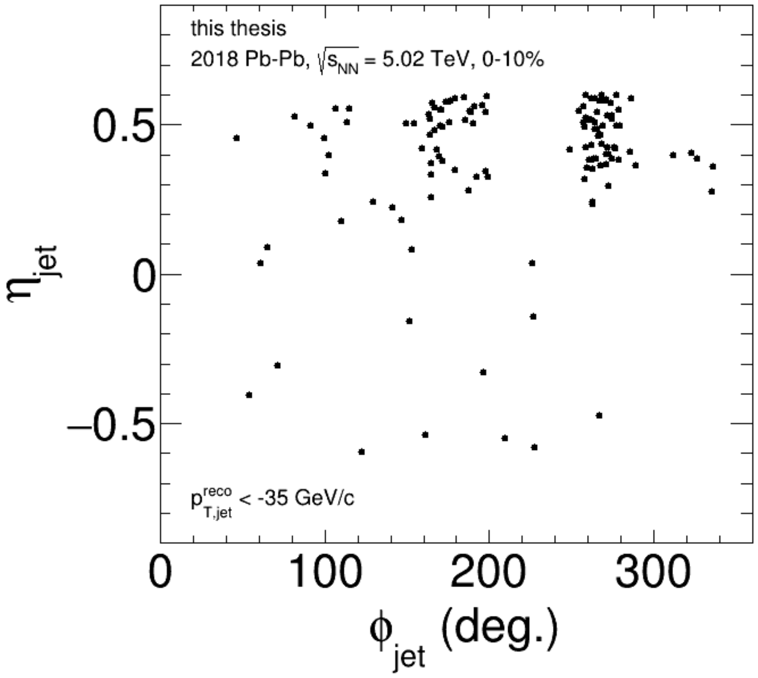

Figure A.5.: $\eta - \phi$ distribution of inclusive jets for the SE with $p_{\mathrm{T,jet}}^{\mathrm{reco}} < -35$ GeV/c.

A.3. Raw jet distributions

Quasi-inclusive jet distribution

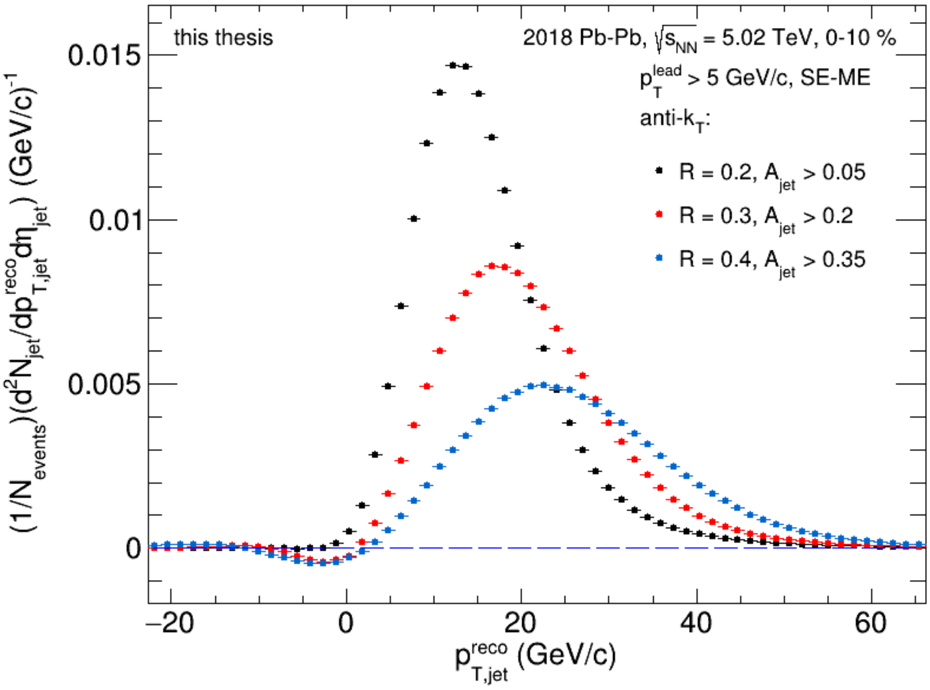

Figure A.6.: Raw correlated quasi-inclusive jet distribution with a bias of $p_T^{lead} >$ 5 GeV/c as function of $p_{T,jet}^{reco}$. For the jet reconstruction the anti-k_T algorithm was used with a jet radius of $R = 0.2$ (black), $R = 0.3$ (red) and $R = 0.4$ (blue).

Bibliography

[1] M. Thomson, *Modern Particle Physics*. Cambridge: Cambridge University Press, 2013, ISBN: 978-1-107-03426-6.

[2] H. Satz, *Extreme States of Matter in Strong Interaction Physics: An Introduction*. Cham: Springer, 2018, vol. 945, ISBN: 978-3-319-71893-4, 978-3-319-71894-1.

[3] *The Higgs boson*, `https://home.cern/science/physics/higgs-boson`. (visited on 05/16/2022).

[4] *Quantum Chromodynamics*, `https://pdg.lbl.gov/2021/reviews/rpp2021-rev-qcd.pdf`. (visited on 05/16/2022).

[5] S. Sarkar, H. Satz, and B. Sinha, Eds., *The physics of the quark-gluon plasma*. 2010, vol. 785.

[6] P. W. Anderson, "More Is Different," *Science*, vol. 177, no. 4047, pp. 393–396, 1972.

[7] A. Bzdak, S. Esumi, V. Koch, J. Liao, M. Stephanov, and N. Xu, "Mapping the Phases of Quantum Chromodynamics with Beam Energy Scan," *Phys. Rept.*, vol. 853, pp. 1–87, 2020. arXiv: `1906.00936 [nucl-th]`.

[8] H.-T. Ding, F. Karsch, and S. Mukherjee, "Thermodynamics of strong-interaction matter from Lattice QCD," *Int. J. Mod. Phys. E*, vol. 24, no. 10, p. 1 530 007, 2015. arXiv: `1504.05274 [hep-lat]`.

[9] *CERN Webpage, Heavy ions and quark-gluon plasma*, `https://home.cern/science/physics/heavy-ions-and-quark-gluon-plasma`. (visited on 08/31/2022).

[10] P. Braun-Munzinger and A. Schmah, *Quark-Gluon Plasma Lecture, Heidelberg University*, 2021.

[11] S. Borsanyi, G. Endrodi, Z. Fodor, A. Jakovac, S. D. Katz, S. Krieg, C. Ratti, and K. K. Szabo, "The QCD equation of state with dynamical quarks," *JHEP*, vol. 11, p. 077, 2010. arXiv: `1007.2580 [hep-lat]`.

[12] *Cern Webpage, LHC*, `https://home.cern/science/accelerators/large-hadron-collider`, 2022. (visited on 06/21/2022).

[13] *The physics of RHIC*, `https://www.bnl.gov/rhic/physics.php`. (visited on 08/25/2022).

[14] *ALICE at CERN*, `https://home.cern/science/experiments/alice`. (visited on 06/20/2022).

[15] R. Stock, "Relativistic Nucleus-Nucleus Collisions and the QCD Matter Phase Diagram," in *Particle Physics Reference Library: Volume 1: Theory and Experiments*, H. Schopper, Ed. 2020, pp. 311–453.

[16] M. L. Miller, K. Reygers, S. J. Sanders, and P. Steinberg, "Glauber modeling in high energy nuclear collisions," *Ann. Rev. Nucl. Part. Sci.*, vol. 57, pp. 205–243, 2007. arXiv: `nucl-ex/0701025`.

[17] U. Heinz and R. Snellings, "Collective flow and viscosity in relativistic heavy-ion collisions," *Ann. Rev. Nucl. Part. Sci.*, vol. 63, pp. 123–151, 2013. arXiv: `1301.2826 [nucl-th]`.

[18] J. Dunlop, M. Lisa, and P. Sorensen, "Constituent quark scaling violation due to baryon number transport," *Phys. Rev. C*, vol. 84, p. 044 914, 2011. arXiv: `1107.3078 [hep-ph]`.

[19] L. Adamczyk *et al.*, "Elliptic flow of identified hadrons in Au+Au collisions at $\sqrt{s_{NN}}$ = 7.7-62.4 GeV," *Phys. Rev. C*, vol. 88, p. 014 902, 2013. arXiv: `1301.2348 [nucl-ex]`.

[20] A. M. Poskanzer and S. A. Voloshin, "Methods for analyzing anisotropic flow in relativistic nuclear collisions," *Phys. Rev. C*, vol. 58, pp. 1671–1678, 1998. arXiv: `nucl-ex/9805001`.

[21] H. Masui, *Elliptic flow*, `http://rnc.lbl.gov/Poskanzer/BonnerTalk/BonnerTalk.pdf`, 2008. (visited on 07/10/2022).

[22] C. Gale, S. Jeon, and B. Schenke, "Hydrodynamic Modeling of Heavy-Ion Collisions," *Int. J. Mod. Phys.*, vol. A28, p. 1 340 011, 2013. arXiv: `1301.5893 [nucl-th]`.

[23] H. Song, S. A. Bass, U. Heinz, T. Hirano, and C. Shen, "200 A GeV Au+Au collisions serve a nearly perfect quark-gluon liquid," *Phys. Rev. Lett.*, vol. 106, p. 192 301, 2011, [Erratum: Phys.Rev.Lett. 109, 139904 (2012)]. arXiv: `1011.2783 [nucl-th]`.

[24] E. Schnedermann, J. Sollfrank, and U. W. Heinz, "Thermal phenomenology of hadrons from 200-A/GeV S+S collisions," *Phys. Rev.*, vol. C48, pp. 2462–2475, 1993. arXiv: `nucl-th/9307020 [nucl-th]`.

[25] K. Reygers, A. Schmah, A. Berdnikova, and X. Sun, "Blast-wave description of Υ elliptic flow at energies available at the CERN Large Hadron Collider," *Phys. Rev. C*, vol. 101, no. 6, p. 064 905, 2020. arXiv: `1910.14618 [hep-ph]`.

[26] B. B. Abelev *et al.*, "Elliptic flow of identified hadrons in Pb-Pb collisions at $\sqrt{s_{\mathrm{NN}}} = 2.76$ TeV," *JHEP*, vol. 06, p. 190, 2015. arXiv: `1405.4632 [nucl-ex]`.

[27] B. Abelev *et al.*, "D meson elliptic flow in non-central Pb-Pb collisions at $\sqrt{s_{\mathrm{NN}}} = 2.76$ TeV," *Phys. Rev. Lett.*, vol. 111, p. 102 301, 2013. arXiv: `1305.2707 [nucl-ex]`.

[28] E. Abbas *et al.*, "J/ψ Elliptic Flow in Pb-Pb Collisions at $\sqrt{s_{\mathrm{NN}}} = 2.76$ TeV," *Phys. Rev. Lett.*, vol. 111, p. 162 301, 2013. arXiv: `1303.5880 [nucl-ex]`.

[29] S. Acharya *et al.*, “Measurement of deuteron spectra and elliptic flow in Pb–Pb collisions at $\sqrt{s_{\mathrm{NN}}} = 2.76$ TeV at the LHC,” *Eur. Phys. J.*, vol. C77, no. 10, p. 658, 2017. arXiv: `1707.07304 [nucl-ex]`.

[30] N. Grünwald, “Bachelor thesis: Simultaneous blast-wave description of transverse momentum spectra and elliptic flow data at $\sqrt{s_{\mathrm{NN}}} = 7.7$ GeV -5.02 TeV,” 2020.

[31] A. Majumder and M. Van Leeuwen, “The Theory and Phenomenology of Perturbative QCD Based Jet Quenching,” *Prog. Part. Nucl. Phys.*, vol. 66, pp. 41–92, 2011. arXiv: `1002.2206 [hep-ph]`.

[32] E. M. Metodiev, *The Fractal Lives of Jets*, `https://www.ericmetodiev.com/post/jetformation/`, Apr. 2020. (visited on 09/08/2021).

[33] J. C. Collins, D. E. Soper, and G. F. Sterman, “Factorization of Hard Processes in QCD,” *Adv. Ser. Direct. High Energy Phys.*, vol. 5, pp. 1–91, 1989. arXiv: `hep-ph/0409313`.

[34] V. N. Gribov and L. N. Lipatov, “Deep inelastic e p scattering in perturbation theory,” *Sov. J. Nucl. Phys.*, vol. 15, pp. 438–450, 1972.

[35] Y. L. Dokshitzer, “Calculation of the Structure Functions for Deep Inelastic Scattering and e+ e- Annihilation by Perturbation Theory in Quantum Chromodynamics.,” *Sov. Phys. JETP*, vol. 46, pp. 641–653, 1977.

[36] J. D. Bjorken, “Energy Loss of Energetic Partons in Quark - Gluon Plasma: Possible Extinction of High p(t) Jets in Hadron - Hadron Collisions,” Aug. 1982.

[37] L. Cunqueiro and A. M. Sickles, “Studying the QGP with Jets at the LHC and RHIC,” *Prog. Part. Nucl. Phys.*, vol. 124, p. 103 940, 2022. arXiv: `2110.14490 [nucl-ex]`.

[38] D. G. d’Enterria, “Quark-Gluon Matter,” *J. Phys. G*, vol. 34, S53–S82, 2007. arXiv: `nucl-ex/0611012`.

[39] C. Adler *et al.*, “Disappearance of back-to-back high p_T hadron correlations in central Au+Au collisions at $\sqrt{s_{NN}} = 200$ GeV,” *Phys. Rev. Lett.*, vol. 90, p. 082 302, 2003. arXiv: `nucl-ex/0210033`.

[40] A. Adare *et al.*, “Dihadron azimuthal correlations in Au+Au collisions at $\sqrt{s_{NN}} = 200$ GeV,” *Phys. Rev. C*, vol. 78, p. 014 901, 2008. arXiv: `0801.4545 [nucl-ex]`.

[41] J. Adams *et al.*, “Direct observation of dijets in central Au+Au collisions at $\sqrt{s_{\mathrm{NN}}} = 200$ GeV,” *Phys. Rev. Lett.*, vol. 97, p. 162 301, 2006. arXiv: `nucl-ex/0604018`.

[42] J. Adams *et al.*, “Transverse momentum and collision energy dependence of high p_{T} hadron suppression in Au+Au collisions at ultrarelativistic energies,” *Phys. Rev. Lett.*, vol. 91, p. 172 302, 2003. arXiv: `nucl-ex/0305015`.

[43] S. S. Adler *et al.*, “Dense-Medium Modifications to Jet-Induced Hadron Pair Distributions in Au+Au Collisions at $\sqrt{s_{\mathrm{NN}}} = 200$ GeV,” *Phys. Rev. Lett.*, vol. 97, p. 052 301, 2006. arXiv: `nucl-ex/0507004`.

[44] M. Cacciari, G. P. Salam, and G. Soyez, “FastJet User Manual,” *Eur. Phys. J. C*, vol. 72, p. 1896, 2012. arXiv: `1111.6097 [hep-ph]`.

[45] L. Adamczyk *et al.*, “Measurements of jet quenching with semi-inclusive hadron+jet distributions in Au+Au collisions at $\sqrt{s_{NN}} = 200$ GeV,” *Phys. Rev. C*, vol. 96, no. 2, p. 024 905, 2017. arXiv: `1702.01108 [nucl-ex]`.

[46] A. Schöning and S. Westhoff, *Standard Model Lecture, Heidelberg University*, 2021.

[47] J. Adam *et al.*, “Measurement of jet suppression in central Pb-Pb collisions at $\sqrt{s_{\mathrm{NN}}} = 2.76$ TeV,” *Phys. Lett. B*, vol. 746, pp. 1–14, 2015. arXiv: `1502.01689 [nucl-ex]`.

[48] J. Adam *et al.*, “Measurement of jet quenching with semi-inclusive hadron-jet distributions in central Pb-Pb collisions at $\sqrt{s_{\mathrm{NN}}} = 2.76$ TeV,” *JHEP*, vol. 09, p. 170, 2015. arXiv: `1506.03984 [nucl-ex]`.

[49] P. M. Jacobs, *private communication*, September 2022.

[50] P. M. Jacobs and A. Schmah, “Measurements of jet quenching with semi-inclusive charged jet distributions in $Au + Au$ collisions at $\sqrt{s_{NN}}$=200 GeV,” *Nucl. Phys. A*, vol. 956, pp. 641–644, 2016. arXiv: `1512.08784 [nucl-ex]`.

[51] *Cern Webpage, history*, `https://home.cern/about/who-we-are/our-history`, 2022. (visited on 06/21/2022).

[52] *Cern Webpage, Our People*, `https://home.cern/about/who-we-are/our-people`, 2017. (visited on 06/21/2022).

[53] *Cern Webpage, timeline*, `https://timeline.web.cern.ch/timeline-header/89`, 2022. (visited on 06/21/2022).

[54] L. Di Lella and C. Rubbia, “The Discovery of the W and Z Particles,” *Adv. Ser. Direct. High Energy Phys.*, vol. 23, pp. 137–163, 2015.

[55] *Cern Webpage, LHC Facts*, `https://home.cern/resources/brochure/knowledge-sharing/lhc-facts-and-figures`, 2017. (visited on 06/21/2022).

[56] *Cern Webpage, LHCb*, `https://home.cern/science/experiments/lhcb`. (visited on 06/21/2022).

[57] *Cern Webpage*, `https://home.cern/news/news/physics/cern-congratulates-englert-and-higgs-nobel-physics`, 2022. (visited on 09/05/2022).

[58] *Cern ALICE Webpage*, `https://home.cern/science/experiments/alice`, 2008. (visited on 02/28/2022).

[59] B. B. Abelev *et al.*, “Performance of the ALICE Experiment at the CERN LHC,” *Int. J. Mod. Phys. A*, vol. 29, p. 1 430 044, 2014. arXiv: `1402.4476 [nucl-ex]`.

[60] S. Acharya *et al.*, “Real-time data processing in the ALICE High Level Trigger at the LHC,” *Comput. Phys. Commun.*, vol. 242, pp. 25–48, 2019. arXiv: `1812.08036 [physics.ins-det]`.

[61] G. Dellacasa *et al.*, “ALICE technical design report of the inner tracking system (ITS),” Jun. 1999.

[62] E. Botta, "ALICE ITS: Operational Experience, Performance and Lessons Learned," *PoS*, vol. Vertex2019, p. 002, 2020.

[63] C. Lippmann, "Upgrade of the ALICE Time Projection Chamber," Mar. 2014.

[64] G. Dellacasa *et al.*, "ALICE: Technical design report of the time projection chamber," Jan. 2000.

[65] S. Acharya *et al.*, "The ALICE Transition Radiation Detector: construction, operation, and performance," *Nucl. Instrum. Meth. A*, vol. 881, pp. 88–127, 2018. arXiv: `1709.02743 [physics.ins-det]`.

[66] F. Carnesecchi, "Performance of the ALICE Time-Of-Flight detector at the LHC," *JINST*, vol. 14, no. 06, p. C06023, 2019. arXiv: `1806.03825 [physics.ins-det]`.

[67] U. Abeysekara *et al.*, "ALICE EMCal Physics Performance Report," Aug. 2010. arXiv: `1008.0413 [physics.ins-det]`.

[68] P. Cortese *et al.*, "ALICE electromagnetic calorimeter technical design report," Sep. 2008.

[69] E. Abbas *et al.*, "Performance of the ALICE VZERO system," *JINST*, vol. 8, P10016, 2013. arXiv: `1306.3130 [nucl-ex]`.

[70] B. Abelev *et al.*, "Technical Design Report for the Upgrade of the ALICE Inner Tracking System," *J. Phys. G*, vol. 41, p. 087 002, 2014.

[71] *ALICE data flow*, `https://indico.cern.ch/event/666222/contributions/2768780/attachments/1551303/2437229/DPG_AnalysisTutorial_20171102.pdf`. (visited on 08/02/2021).

[72] Y. Belikov, M. Ivanov, K. Safarik, and J. Bracinik, "TPC tracking and particle identification in high density environment," *eConf*, vol. C0303241, TULT011, 2003. arXiv: `physics/0306108`.

[73] Y. Pei, S. Biswas, D. S. Fussell, and K. Pingali, *An elementary introduction to kalman filtering*, 2017. [Online]. Available: `https://arxiv.org/abs/1710.04055`.

[74] *ROOT TTree*, `https://root.cern.ch/root/htmldoc/guides/users-guide/Trees.html`. (visited on 04/21/2021).

[75] *ROOT CERN Webpage, list of data types*, `https://root.cern.ch/root/html522/ListOfTypes.html`, 2008. (visited on 12/09/2021).

[76] *PDG summary tables*, `https://pdg.lbl.gov/2022/tables/contents_tables.html`. (visited on 09/07/2021).

[77] S. Acharya *et al.*, "Centrality and transverse momentum dependence of inclusive J/ψ production at midrapidity in Pb–Pb collisions at $\sqrt{s_{\mathrm{NN}}} = 5.02$ TeV," *Phys. Lett. B*, vol. 805, p. 135 434, 2020. arXiv: `1910.14404 [nucl-ex]`.

[78] S. S. Adler *et al.*, "Measurement of nonrandom event by event fluctuations of average transverse momentum in $\sqrt{s_{\mathrm{NN}}} = 200$ GeV Au+Au and p+p collisions," *Phys. Rev. Lett.*, vol. 93, p. 092 301, 2004. arXiv: `nucl-ex/0310005`.

[79] H. Appelshäuser *et al.*, "Event-by-event fluctuations of average transverse momentum in central Pb + Pb collisions at 158-GeV per nucleon," *Phys. Lett. B*, vol. 459, pp. 679–686, 1999. arXiv: `hep-ex/9904014`.

[80] J. Adams *et al.*, "Identified hadron spectra at large transverse momentum in p+p and d+Au collisions at $\sqrt{s_{\mathrm{NN}}} = 200$ GeV," *Phys. Lett. B*, vol. 637, pp. 161–169, 2006. arXiv: `nucl-ex/0601033`.

[81] S. Acharya *et al.*, "Anisotropic flow of identified particles in Pb-Pb collisions at $\sqrt{s_{\mathrm{NN}}} = 5.02$ TeV," *JHEP*, vol. 09, p. 006, 2018. arXiv: `1805.04390 [nucl-ex]`.

[82] R. J. Barlow, "Practical Statistics for Particle Physics," *CERN Yellow Rep. School Proc.*, vol. 5, M. Mulders and J. Trân Thanh Vân, Eds., pp. 149–197, 2020. arXiv: `1905.12362 [physics.data-an]`.

[83] T. Sjöstrand, S. Ask, J. R. Christiansen, R. Corke, N. Desai, P. Ilten, S. Mrenna, S. Prestel, C. O. Rasmussen, and P. Z. Skands, "An introduction to PYTHIA 8.2," *Comput. Phys. Commun.*, vol. 191, pp. 159–177, 2015. arXiv: `1410.3012 [hep-ph]`.

[84] T. Sjostrand, S. Mrenna, and P. Z. Skands, "PYTHIA 6.4 Physics and Manual," *JHEP*, vol. 05, p. 026, 2006. arXiv: `hep-ph/0603175`.

[85] *PYTHIA webpage, version 8.243*, `https://pythia.org/manuals/pythia8243/Welcome.html`, 2017. (visited on 07/01/2022).

[86] J. Kim, "Jet-hadron correlations to search for Mach cone signals in Pb-Pb collisions with ALICE at the LHC," Ph.D. dissertation, U. Heidelberg (main), 2022.

[87] C. Lippmann, "Performance of the ALICE Time Projection Chamber," *Phys. Procedia*, vol. 37, T. Liu, Ed., pp. 434–441, 2012.

[88] G. Bohm and G. Zech, *Introduction to statistics and data analysis for physicists*. Hamburg: DESY, 2014, ISBN: 978-3-935702-88-1.

[89] G. D'Agostini, "A Multidimensional unfolding method based on Bayes' theorem," *Nucl. Instrum. Meth. A*, vol. 362, pp. 487–498, 1995.

[90] A. Hocker and V. Kartvelishvili, "SVD approach to data unfolding," *Nucl. Instrum. Meth. A*, vol. 372, pp. 469–481, 1996. arXiv: `hep-ph/9509307`.

[91] *GitLab RooUnfold*, `https://gitlab.cern.ch/RooUnfold/RooUnfold`. (visited on 07/24/2021).

Acknowledgement

First I wish to express my gratitude to Prof. Dr. Johanna Stachel for giving me the opportunity of writing my thesis within her group in this interesting field of research.

Thank you to Prof. Dr. Norbert Herrmann for being the second referee for my thesis.

I would like to thank especially Dr. Peter Jacobs and Dr. Alexander Schmah for providing the topic of my thesis. Thanks a lot for the weekly discussions, inspirations and the motivation you have given me during the past year. Thank you for answering all my physics questions and helping me with technical issues.

In addition many thanks to Prof. Dr. Johanna Stachel, Dr. Alice Ohlson, Dr. Jiyoung Kim and M.Sc. Luisa Bergmann for discussions and suggestions within our regular meetings.

Thanks to Dr. Alexander Schmah and B.Sc. Sven Hoppner for supporting me in the data production.

At least I would like to thank my family and friends for their support and patience during the last years of my studies.

Erklärung:

Ich versichere, dass ich diese Arbeit selbstständig verfasst habe und keine anderen als die angegebenen Quellen und Hilfsmittel benutzt habe.

Heidelberg, den 04.10.2022

Nadine Grünwald